Fast Hydro Simulation for the Intracluster Medium Physics and Cosmology with the Sunyaev-Zel'dovich Effect

by

Yizhou He

Submitted in partial fulfillment of the
requirements for the degree of
Doctor of Philosophy
at
Carnegie Mellon University
Department of Physics
Pittsburgh, Pennsylvania

Advised by Professor Hy Trac

August 13, 2021

Abstract

My thesis focuses on developing a cosmological code based on an innovative hydro-particle-mesh (HPM) algorithm for Efficient and Rapid (HYPER) simulations of gas and dark matter (He et al., 2021b). HYPER can produce lightcone catalogs of dark matter halos and full-sky tomographic maps of the lensing convergence, Sunyaev-Zel'dovich (SZ) effect, and X-ray emission. These simulation products are useful for testing data analysis pipelines, generating training data for machine learning, understanding selection and systematic effects, and interpreting astrophysical and cosmological constraints. I start my thesis by presenting our study on an analytical model for the average cluster pressure profile, which we use to implement the HYPER simulation. We first come up with a model for estimating hydrostatic bias in the X-ray measurement by fitting a power-law to the relation between the "true" halo mass and X-ray cluster mass in hydrodynamic simulations (IllustrisTNG, BAHAMAS, and MACSIS). We apply this model to the REXCESS X-ray cluster sample and adjust the Universal Pressure Profile (UPP) derived from scaled and stacked pressure profiles (Arnaud et al., 2010) for the hydrostatic mass bias. Our work eventually leads to an updated model, Debiased Pressure Profile (DPP), for the gas pressure profile of galaxy clusters (He et al., 2021a). The second part of this thesis introduces HYPER code in detail, which updates the HPM approach of (Gnedin & Hui, 1998) to expand the scope of its application from the lower-density intergalactic medium (IGM) to the higher-density intracluster medium (ICM). In order to achieve high efficiency and high fidelity for the approximate hydrodynamic solver, the pressure term in the gas equations of motion is calculated using robust physical models. In particular, we use the dark matter halo model, ICM pressure profile, and IGM temperature-density relation to model the gas physics in the IGM and ICM regime, all of which can be systematically varied for parameter-space studies. We show that the HYPER simulation results are in good agreement with the halo model expectations. At the end of this part, we also envision the perspective of use cases for HYPER. I discuss the application of HYPER simulation in SZ science in the final part of this dissertation. We present a template for calculating the thermal and kinetic angular power spectra using the outputs of HYPER simulations, which can be applied to the analyses for future SZ surveys. We also show a simplified case in which this template is combined with observation data to constrain cosmological parameters.

Acknowledgments

First of all, I would like to express my gratitude to my advisor Professor Hy Trac for giving me the opportunity to work with him and meet with many other extraordinary scientists in this intriguing research area. He is always generous with giving his time, sharing his ideas, and offering his suggestions in taking my research progress forward and how to be successful in my future career and life. If not with his guidance and support, it is impossible for me to get to this point.

I would like to thank my thesis committee members, Professor Rachel Mandelbaum, Professor Renyue Cen, and Professor Rupert Croft. I greatly appreciate their willingness to spend their valuable time giving feedback and advice, which significantly improved the quality of my research.

I owe gratitude to all of my collaborators Dr. Markus Michael Rau, Professor Nicholas Battaglia, Professor Nickolay Y. Gnedin, Dr. Philip Mansfield. Insightful discussions with these intelligent researchers immensely helped shape the direction of my research.

I would like to thank Dr. Qirong Zhu, Diptajyoti Mukherjee, Matthew Ho, Nianyi Chen. I am grateful that we are together in the group, and thanks for helpful discussions in both group meetings and private talk, which broaden my vision in research and many other aspects of life.

I would like to thank my fellow graduate students and my friends at Carnegie Mellon University. The days we spend together make my life in Pittsburgh so happy and colorful. I appreciate all the supports whenever I need their help.

I am also indebted to Professor Stephen Garoff. He offered me an opportunity to join the summer exchange program at CMU and helped me decide on pursuing my Ph.D. degree here. I also would like to thank Professor Manfred Paulini and Professor Fred Gilman for all the support about the bureaucratic issues at CMU.

In the end, I would like to take this opportunity to thank my family for their constant encouragement and support, especially my parents, who let me know the true meaning of altruistic love.

Contents

List of Tables

List of Figures

Chapter 1

Introduction

The work presented in this thesis is based on one published paper and one submitted manuscript under review. The references are as follows:

1. **Yizhou He**, Philip Mansfield, Markus Michael Rau, Hy Trac, and Nicholas Battaglia. Debiased Galaxy Cluster Pressure Profiles from X-Ray Observations and Simulations. *The Astrophysical Journal*, 908:91, 2021 February 16. (https://doi.org/10.3847/1538-4357/abd0ff)

   This paper is reproduced in Chapter 2.

2. **Yizhou He**, Hy Trac, and Nickolay Y. Gnedin. A Hydro-Particle-Mesh Code for Efficient and Rapid Simulations of the Intracluster Medium. *The Astrophysical Journal* (submitted)

   This paper is reproduced in Chapter 3.

"Two things fill the mind with ever new and increasing wonder and awe, the oftener and the more steadily we reflect on them: the starry heavens above me and the moral law within me." A motto by Immanuel Kant, one of the most influential figures in modern Western philosophy, reveals the eager of exploring the "unknown" of the universe buried deep in human nature. The "light" radiated outwards from stars composing proto-galaxies ionize the neutral hydrogen atoms encountered ends the "Dark Ages" of our universe and open the Epoch of Reionization. The light shed by stars and galaxies from the vault of heaven also evokes the scientific revolution and turns a new page for human civilization. During the Renaissance, Nicolaus Copernicus proposed a heliocentric model of the solar system. His work was defended by Galileo Galilei and expanded upon by Johannes Kepler. Kepler was the first to devise a system that correctly described the details of the motion of the planets around the Sun. In order to explain the motions of the planets, Isaac Newton invents celestial dynamics and his law of gravitation. People then stepped into a period of rising prosperity of science.

With the advanced development of theories for cosmological models and observation techniques, the origin and evolution of our Universe are gradually unveiled by scientists, from the Big Bang to today and into the future. Before delving into the scientific specifics of my research, I would like to briefly look back on the "life" of a photon, as it travels across space and time, from just moments after the big bang to the human observation instruments.

The light's journey begins around 13.8 billion years ago, just seconds and minutes after the big bang and inflation. The Universe was a hot plasma of electrons, protons, and photons in thermal equilibrium. The light repeatedly bounces off electrons. As a result, the mean free path of photons was very short, and light can not travel very far.

As the Universe kept expanding adiabatically, the Universe became cool enough for the electrons and protons to get together to form neutral atoms. This era, referred to as the Epoch of Recombination, occurred about 380,000 years after the big bang at redshift $z \simeq 1100$. During this epoch, electrons no longer interact with the photo, and light is free to travel. The Universe became transparent to photons, which lead to the emission of the cosmic microwave background (CMB) from the "surface of last-scattering". Exquisite measurements of the CMB have been made by the Wilkinson Microwave Anisotropy Probe (WMAP) and Planck satellites and ground-based telescope Atacama Cosmology Telescope (ACT) and South Pole Telescope (SPT). The next-generation observation plan Simons Observatory (SO) is also on the agenda now. The scientific study of CMB revolutionizes our understanding of cosmology. It helps establish a working cosmological model and leads to unprecedented precise determination of many of the cosmological parameters that shape our Universe.

After recombination and decoupling, the Universe became transparent and allow the light to freely pass through the "dark ages" of the Universe before the light-producing structures such as stars and galaxies form. As neutral baryons evolve under the influence of gravitational attraction, initial inhomogeneities in the matter distribution laid down by inflation get amplified, regions with above-average density accrete matter and become denser. These regions eventually collapsed under gravity and ignited nuclear fusion in their cores and leading to the first stars and galaxies emitting radiation as they burn. Their energy heated the surrounding medium, once again ionizing the hydrogen in the Universe. These areas were like tiny bubbles of ionized gas surrounding bright energy sources at first. These bubbles grew and eventually began to overlap, enabling ionizing radiation to travel farther and farther through space. Reionization might have started to happen as early as $z \sim 16$ and the Universe ionized by $z \sim 7 - 9$. During Reionization, the matter had become far more spread out due to the ongoing expansion of the Universe. Despite the neutral hydrogen atoms being reionized, the plasma was much more thin and diffuse, light across most of the electromagnetic spectrum could travel unimpeded through the cosmos, and the Universe remained largely transparent. Reionization gradually ended as the Universe continued to cool and expand.

After experiencing such a long haul introduced above, photons march to their final stretch of the journey from the endpoint of Reionization to the human observation instruments. During this period, photons might traverse the clusters of galaxies and could once again get scattered by electrons in hot gas trapped in galaxy clusters, which we refer to as the Sunyaev-Zel'dovich (SZ) effect. The SZ effect from galaxy clusters provides the most substantial contribution to temperature anisotropies beyond the damping tail of acoustic peaks in CMB power spectrum (Hu & Dodelson, 2002), where lies a wealth of information about the evolution of structure in the Universe and its origin in the early Universe. The SZ effect also offers a unique way to map the large-scale structure of the Universe as traced by massive clusters of galaxies. SZ surveys like Plank, ACT and SPT have found hundreds to thousands of galaxy clusters. Direct measurement of the evolution of the number density of galaxy clusters by these deep, large-scale SZ surveys provides a unique and powerful observational tool for cosmology (e.g. Planck Collaboration et al., 2014a, 2016b). An interesting statistic, the SZ angular power spectrum, is often used to interpret cosmological constraints (e.g. Lueker et al., 2010; Fowler et al., 2010; Dunkley et al., 2011; Planck Collaboration et al., 2016a; Bolliet et al., 2018) because of the strong dependence of its amplitude on σ_8, a cosmological parameter describing the normalization of matter perturbations. The SZ effect has also been combined with other observational diagnostics of galaxy clusters such as X-ray, weak and strong lensing, and optical measurements to determine cosmological parameters. One example is that cluster distances could be determined from the joint analysis of the SZ effect and X-ray data, which enables interesting constraints on the Hubble constant (e.g. Reese et al., 2000; Reese, 2004; Bonamente et al., 2006). SZ and X-ray measurements also allow tight constraints on cluster gas mass fractions which can be used to estimate matter density of the Universe $\Omega_{\rm m}$. The analysis of various combinations of SZ effect, X-ray, and lensing observations enable robust constraints on the desired properties of clusters, which provides critical insights to our understanding of clusters and critical tests of current models for the formation and evolution of galaxy clusters.

As more advanced cosmological observations are being prepared and ready for use, precise modeling of the observed structure is required to study the evolution and history of the large-scale structure in great detail and accurate constraints on the cosmological parameters. In order to model these observed structures realistically, we need to resort to numerical simulations capable of resolving and following correctly the highly non-linear dynamics.

1.1 Physics of the Sunyaev-Zel'dovich effect

The SZ effect is a small spectral distortion of the CMB spectrum caused by the scattering of the CMB photons off the distribution of high energy electrons, was first proposed in 1970 (Sunyaev & Zeldovich, 1970a). The theoretical foundation of the SZ effect was laid in discussions of a more general problem of Comptonization of a

radiation field by passage through ionized gases, where inverse-Compton scattering is an essential ingredient in the discussion. In this section, I briefly introduce the fundamental physics behind the SZ effect and the distortion of the CMB spectrum caused by the hot thermal distribution of electrons provided by the ICM of galaxy clusters and the Doppler effect coming from scattering with electrons having fast peculiar motions. More details are provided in reviews of the SZ effect (e.g. Birkinshaw, 1999; Carlstrom et al., 2002).

To explain the fundamental physics behind the SZ effect, I start with a case of single photon-electron scattering when a low-energy photon is scattered by a high-energy electron ($\epsilon \ll m_{\rm e}c^2$), which is found appropriate for the scatterings that happened in galaxy clusters. The energy and direction of motion of both the photon and the electron are altered, and the scattering preferentially boosts the energy of the photon. This is also the reason for the scattering that causes the SZ effect is usually referred to as inverse-Compton scattering. In this thermal scattering limit, the interaction cross-section for a CMB photon with an electron can be described using the classical Thomson cross-section formula. For the collision process in the electron rest frame, the probability of scattering with angle θ is

$$p(\theta){\rm d}\theta = p(\mu){\rm d}\mu = (2\gamma^4(1-\beta\mu)^3)^{-1}{\rm d}\mu, \tag{1.1}$$

where the electron velocity is βc, $\gamma = 1/\sqrt{1-\beta^2}$, and $\mu = \cos\theta$. The probability of a scattering to angle θ' is

$$\phi(\mu';\mu){\rm d}\mu' = \frac{3}{8}\left(1+\mu^2\mu'^2+\frac{1}{2}(1-\mu^2)(1-\mu'^2)\right){\rm d}\mu', \tag{1.2}$$

where $\mu' = \cos\theta'$, and the change of photon direction causes a frequency shift of the scattered photon from ν to ν' and

$$\nu' = \nu(1+\beta\mu')(1-\beta\mu)^{-1}, \tag{1.3}$$

according to Chandrasekhar (1950). It's conventional to express the resulting scattering in terms of the logarithmic frequency shift $s = \log(\nu'/\nu)$. Then the probability that a single scattering of the photon causes a frequency shift s from an electron with speed βc is expressed as

$$\begin{aligned} P(s;\beta) &= \int p(\mu)\frac{{\rm d}\mu'}{{\rm d}s}\phi(\mu';\mu){\rm d}\mu \\ &= \frac{3}{16\gamma^4\beta}\int_{\mu_1}^{\mu_2}(1+\beta\mu')\left(1+\mu^2\mu'^2+\frac{1}{2}(1-\mu^2)(1-\mu'^2)\right)(1-\beta\mu)^{-3}{\rm d}\mu, \end{aligned} \tag{1.4}$$

where μ' can be expressed in terms of μ and s that

$$\mu' = \frac{e^s(1-\beta\mu)-1}{\beta}, \tag{1.5}$$

and since μ, μ' are cosine values of real angles, we have

$$\begin{aligned} \mu_1 &= -1 \text{ if } s \leq 0; \text{else } \frac{1 - e^{-s}(1+\beta)}{\beta}, \\ \mu_2 &= \quad 1 \text{ if } s \geq 0; \text{else } \frac{1 - e^{-s}(1-\beta)}{\beta}, \end{aligned} \tag{1.6}$$

and because $\mu_1 \leq \mu_2$, we can derive the minimum value of β capable of causing a frequency shift s that

$$\beta_{\min} = \frac{e^{|s|} - 1}{e^{|s|} + 1}. \tag{1.7}$$

Then, we could calculate the distribution of photon frequency shifts caused by scattering by a population of electrons using $P(s;\beta)$ by averaging over the electron β distribution. For photons that have been scattered only once, the probability distribution of s, $P_1(s)$, is given by

$$P_1(s) = \int_{\beta_{\min}}^{1} p_{\rm e}(\beta) P(s;\beta) \mathrm{d}\beta, \tag{1.8}$$

where $p_{\rm e}(\beta)$ is the electron distribution.

More generally, a photon entering the electron distribution may be scattered multiple times by encounters with the electrons. If the optical depth to scattering through the electron cloud is $\tau_{\rm e}$, then the probability that it is scattered once is $\tau_{\rm e} e^{-\tau_{\rm e}}$, and in general the probability of N scatterings follows a Poisson distribution $p_N = \tau_{\rm e}^N e^{-\tau_{\rm e}}/N!$, and the full frequency redistribution function from scattering is

$$P(s) = e^{-\tau_{\rm e}}(\delta(s) + \tau_{\rm e} P_1(s) + \frac{1}{2!}\tau_{\rm e}^2 P_2(s) + \dots). \tag{1.9}$$

The redistribution function $P_n(s)$ after n scatterings is given by a repeated convolution

$$\begin{aligned} P_2(s) &= \int P_1(s_1) P_1(s - s_1) \mathrm{d}s_1 \\ P_3(s) &= \int P_1(s_1) P_1(s_2) P_1(s - s_1 - s_2) \mathrm{d}s_1 \mathrm{d}s_2 \\ &\dots \end{aligned} \tag{1.10}$$

Finally, we are equipped with all the tools to calculate the form of the scattered spectrum of the CMB. If every photon in the incident,

$$I_0(\nu) = \frac{2h\nu^3}{c^2(e^{h\nu/k_{\rm B}T_{\rm CMB}} - 1)}, \tag{1.11}$$

then the resulting spectrum is given by

$$\frac{I(\nu)}{\nu} = \int_0^\infty P(\nu, \nu_0) \frac{I_0(\nu_0)}{\nu_0} \mathrm{d}\nu_0, \tag{1.12}$$

where $P(\nu, \nu_0)$ is the probability that a scattering occurs from frequency ν_0 to ν and $I(\nu)/h\nu$ is the spectrum in photon number terms. Since $P(\nu, \nu_0) = P(s)/\nu$, the change in the radiation spectrum at frequency ν is then

$$\begin{aligned}\Delta I(\nu) &\equiv I(\nu) - I_0(\nu) \\ &= \frac{2h}{c^2}\int P(s)(\frac{\nu_0^3}{e^{h\nu_0/k_{\rm B}T_{\rm CMB}}-1} - \frac{\nu^3}{e^{h\nu/k_{\rm B}T_{\rm CMB}}-1})\mathrm{d}s.\end{aligned} \tag{1.13}$$

Eq. (1.13) tells us an important fact that intensity change caused by the Sunyaev-Zel'dovich effect only depends on intrinsic properties of the scattering medium $P(s)$, which means it is redshift independent and is, therefore, a remarkably robust indicator of gas properties at a wide range of redshifts.

1.1.1 Thermal Sunyaev-Zel'dovich effect

This section focuses on the thermal SZ (tSZ) effect caused by the hot thermal distribution of electrons provided by the ICM of galaxy clusters. CMB photons passing through the center of a massive cluster have only $\sim 1\%$ probability of interacting with an energetic ICM electron. The resulting inverse Compton scattering preferentially boosts the energy of the CMB photon by roughly $k_{\rm B}T_{\rm e}/m_{\rm e}c^2$ causing a small ($\sim 0.1 - 1$mK) distortion in the CMB spectrum.

When the electron scattering medium is optically thin and in the non-relativistic limit, the scattering process is substantially simplified and could be well described by the Kompaneets equation (Kompaneets, 1957), which describes the change in intensity in Eq. (1.13) by a diffusion process. We could then calculate the CMB spectrum distortion caused by thermal SZ effect by replacing the $P(s)$ in Eq. (1.13) with the Kompaneets scattering kernel $P_{\rm K}(s)$ (Sunyaev & Zeldovich, 1980a; Bernstein & Dodelson, 1990), which is in form of Gaussian

$$P_{\rm K}(s) = \frac{1}{\sqrt{4\pi y}}\exp(-\frac{(s+3y)^2}{4y}), \tag{1.14}$$

where y is known as the the Comptonization parameter, expressed as

$$y = \int n_{\rm e}\sigma_{\rm T}\frac{k_{\rm B}T_{\rm e}}{m_{\rm e}c^2}\mathrm{d}l, \tag{1.15}$$

$n_{\rm e}$ is the electron number density, $\sigma_{\rm T}$ is the Thomson cross-section, $k_{\rm B}$ is the Boltzmann constant, $T_{\rm e}$ is the electron temperature, $m_{\rm e}c^2$ is the electron rest mass energy, and the integration is along the line of sight.

By adopting the $P_{\rm K}(s)$ in Eq. (1.13), we could then derive the solution for the tSZ spectral distortion of the CMB expressed as a intensity change at dimensionless frequency $x = h\nu/k_{\rm B}T_{\rm CMB}$ expressed as

$$\Delta I(\nu) = g(x)I_0 y, \tag{1.16}$$

where $I_0 = 2(k_{\rm B}T_{\rm CMB})^3/(hc)^2$ and the frequency dependence is given by

$$g(x) = \frac{x^4 e^x}{(e^x-1)^2}(x\coth(x/2) - 4). \tag{1.17}$$

The tSZ effect appears as a decrease in the intensity of the CMB at frequencies $\lesssim$ 218GHz and as an increase at higher frequencies. The temperature change is related to ΔI by the derivative of the black body radiation with respect to temperature $|{\rm d}B_\nu/{\rm d}T|$, and is given by

$$\frac{\Delta T_{\rm tSZ}}{T_{\rm CMB}} = f(x)y,\ \ f(x) = x\coth(x/2) - 4. \tag{1.18}$$

In very massive halos, the gas temperature could be around $k_{\rm B}T_{\rm e} \sim 10$keV, where electron velocities are becoming relativistic and small corrections are required for accurate interpretation of the SZ effect. There has been considerable theoretical work to include relativistic corrections to the SZ effect (e.g. Wright, 1979; Sunyaev & Zeldovich, 1980a,b; Rephaeli, 1995; Itoh et al., 1998; Dolgov et al., 2001). All of these derivations matches well as $k_{\rm B}T_{\rm e} \leq 15$keV, appropriate for galaxy clusters as the cluster mass is expect to scale with the temperature $T_{\rm e} \propto M^{2/3}$. For a very massive cluster with $k_{\rm B}T_{\rm e} \sim 10$keV, the relativistic corrections to the SZ effect are expected to be of order only a few percent in the Rayleigh-Jeans (RJ) portion of the spectrum.

An interesting fact in the SZ survey is that while the CMB suffers cosmological dimming with redshift, the ratio of the magnitude of the SZ effect to the CMB does not. The integrated SZ effect signal provides a relatively clean measure of the total thermal energy of the cluster, integrating over the solid angle of the cluster provides a sum of all of the electrons in the cluster weighted by the temperature that

$$Y_{\rm SZ} = \int \Delta T {\rm d}\Omega \propto \frac{N_{\rm e}\langle T_{\rm e}\rangle}{D_{\rm A}^2} \propto \frac{M_{\rm gas}\langle T_{\rm e}\rangle}{D_{\rm A}^2}, \tag{1.19}$$

where $N_{\rm e}$ is the total number of electrons in the clusters, $\langle T_{\rm e}\rangle$ is the mean electron temperature, $D_{\rm A}$ is the angular diameter distance, and $M_{\rm gas}$ is the total gas mass of the cluster. The integrated SZ effect flux is simply the temperature-weighted mass of the cluster divided by $D_{\rm A}^2$. Notice that angular diameter distance is fairly flat at high redshift. Also, a cluster of a given mass will be denser and therefore hotter at high redshift because the universal matter density increases as $(1+z)^3$ and the signal will be significant enough to be detected. Therefore, one expects an SZ survey to detect all clusters above some mass threshold with little dependence on redshift.

1.1.2 Kinetic Sunyaev-Zel'dovich effect

When the scattering medium causing the tSZ effect is moving relative to the Hubble flow, there will be an additional spectral distortion due to the Doppler effect of the

cluster bulk velocity on the scattered CMB photons we refer to as the kinetic SZ effect (kSZ). In the reference frame of the scattering gas, the microwave background radiation appears to be anisotropic, and the effect of the inverse-Compton scattering turns to slightly re-isotropize the radiation. The radiation field is no longer isotropic when back in the rest frame of the observer but shows a structure towards the scattering medium with amplitude proportional to $\tau_{\rm e} v_{\rm los}/c$, where $v_{\rm los}$ is the component of peculiar velocity of the scattering medium along the line of sight (Sunyaev & Zeldovich, 1972; Phillips, 1995).

In the non-relativistic limit, the spectral signature of the kSZ effect is a pure thermal distortion of magnitude

$$\frac{\Delta T_{\rm kSZ}}{T_{\rm CMB}} = -\int \frac{\sigma_{\rm T}}{c} n_{\rm e} v_{\rm los} {\rm d}l, \tag{1.20}$$

when choose the convention where $v_{\rm los} > 0$ if the electrons are moving away from the observer.

Relativistic perturbations also apply to the kSZ effect due to the Lorentz boost to the electrons provided by the bulk velocity (Sunyaev & Zeldovich, 1980a), and this perturbation is usually very small. For a very massive cluster ($\sim$ 10keV) moving at high speed ($\sim$ 1000km/s), the correction is only of order a few percent to the non-relativistic term.

In conclusion, the tSZ effect depends on random motions of the scattering electrons. It is a small spectral distortion of the CMB of order $\sim 0.1 - 1$mK and independent of redshift. It has a unique spectral signature with a decrease in the CMB intensity at frequencies $\lesssim$ 218GHz and an increase at higher frequencies. The integrated SZ effect flux is nearly independent of redshift, which implies the capability of SZ surveys for detecting all clusters above some mass threshold. The kinetic effect depends on the systematic motion of scattering media. Although the tSZ effect generally dwarfs the kSZ effect, the distinct frequency signature of the tSZ effect can be used to separate these two components. The kSZ effect also provides a method for measuring one component of the peculiar velocity of an object at a large distance and could place strong constraints on the dynamics of structure formation.

1.2 Numerical Techniques for Cosmological Simulations

Over the last decades, numerical simulations of the Universe on cosmological scales have been an important tool for advancing our understanding of the evolution and history of the large-scale structure in the Universe. As modern astronomical surveys provide enormous amounts of observational data confronting our theories of structure formation, cosmological simulations have proven very useful in developing data reduction and analysis pipelines, understanding systematics and selection effects, and interpreting cosmological and astrophysical constraints.

1.2.1 Dark Matter Simulation

Dark matter dominates the Universe over most of the cosmic time of interest for structure formation. The most favorable model, cold dark matter (CDM) model, describes the evolution of non-interacting dark matter particles with the collisionless Boltzmann equation:

$$\frac{\mathrm{d}f}{\mathrm{d}t} = \frac{\partial f}{\partial t} + \frac{\partial f}{\partial \vec{r}}\vec{v} - \frac{\partial f}{\partial \vec{v}}\frac{\partial \Phi}{\partial \vec{r}}, \tag{1.21}$$

coupled to Poisson's equation:

$$\nabla^2\Phi = 4\pi G \int f \mathrm{d}^3\vec{v}, \tag{1.22}$$

where $f = f(\vec{r}, \vec{v}, t)$ is the phase-space distribution function of dark matter, which are solved in an expanding background Universe dictated by the Friedmann equations. This set of equations represents a high-dimensional problem and is usually solved by sampling the phase-space density by a finite number N of tracer particles. The equations of motion of dark matter particles in comoving coordinates is expressed as

$$\frac{\mathrm{d}\vec{x}}{dt} = \frac{\vec{v}}{a} \tag{1.23}$$

and

$$\frac{\mathrm{d}\vec{v}}{dt} + \vec{v}\frac{\dot{a}}{a} = -\frac{\nabla\Phi}{a}, \tag{1.24}$$

where $\vec{v}$ is the proper peculiar velocity and a is the Universe scale factor.

Different approaches are employed to solve the motion of the tracer particles directly or to solve the Poisson equation. The most direct way to solve the integral form of Poisson's equation $\Phi(\vec{r}) = -G\int \rho(\vec{r}')/|\vec{r}-\vec{r}'|\mathrm{d}^3\vec{r}'$ is to sum the contributions of all the individual particles to the gravitational potential directly. However, this method has the disadvantage of being computational expensive with complexity $\propto N^2$. Tree approach (Barnes & Hut, 1986) was proposed to accelerate the direct summation through approximating the contributions to the gravitational potential from distant particles by the lowest order terms in a multipole expansion of the mass distribution at a coarse level of the tree and successfully reduce the computational cost to $\propto N \log N$. Fast multipole method (e.g. Greengard & Rokhlin, 1987; Dehnen, 2000; Zhu, 2017), which calculate the force between two tree nodes rather than between individual particles and nodes, further improve the computing time to $\propto N$.

Mesh-based methods were also employed to solve the differential form of Poisson's equation in Fourier space, $k^2\tilde{\Phi}(\vec{k}) = -4\pi G\tilde{\rho}(\vec{k})$, through fast Fourier transform-based methods, leading to the so-called particle-mesh method (Hockney & Eastwood, 1981). The complexity of the force calculation via a fast Fourier transform is only $\propto N \log N$, where N is the number of mesh cells. For a more accurate force solver for the inhomogeneous systems, adaptive-mesh-refinement schemes (Kravtsov et al., 1997) was

proposed combining the particle-mesh method with a set of nested grids of increasing resolution adapted according to the particle density.

In order to achieve high efficiency and higher fidelity, most modern simulations now implement hybrid solvers combining direct summation-based techniques for short-range forces and Fourier transform-based methods for long-range forces. Typical hybrid schemes are the particle-particle plus particle-mesh method (Efstathiou et al., 1985) and the tree-particle-mesh method (Bode & Ostriker, 2003) where the direct summation for short-range interactions is approximated by a tree-like method.

1.2.2 Hydrodynamical Simulation

Though dark matter and dark energy dominate the energy budget of the Universe, the visible components of large structures (e.g. galaxies, galaxy clusters) are consist of baryons. Hydrodynamical simulations, which also simulate the baryons mainly comprised of gas, mostly hydrogen and helium, are crucial to making predictions for the visible Universe. Astrophysical gases in cosmological simulations can typically be described as an ideal fluid. Therefore, the evolution of the fluid is usually described by solving the set of hydrodynamic equations: the Euler equation, continuity equation, and the first law of thermodynamics, expressed in the form of Lagrangian formulation as

$$\frac{\mathrm{d}\vec{v}}{\mathrm{d}t} = -\frac{\nabla P}{\rho} - \nabla\Phi, \tag{1.25}$$

$$\frac{\mathrm{d}\rho}{\mathrm{d}t} = -\rho\nabla\cdot\vec{v}, \tag{1.26}$$

and

$$\frac{\mathrm{d}u}{\mathrm{d}t} = -\frac{P}{\rho}\nabla\cdot\vec{v}. \tag{1.27}$$

Equation of state assuming ideal gas $P = (\gamma - 1)\rho u$ relates the pressure P to the internal energy u and closes the hydrodynamic equations above.

Numerical techniques of hydrodynamical simulations can be classified into two main types:

1. Lagrangian Methods: assumes an observer that follows an individual fluid parcel, with its own properties like density, as it moves through space and time, Smoothed Particle Hydrodynamics (SPH) is one of the most widely used mesh-free Lagrangian techniques (e.g. Gingold & Monaghan, 1977; Springel, 2010a; Price, 2012) for approximating the continuum dynamics of fluids through the use of sampling particles, following the equations of motion derived from the hydrodynamical equations.

2. Eulerian Methods: focuses on specific locations in space through which the fluid flows as time passes, modern implementations of Eulerian methods employ parabolic interpolation, known as the piecewise parabolic method (e.g. Colella

& Woodward, 1984; Woodward, 1986). Adaptive-mesh-refinement schemes (e.g. Klein et al., 1994; Bryan & Norman, 1995) which reduce the mesh size based on some refinement criterion were also applied to cosmological simulations of large dynamic range.

In addition to traditional methods for hydrodynamical simulations, a new type of scheme, referred to as the arbitrary Lagrangian-Eulerian methods (e.g. Springel, 2010b; Hopkins, 2015), recently has been realized through a Voronoi tessellation of a set of discrete mesh-generating points where the mesh continuously deforms and changes its topology as the points are allowed to move freely. This new type of simulation has been successfully applied to astrophysical and galaxy formation problems.

In order to make predictions for the large structures what observational efforts to detect in the Universe, hydrodynamical equations also have to be complemented by various astrophysical processes like gas cooling, star formation, feedback from active galactic nuclei, magnetic fields, and other physics. In practice, hydrodynamical simulations implement most of these processes employing effective, so-called subresolution models, which are necessary due to the limited numerical resolution of simulations. A more detailed review of baryonic physics implemented in simulation is given by Vogelsberger et al. (2020).

1.2.3 Rapid Simulation Methods

Nowadays, the effective volumes of modern surveys keep growing, and achieving the science goals of these surveys requires numerical simulations of exceptionally large volumes - both for correctly capturing the statistics of the rare objects and for computing the covariance matrices between the observables. Simulations in spatial volumes comparable to the surveys in size are generally too expensive to make many large-scale mock observations and explore both astrophysical and cosmological parameter space. In the face of increasing demand for multiple realizations of simulated mock catalogs for comparison with the large-scale structure observations, fast approximate approaches for dark matter simulations based on semi-numerical methods and lagrangian perturbation theory have been developed.

A fast algorithm, PTHALOS (Scoccimarro & Sheth, 2002), has been used to generate realistic non-Gaussian galaxy distributions. PTHALOS generate the large-scale dark matter distribution using second-order lagrangian perturbation theory (2LPT) to determine the masses and positions of virialized halo centers and then distribute particles around the halo centers with realistic density profiles. It shows the capability of generating realistic galaxy distributions in a very small fraction of the time it takes for methods that require N-body simulations of gravitational clustering. PINOCCHIO (Monaco et al., 2002) adopt a new idea for identifying dark matter halos in a given numerical realization of the linear density field in a hierarchical universe. In PINOCCHIO, mass elements are assumed to have collapsed after undergoing orbit crossing. Such points are then grouped into halos using an algorithm that mimics

the hierarchical growth of structure through accretion and mergers. The Zel'dovich approximation is used to compute the Eulerian positions of halos at a given time. Some points that have undergone orbit crossing are also assigned to the network of filaments and sheets that connects the halos. It has been shown that the predictions of the PINOCCHIO code are very accurate when compared with the results of large N-body simulations but only requires negligible computer time as compared with performing a numerical N-body simulation.

Recently, a new N-body method, COLA (Tassev et al., 2013), was proposed for solving Large Scale Structure (LSS) in a frame that is comoving with observers following trajectories calculated in LPT. The analytic calculation from 2LPT governs the large-scale displacement, and the PM is only used to solve for the "residual" small-scale displacement that affects the formation of haloes. COLA has been used for cheaply generating large ensembles of accurate mock halo catalogs required to study galaxy clustering and weak lensing, which are essential for performing detailed error analysis for ongoing and future surveys of LSS. FastPM (Feng et al., 2016a), a new implementation of an approximate PM N-body solver as the up-and-comer modifies the standard kick and drift factors such that it agrees with Zel'dovich solution on large scales and guarantee zero error for large scales even for very few time steps.

Though we have seen significant progress in various approaches aiming to speed up dark matter only N-body simulations, there is still a notable lack of fast approximate hydro simulation methods. Previously, Gnedin & Hui (1998) used the particle-mesh (PM) solver for dark matter dynamics and allowed for the additional gas pressure force to approximate hydrodynamics. Their hydro-particle-mesh (HPM) algorithm substantially relies on the existence of a tight temperate-density relation in the intergalactic medium (IGM) and has been successfully used to model the high-redshift Lyman alpha forest with moderate precision (McDonald et al., 2002).

However, the tight correlation between the gas density and temperature in the low-density IGM breaks down in denser regions. Yet, it is possible to extend the range of validity of HPM-like techniques further. My thesis mainly focuses on developing a fast approximate method for modeling hydrodynamics in the high-density ICM, which can be implemented through building a mapping relation based on empirical or simulated ICM pressure profiles (e.g. Arnaud et al., 2010; Battaglia et al., 2012; He et al., 2021a) between the gas temperature or pressure and some properties of cosmic gas that can be captured by, say, a simple PM solver. The gas physics can then be modeled very efficiently in both the IGM and the ICM regime, which together fill most of the spatial volume in a fast hydro simulation.

1.3 Thesis Outline

Our discussions of developing the cosmological HYPER code based on an innovative HPM algorithm and using HYPER to study cosmology with the SZ effect consist of three parts. In Chapter 2, we construct a model for the estimation of hydrostatic mass bias by combining results from X-ray observations with cosmological simulations. We also come up with an analytical model for the average cluster pressure profile by applying our finds for hydrostatic mass bias to the REXCESS X-ray cluster sample. In Chapter 3, I introduce our implementation of the HYPER code in detail. I describe how we achieve high efficiency and high fidelity for the approximate hydrodynamics solver using the dark matter halo model, ICM pressure profile, and IGM temperature-density relation. I show that the HYPER simulation results are in good agreement with the halo model expectations for the density, temperature, and pressure radial profiles. Simulated galaxy cluster scaling relations for Sunyaev-Zel'dovich and X-ray observables are also found in good agreement with mean predictions, with scatter comparable to that found in hydrodynamic simulations. I emphasize one crucial strength of HYPER: it allows for systematically varying the ICM and IGM models to study different baryonic physics and effects. I also bring out some perspectives of the use cases for HYPER simulation and discuss the future code development extensions in this chapter. I discuss the application of HYPER in SZ science in Chapter 4. A template is proposed for calculating the thermal and kinetic SZ angular power spectra using the outputs of HYPER simulations. I also show that this template can be used for constraining cosmological parameters in the analyses of future SZ surveys. In Chapter 5, I discuss some general conclusions and avenues that remain for future work.

Chapter 2

Debiased Galaxy Cluster Pressure Profiles from X-ray Observations and Simulations

2.1 Introduction

Galaxy clusters are formed by the gravitational collapse of large overdensities and are accompanied by a complex interplay of gravity and baryonic processes. They are ideal probes to study dark energy and the evolution of large scale structure (e.g. Voit, 2005; Allen et al., 2011), and their abundance is sensitive to cosmology, meaning that accurate measurements of the cluster mass function and its evolution can provide meaningful cosmological constraints and further our understanding of cosmology in upcoming cluster surveys.

Galaxy clusters have deep gravitational potential wells, and the potential energy of material falling into clusters leads to shock-heating of the gas. This hot, ionized gas emits X-rays through bremsstrahlung radiation, making clusters of galaxies the most common, bright, extended extragalactic X-ray sources. It also makes X-ray observation one of the most attractive methods to detect and characterize galaxy clusters. Due to tight X-ray observable-mass relations, the X-ray temperature $T_{\rm X}$, gas mass $M_{\rm g}$, $Y_{\rm X} = T_{\rm X} M_{\rm g}$ and X-ray luminosity $L_{\rm X}$ inferred from X-ray spectroscopy, have been used as robust mass proxies of galaxy clusters (e.g. Arnaud et al., 2007). The ACT and the Planck collaborations (e.g. Hasselfield et al., 2013; Planck Collaboration et al., 2016c; Hilton et al., 2018) have been used stacked pressure profiles of the Intracluster Medium (ICM) in galaxy clusters (Arnaud et al., 2010; see also, Nagai et al., 2007a), modeled on X-ray measurements, to interpret survey data of the SZ effect (Sunyaev & Zeldovich, 1970b), represented as a distortion in the spectrum of the cosmic microwave background (CMB) due to relic CMB photons inverse Compton scattering off energetic electrons in the galaxy clusters.

When estimating cluster masses from X-ray measurements of density and temper-

ature profiles of the ICM, clusters are generally assumed to be in a dynamical state of hydrostatic equilibrium. However, in the hierarchical structure formation model, galaxy clusters are dynamically active systems and are not in exact hydrostatic equilibrium. Both the latest observations (e.g. Bautz et al., 2009; George et al., 2009; Reiprich et al., 2009; Hoshino et al., 2010; Kawaharada et al., 2010; Urban et al., 2011; Simionescu et al., 2011; Hitomi Collaboration et al., 2018; Siegel et al., 2018) and numerical simulations (e.g. Evrard, 1990; Rasia et al., 2004; Lau et al., 2009; Battaglia et al., 2012; Nelson et al., 2012; Lau et al., 2013; Nelson et al., 2014; Gupta et al., 2017) find non-thermal gas processes like virialized bulk motions and turbulent gas flows, generated primarily by mergers and accretion during cluster formation, lead to non-trivial pressure support especially in the outskirt of galaxy clusters. Analytical models have also been developed to describe the non-thermal pressure support in intracluster gas and found that it was in excellent agreement with high resolution cosmological hydrodynamic simulations (e.g. Shi & Komatsu, 2014; Shi et al., 2015).

Recent work suggests that neglecting the existence of non-thermal pressure in X-ray observations causes systematic underestimation of the hydrostatic masses of galaxy clusters and is a major source of bias in the inferred hydrostatic masses. This is referred to as hydrostatic mass bias. Studies have shown that correcting the absence of non-thermal pressure in hydrostatic equilibrium will help mitigate the tension between cluster mass estimates from weak lensing surveys and from X-ray surface brightness and SZ observations (e.g. Shi et al., 2016).

Hydrostatic mass bias has often been assumed to be a constant, parameterized in terms of $b = 1 - M_{\rm X/SZ}/M_{\rm WL}$ where $M_{\rm X/SZ}$ refers to hydrostatic masses obtained from X-ray or SZ observation and $M_{\rm WL}$ refers to results of weak-lensing measurements. Observations giva a range of biases $b = 5 - 30\%$ (e.g. von der Linden et al., 2014; Hoekstra et al., 2015; Simet et al., 2015; Simet et al., 2016; Battaglia et al., 2016; Smith et al., 2016; Penna-Lima et al., 2017; Sereno et al., 2017; Medezinski et al., 2018). Numerical simulations (e.g. Nagai et al., 2007b; Battaglia et al., 2012; Kay et al., 2012; Rasia et al., 2012; Le Brun et al., 2014) also point to typical mass biases around b=0.20. That hydrostatic bias could depend on cluster mass was not proposed until recently (e.g. Rasia et al., 2012): Henson et al. (2017) find that mass bias climbs from 0.20 to 0.40 as cluster masses increase from $M_{\rm 500c} = 10^{14}$ to $10^{15} h^{-1} M_{\odot}$. Barnes et al. (2020) introduced the Mock-X analysis framework, a multi-wavelength tool that generates synthetic images from cosmological simulations and derives directly observable and reconstructed properties from these images via observational methods, and applied this framework to explore hydrostatic mass bias for the IllustrisTNG (e.g. Pillepich et al., 2018a; Nelson et al., 2018; Naiman et al., 2018; Marinacci et al., 2018; Springel et al., 2018), BAHAMAS (McCarthy et al., 2017a), and MACSIS (Barnes et al., 2017) simulations. They find hydrostatic bias recovered from synthetic X-ray images which shows a significantly stronger mass dependence, increasing from $b = 0.0$ at $10^{14} M_{\odot}$ to $b = 0.2$ at $2 \times 10^{15} M_{\odot}$. Both studies claim that the key factor causing this mass dependence is the increase in dense, cold gas in cluster outskirts as

mass increases. The quadratic dependence of X-ray emission on density causes this cool gas to lower mass estimates for the most massive clusters. Carefully treating hydrostatic mass bias in the recalibration of the ICM pressure models derived from X-ray observation is crucial for better interpreting the angular power spectrum of the thermal SZ signal, reducing systematic uncertainties in cosmological parameters.

This chapter is organized as follows. In Section 3.3, we begin by introducing an analytical approach for correcting hydrostatic mass bias in clusters based on the "true" simulated mass and the X-ray mass of clusters drawn from the IllustrisTNG, BAHAMAS and MACSIS simulations. We then discuss how to apply this model to the best-fit Generalized Navarro–Frenk–White (GNFW; Zhao, 1996) ICM pressure profiles measured in X-ray surveys. In Section 3.4, we apply the correction discussed in Section 3.3 to the X-ray measurements of cluster masses and the GNFW fit correction to the scaled pressure profiles of the REXCESS cluster sample (Böhringer et al., 2007). We use the corrected characteristic pressures and masses of the REXCESS sample to modify the Universal Pressure Profile (UPP), which gives us a new model for cluster pressures: the Debiased Pressure Profile (DPP). We use the DPP to study the power-law relation between the integrated Compton parameter and cluster mass. We also calculate the thermal Sunyaev-Zeldovich (tSZ) angular power spectrum with the DPP, and compare with Planck, ACT, and SPT measurements of the tSZ power spectrum. In Section 2.4, we conclude our findings for the mass bias of clusters in the REXCESS sample, the self-similarity of both the new pressure model and the $Y - M$ relation, and the change in amplitude of the tSZ angular power spectrum we get based on the new pressure model. In the end, we also bring up the remaining questions and possible directions for future work. We adopt the following cosmological parameters: $\Omega_m = 0.3,\ \Omega_\Lambda = 0.7,\ \Omega_b = 0.045,\ h = 0.7,\ n_s = 0.96,\ \sigma_8 = 0.8$ in this chapter.

2.2 Methods

2.2.1 $M_{500c}^{\rm True}$ v.s. $M_{500c}^{\rm X-ray}$ of Mock-X

For a spherically symmetrical cluster, hydrostatic equilibrium occurs when the the force of gravity exerted on gas in the cluster is balanced by the gradient of gas pressure:

$$\frac{{\rm d}P(r)}{{\rm d}r} = -\rho_{\rm gas}(r)\frac{GM(<r)}{r^2}, \tag{2.1}$$

with the gravitational constant, G, enclosed mass profile, $M(<r)$, gas pressure profile, $P(r)$, and gas density profile, $\rho_{\rm gas}(r)$, all with respect to the distance r from the center of the cluster. A combination of X-ray observations like XMM$-Newton$, CHANDRA and analysis technique taking into account projection and PSF effects have achieved high resolution measurements of the radial electron density profiles, $n_{\rm e}(r)$, and the radial temperature profiles, $T(r)$, of galaxy clusters (e.g. Vikhlinin et al., 2006; Croston et al., 2008), which can be used to determine the radial electron pressure profile,

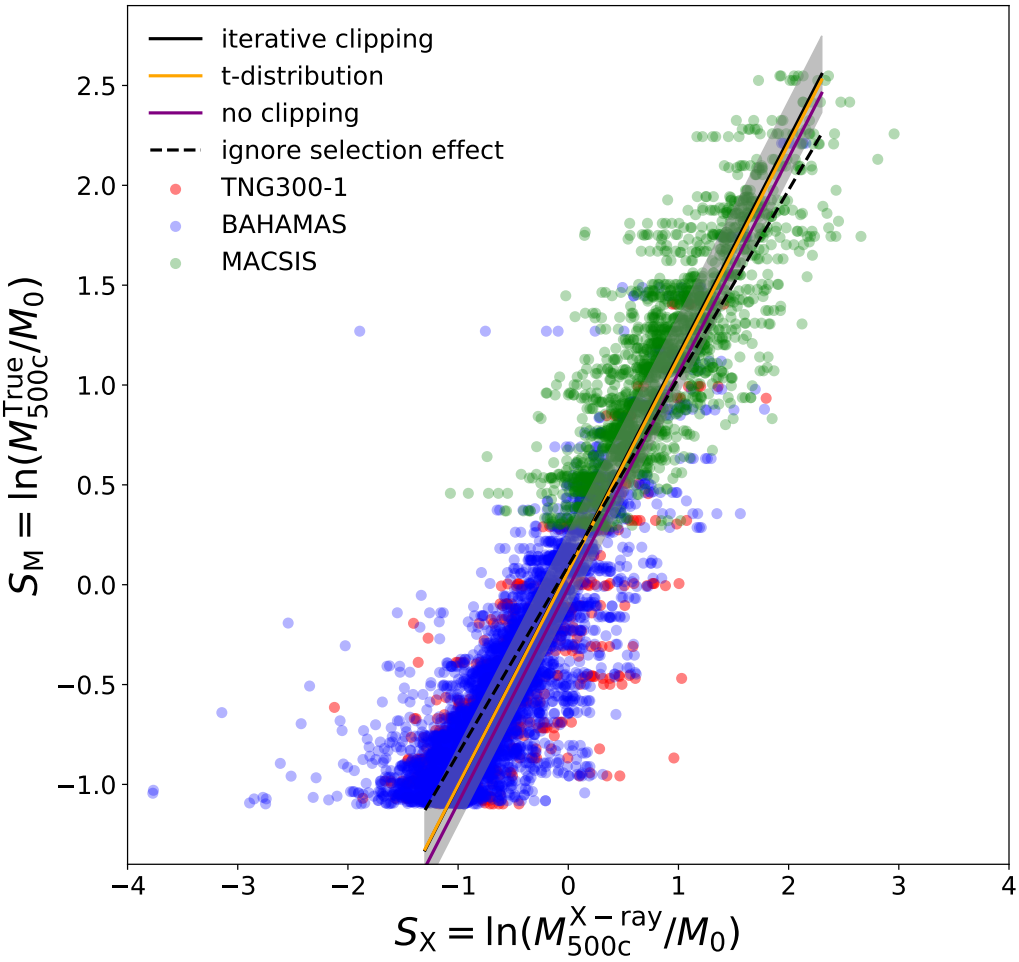

Figure 2.1: Normalized "true" masses (M_{500c}^{True}/M_0) vs. X-ray masses (M_{500c}^{X-ray}/M_0) for clusters from the IllustrisTNG (red), BAHAMAS (blue), and MACSIS (green) simulations are shown by a scatter plot. The power-law regression described in section 2.2.1 (solid black line) and the corresponding 68% scatter (gray shaded region), defined by regression parameter σ, is plotted over the cluster data. This fiducial approach – based on iterative clipping – is consistent with an alternative fit which does not perform clipping but uses a truncated t-distribution to account for outliers (solid orange line). Outlier removal has a modest but statistically significant effect on fit results, as shown by a fit which did not account for outliers (solid purple line), but failing to account for mass selection effects (dashed black line) results in a substantially different power-law index.

$P_e(r)$, by assuming an ideal gas equation of state, $P_e(r) = k_B n_e(r) T(r)$. Given the electron pressure, the gas thermal pressure P_{th} is defined by $P_{th}(r) = P_e(r)\mu_e/\mu$ where μ is the mean mass per gas particle, and μ_e is the mean mass per electron.

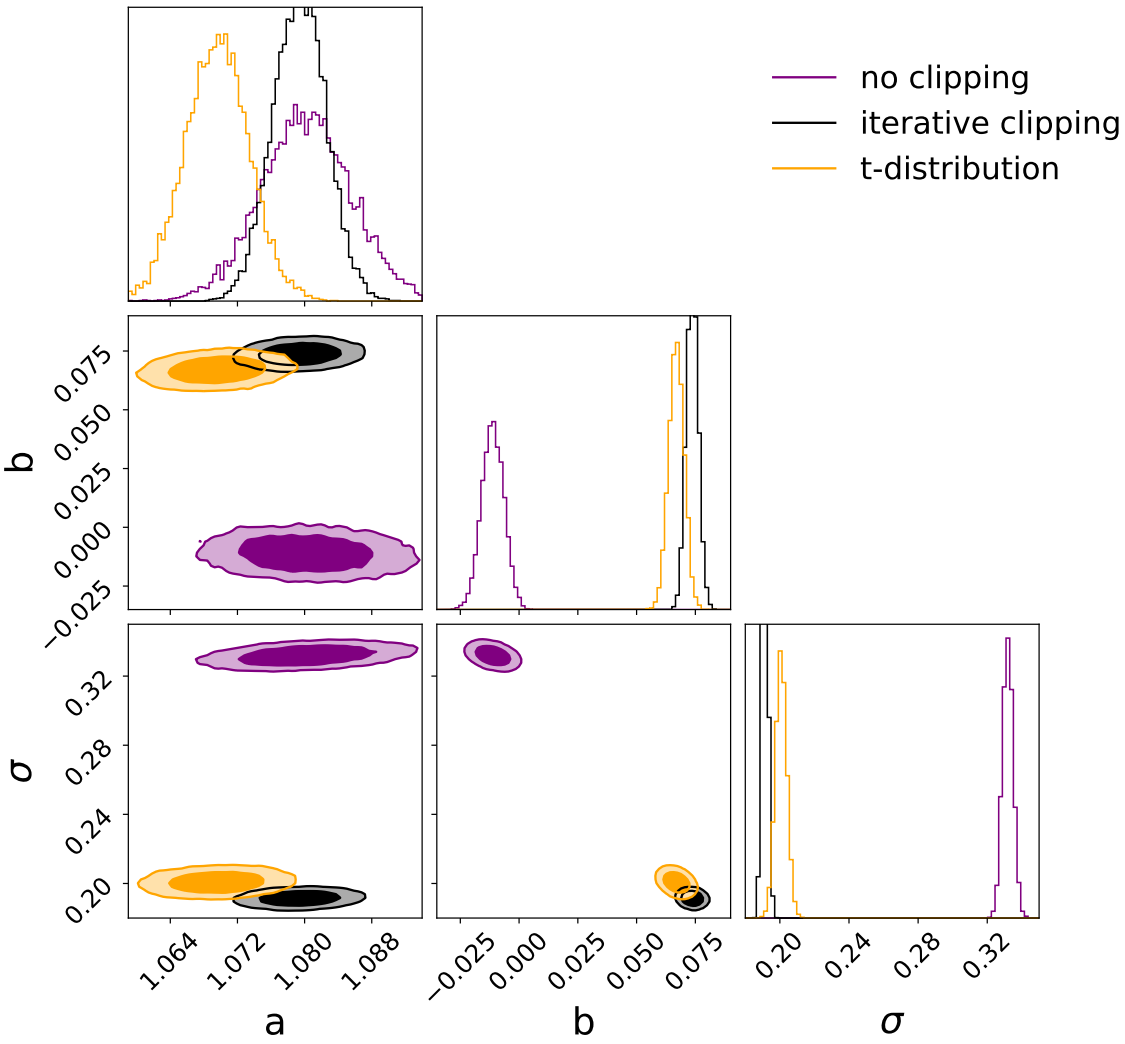

Figure 2.2: Marginalized (1D and 2D) joint posterior probability distributions of the regression model parameters. The dark and light contours show 68% and 95% confidence level respectively.

In addition to the thermal motion of the gas, other sources of gas pressure - including viralized bulk motion, turbulence, cosmic rays, and magnetic fields - also provide non-trivial pressure support (e.g. Ensslin et al., 1997; Churazov et al., 2008; Brüggen & Vazza, 2015). For realistic equilibrium systems, the gas pressure, P, in Eq. 2.1 is replaced by $P = P_{\rm th} + P_{\rm nth}$, where $P_{\rm nth}$ refers to any non-thermal pressure acting on the intracluster gas. X-ray-measured cluster masses are derived from the assumption of hydrostatic equilibrium with only thermal gas pressure, which means that the contribution of non-thermal pressure can cause X-ray measurements to underestimate cluster masses systematically.

Numerical simulations provide a vital resource for characterizing the mass bias as the properties of simulated galaxy clusters are known exactly. Barnes et al. (2020) developed the Mock-X analysis framework, which can generate synthetic X-ray images and derives halo properties (e.g. gas density and temperature profiles) via observational methods, which can be used to derive hydrostatic mass in mock X-ray observations. Hydrostatic mass bias is equal to the ratio of the hydrostatic mass to the "true" (overdensity) mass of simulated clusters identified through SUBFIND (e.g. Springel et al., 2001; Dolag et al., 2009) in simulations. Studies (e.g. Henson et al., 2017; Barnes et al., 2020) also point out that the bias of hydrostatic mass estimated with density and temperature profiles derived from the spectroscopic analysis show a much stronger mass-dependence than those estimated from the true mass-weighted temperature profiles. These simulated spectroscopic temperatures emulate the observational procedure for measuring X-ray temperatures and thus we compare against them in this analysis.

A number of the aforementioned numerical studies have measured $M_{500c}^{\mathrm{X-ray}}/M_{500c}^{\mathrm{True}}$. However, observationally, one only has access to $M_{500c}^{\mathrm{X-ray}}$. This means that we must invert these relations to give $M_{500c}^{\mathrm{True}}/M_{500c}^{\mathrm{X-ray}}$ as a function of $M_{500c}^{\mathrm{X-ray}}$ (a deceptively complex task). Here, M_{500c} is the "overdensity mass" and corresponds to the mass within a spherical boundary which has an average density equal to 500 times the critical density, ρ_{crit}.

In this work, we present an efficient approach to estimate the true cluster mass by utilizing both the X-ray and "true" masses of simulated clusters, M_{500c}^{True} from Barnes et al. (2020). We adopt a power-law model for the scaling relation between M_{500c}^{True} and $M_{500c}^{\mathrm{X-ray}}$. This is a linear model in logarithmic scale. For convenience, we denote

$$\begin{aligned} S_{\mathrm{X}} &= \ln(M_{500c}^{\mathrm{X-ray}}/M_0), \\ S_{\mathrm{M}} &= \ln(M_{500c}^{\mathrm{True}}/M_0), \end{aligned} \tag{2.2}$$

with $M_0 = 3 \times 10^{14} M_\odot$. For fixed S_{X}, we assume a linear relation between S_{M} and S_{X} where the error, ϵ, follows a Gaussian distribution:

$$S_{\mathrm{M}} = aS_{\mathrm{X}} + b + \epsilon, \tag{2.3}$$

$$\epsilon \sim \mathrm{Norm}(0, \sigma^2), \tag{2.4}$$

where a, b, σ are free parameters.

We notice that clusters drawn from simulations are selected in terms of a certain mass threshold, which means we also need to consider this selection effect in our model when fitted to simulation data. For given S_{X} and S_{M} of a simulated cluster, we use a truncated normal distribution to model the likelihood

$$p(S_{\mathrm{M}}|S_{\mathrm{X}}, S_{\mathrm{T}}, \vec{\theta}) = \frac{A(S_{\mathrm{X}}, S_{\mathrm{T}}, \theta)}{\sqrt{2\pi\sigma^2}} \exp\left[\frac{(aS_{\mathrm{X}} + b - S_{\mathrm{M}})^2}{2\sigma^2}\right], \tag{2.5}$$

where $\vec{\theta} = (a, b, \sigma)$ denotes the free parameters. S_{T} is the truncation parameter defined by $S_{\mathrm{T}} = \log(M_{500c}^{\mathrm{T}}/M_0)$ and M_{500c}^{T} is the mass threshold for a given simulated

cluster sample. $A(S_{\rm T}, S_{\rm X}, \vec{\theta})$ is the normalization factor for a normal distribution, $\mathrm{Norm}(aS_{\rm X}+b, \sigma^2)$, truncated with a lower bound $S_{\rm T}$:

$$A(S_{\rm T}, S_{\rm M}, \vec{\theta}) = \left[1 - \Phi\left(\frac{S_{\rm T} - aS_{\rm X} - b}{\sigma}\right)\right]^{-1}, \tag{2.6}$$

where Φ denotes the cumulative distribution function (CDF) of standard normal. We set

$$a, b \sim \mathcal{U}(-5, 5) \tag{2.7}$$
$$\sigma \sim \mathcal{U}(0, 5) \tag{2.8}$$

as priors, where $\mathcal{U}$ denotes the uniform distribution. We can then write out the posterior for the parameters

$$p(\vec{\theta}|D) \propto p(a)p(b)p(\sigma) \prod_{\alpha} \left[\prod_{i=1}^{N_\alpha} p(S^i_{{\rm M},\alpha}|S^i_{{\rm X},\alpha}, S_{{\rm T},\alpha}, \vec{\theta})\right], \tag{2.9}$$

where $D = \{D_1, D_2, D_3\}$ is a data vector of log-scaled masses of simulated cluster sample drawn from IllustrisTNG, BAHAMAS and MACSIS simulations denoted by $\alpha = 1, 2, 3$, and $D_\alpha = \{(S^i_{{\rm M},\alpha}, S^i_{{\rm X},\alpha}), i = 1, \ldots N_\alpha\}$. Each simulation uses a different $S_{{\rm T},\alpha}$. Mass thresholds, $M^{\rm T}_{\rm 500c}$, are set to be $10^{14} M_\odot$ for IllustrisTNG and BAHAMAS, and $4 \times 10^{14} M_\odot$ for MACSIS. Details about these simulations can be found in Barnes et al. (2020).

We note that the IllustrisTNG, BAHAMAS, and MACSIS simulations adopt different numerical methods or subgrid physics, which may introduce differences in the derived cluster profiles and systematics in the mass estimation of the mock X-ray observation. This will be accounted in the intrinsic scatter in our regression model for the relation of $M^{\rm True}_{\rm 500c}$ v.s. $M^{\rm X-ray}_{\rm 500c}$ since the fit is performed on all simulations simultaneously.

We explore the parameter space by Markov Chain Monte Carlo (MCMC), using `emcee` (Foreman-Mackey et al., 2013) for the sampling. We discard the initial steps suggested by the integrated autocorrelation time (Foreman-Mackey et al., 2019), which estimate the number of steps that are needed before the chain "forgets" where it started. This step ensures the samples well "burnt-in". Regression results for the linear model and uncertainty are reported in Table 2.1.

A small fraction, $\sim$9%, of simulated clusters have abnormally high or abnormally low $M^{\rm True}_{\rm 500c}/M^{\rm X-ray}_{\rm 500c}$, suggesting ratios outside the observed range (e.g. Miyatake et al., 2019). Most cases appear in low-mass clusters, and may be due to the numerical noise when resolving the X-ray mass of simulated clusters from synthetic images. The steep slope of the mass function causes these unreliable low-mass data points to significantly influence the mean $M^{\rm True}_{\rm 500c}$ at high $M^{\rm X-ray}_{\rm 500c}$. In addition to the numerical noise, merging events, or certain AGN activities in the unrelaxed clusters could lead

to a less spherical cluster. The thermodynamic profiles and corresponding X-ray mass of these less regular clusters will be recovered with more systematic uncertainty because clusters' profiles and masses are derived assuming spherical symmetry in the Mock-X analysis (Barnes et al., 2020), which could also result in an extreme value of $M_{500c}^{\rm True}/M_{500c}^{\rm X-ray}$. For a more concrete conclusion, detailed studies are required for these peculiar cluster samples with abnormal values of $M_{500c}^{\rm True}/M_{500c}^{\rm X-ray}$ in the future work.

To mitigate the effect introduced by the simulated clusters with extreme values of $M_{500c}^{\rm True}/M_{500c}^{\rm X-ray}$, we iteratively remove outlier clusters falling outside the 2σ region of the regression results until the prediction for $M_{500c}^{\rm True}$ derived from the linear model for $M_{500c}^{\rm True}$ v.s. $M_{500c}^{\rm X-ray}$ converges to 1% agreement with the previous iteration. This is performed for clusters within the X-ray mass range $M_{500c}^{\rm X-ray} = 10^{14} - 10^{15} M_{\odot}$. To test the impact of this method for removing outliers, we also used a truncated t-distribution (e.g. Pfanzagl & Sheynin, 1996) to model the uncertainty, ϵ, which is another approach to alleviate the effect of outlier samples.

In Figure 2.1, we plot $S_{\rm M}$ v.s. $S_{\rm X}$ for the IllustrisTNG, BAHAMAS, and MACSIS cluster samples. We also show the regression results for the linear relation between log-scaled "true" and X-ray masses, considering both truncation effects and the influence of outlier clusters. The intrinsic scatter in our linear model is determined by the parameter σ. We find the slope parameter $a = 1.079$ is greater than 1, which indicates the ratio of $M_{500c}^{\rm True}$ to $M_{500c}^{\rm X-ray}$ is mass-dependent, and hydrostatic mass bias increases with cluster mass. We also plot the regression results for the linear relation by modeling the uncertainty, ϵ, with a truncated t-distribution. For comparison, we also show regression results without removing outlier clusters and without modeling truncation effects. In Figure 2.2, we plot marginalized (1D and 2D) joint posterior probability distributions of the regression model parameters to directly compare regression results of different fitting methods in parameter space.

The alternative fit for $M_{500c}^{\rm True}$ v.s. $M_{500c}^{\rm X-ray}$, which does not perform clipping but uses a truncated t-distribution to account for outliers, is in good agreement with the results of iterative 2σ clipping methods. Regression results of the two methods find similar values for the slope parameter and the discrepancy between $M_{500c}^{\rm True}$ for $10^{14} M_{\odot} < M_{500c}^{\rm X-ray} < 10^{15} M_{\odot}$ is at the $\sim 1\%$ level. Comparing with the fit which did not account for outliers, we find outlier removal has a modest but statistically significant effect on fit results. We also find failing to account for mass selection effects results in a bad fit to the simulation data and a substantially different power-law index.

2.2.2 Hydrostatic Bias for Pressure Models

When we fit an analytical model like a GNFW profile to the radial pressure profile of a galaxy cluster, a common approach taken is to normalize the pressure and radius by the characteristic pressure P_{500c} and radius R_{500c}, both of which can be directly com-

Model parameters	a	b	σ
iterative clipping	1.079 $\pm$0.003	0.074 $\pm$0.002	0.191 $\pm$0.001
t-distribution	1.070 $\pm$0.004	0.067 $\pm$0.003	0.201 $\pm$0.002
no clipping	1.080 $\pm$0.005	-0.011 $\pm$0.005	0.332 $\pm$0.003

Table 2.1: Best-fitting parameters for Eq. 2.3 for the cluster data from the IllustrisTNG, BAHAMAS, and MAC-SIS simulations. Each row shows a different method for accounting for outlier clusters.

puted at a given cluster mass. If the mass of galaxy clusters in X-ray measurements suffers from hydrostatic bias, the characteristic pressure and radius will as well. For convenience, we define a new variable for the hydrostatic mass bias,

$$B_{\rm M} = M_{\rm 500c}^{\rm True}/M_{\rm 500c}^{\rm X-ray}, \tag{2.10}$$

then the radius bias, $B_{\rm R}$, and pressure bias, $B_{\rm P}$, can be obtained from scaling relations, although the latter relies on the assumption of a specific model for the pressure profile. For a spherical cluster, $R_{\rm 500c} \propto M_{\rm 500c}^{1/3}$, so hydrostatic bias for cluster radius is defined by

$$B_{\rm R} = B_{\rm M}^{1/3}. \tag{2.11}$$

If we assume that pressure follows a GNFW profile given by $P(r) = P_{\rm 500c}(M_{\rm 500c}, z)\mathbb{P}(x)$ (Nagai et al., 2007a), where $x = r/R_{\rm 500c}$ and

$$\begin{aligned} P_{\rm 500c}(M_{\rm 500c}, z) =& 1.65 \times 10^{-3} h(z)^{8/3} \\ & \times \left[\frac{M_{\rm 500c}}{3 \times 10^{14} M_\odot}\right]^{2/3} h_{70}^2 \,{\rm keV\,cm^{-3}}, \end{aligned} \tag{2.12}$$

$\mathbb{P}(x)$ is the scaled profile, with the form

$$\mathbb{P}(x) = \frac{P_0}{(c_{\rm 500}x)^\gamma \left[1 + (c_{\rm 500}x)^\alpha\right]^{(\beta-\gamma)/\alpha}}, \tag{2.13}$$

where $c_{\rm 500}$ is the concentration, P_0 is the normalization parameter, and the parameters α, β, γ determine the power-law slopes of different region of the cluster. Since $P_{\rm 500c} \propto M_{\rm 500c}^{2/3}$ according to Eq. 2.12, the pressure bias is

$$B_{\rm P} = B_{\rm M}^{2/3}. \tag{2.14}$$

The bias parameters $B_{\rm R}$ and $B_{\rm P}$ can be used to debias GNFW fits to X-ray measurements of thermal pressure profiles by rescaling c_{500} and P_0 with the following bias correction factors:

$$c_{500} = c_{500}^{\rm bias} \times B_{\rm R}, \tag{2.15}$$

$$P_0 = P_0^{\rm bias}/B_{\rm P}. \tag{2.16}$$

We note that radius and pressure biases have a one-to-one relation with $B_{\rm M}$, so uncertainty in $B_{\rm M}$ can be converted to $B_{\rm R}$ and $B_{\rm P}$ by

$$\sigma_{\ln B_{\rm R}} = \sigma_{\ln B_{\rm M}}/3, \sigma_{\ln B_{\rm P}} = 2\sigma_{\ln B_{\rm M}}/3. \tag{2.17}$$

2.3 Results

2.3.1 Mass Adjustment of the REXCESS Sample

We apply our linear model for $S_{\rm M}$ vs. $S_{\rm X}$ to the hydrostatic X-ray masses of the REXCESS cluster sample to estimate the true masses of these clusters. REXCESS is a representative sample of local clusters at redshifts $0.0 < z < 0.2$ which spans a mass range of $10^{14}M_{\odot} < M_{500c} < 10^{15}M_{\odot}$ (Arnaud et al., 2010). REXCESS clusters are drawn from the REFLEX catalog and were studied in-depth by the $XMM-Newton$ Large Programme. A description of the REFLEX sample and of $XMM-Newton$ observation details can be found in Böhringer et al. (2007). We correct the hydrostatic mass of 31 local clusters from the REXCESS sample measured by X-ray observation,

$$M_{\rm 500c}^{\rm True}/M_0 = e^b \times (M_{\rm 500c}^{\rm X-ray}/M_0)^a, \tag{2.18}$$

where a and b are the regression parameters for the linear model reported in Table 2.1. We find that the X-ray measured hydrostatic masses of clusters in the REXCESS sample are underestimated by approximately 7% on average. The bias climbs from 0% to 15% as cluster X-ray mass increases from $10^{14}M_{\odot}$ to $10^{15}M_{\odot}$.

The regression parameter σ is the intrinsic scatter in $S_{\rm M} = \ln(M_{\rm 500c}^{\rm True}/M_0)$ and can be used to characterize the uncertainty in the corrected mass of REXCESS clusters at a given predicted $M_{\rm 500c}^{\rm True}$:

$$\sigma_{M_{\rm 500c}^{\rm True}} \simeq M_{\rm 500c}^{\rm True}\sigma. \tag{2.19}$$

With the first order approximation, this scatter yields significant uncertainties for individual objects, around ≈20%, for corrected cluster masses. σ also defines scatter in the mass bias $B_{\rm M}$, radius bias $B_{\rm R}$, and pressure bias $B_{\rm P}$ in log scale:

$$\sigma_{\ln B_{\rm M}} = \sigma, \sigma_{\ln B_{\rm R}} = \sigma/3, \sigma_{\ln B_{\rm P}} = 2\sigma/3. \tag{2.20}$$

These allow us to estimate the modeling uncertainty in the debiased pressure, radius and mass.

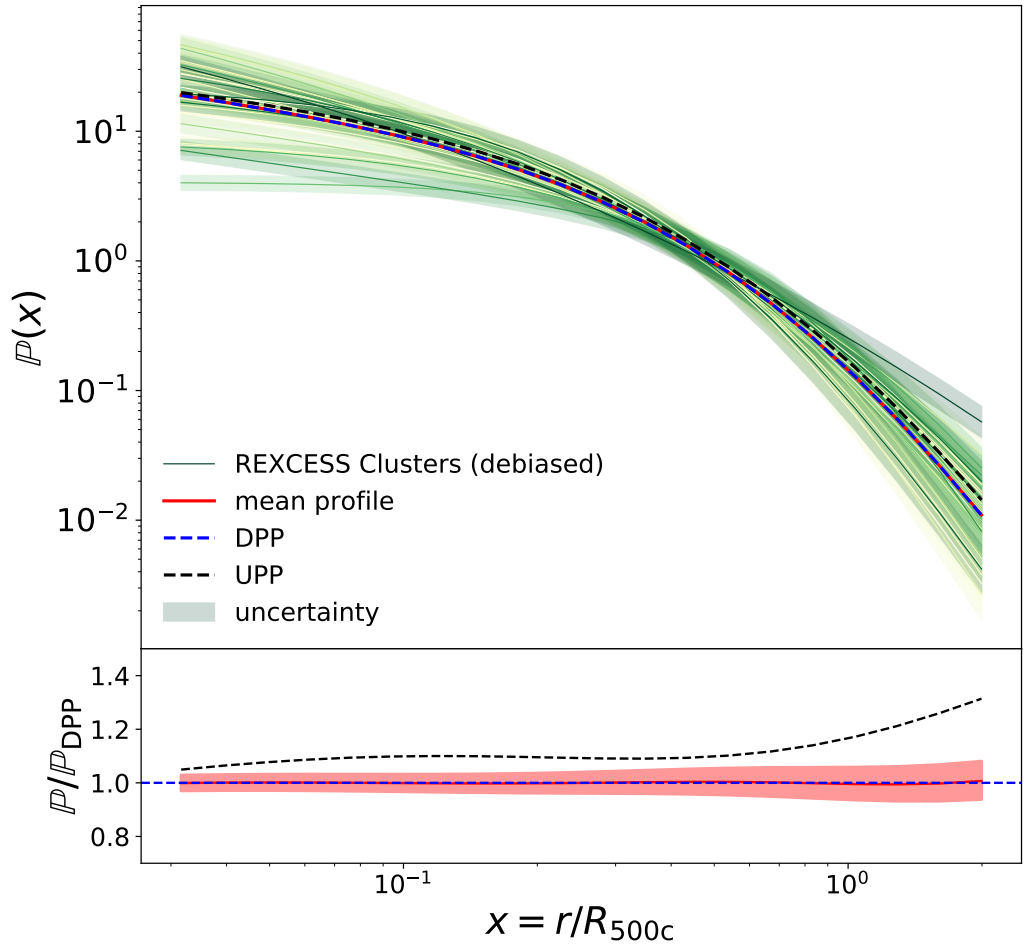

Figure 2.3: **Top**: Individual GNFW fits for the scaled pressure profiles of each cluster in REXCESS sample after R_{500c} and P_{500c} have been corrected for hydrostatic mass bias (solid green lines) with uncertainty estimated from the scatter in the mass bias (green semitransparent bands). Also shown are the mean profile (dashed blue line) of the corrected samples and the best-fitting GNFW profile to the median, $\mathbb{P}(x)$ (solid red line). The best-fitting $\mathbb{P}(x)$ of the uncorrected UPP model (dashed black line) is also plotted for comparison. **Bottom**: The ratio between $\mathbb{P}(x)$ of the UPP model (dashed black line) and the mean corrected profile of the REXCESS sample (solid red line) with respect to the corrected $\mathbb{P}(x)$ (dashed blue line) are shown. Uncertainty in the adjusted mean pressure profile (red semitransparent band) is calculated through the procedure discussed in Section 2.3.2.

2.3.2 Adjustment of the Universal Pressure Profile

The Universal Pressure Profile (UPP) is a model for ICM thermal pressure profiles developed by Arnaud et al. (2010) which was calibrated off the REXCESS sample. For each cluster in the sample, the pressure profile – derived along with the X-ray measurements of gas density and temperature profiles – is scaled with the characteristic pressure P_{500c} and cluster radius R_{500c}. As discussed in Section 2.2.2, both R_{500c} and P_{500c} are dimensional rescalings of M_{500c}, which itself is measured from a $M_{500c} - Y_X$ relation (Kravtsov et al., 2006; Nagai et al., 2007a; Arnaud et al., 2007) which was calibrated on biased hydrostatic mass estimates. Note that Arnaud et al. (2007) itself does not use the REXCESS sample, which could potentially allow selection bias to creep in. The UPP model is widely used for characterizing cluster masses in SZ surveys (e.g. Hasselfield et al., 2013; Planck Collaboration et al., 2016c; Hilton et al., 2018) and is expressed as

$$\begin{aligned} P(x, M_{500c}, z) =& P_{500c}(M_{500c}, z) \\ & \times \mathbb{P}(x) \left[\frac{M_{500c}}{3 \times 10^{14} h_{70}^{-1} M_\odot} \right]^{\alpha_P(x)}, \end{aligned} \tag{2.21}$$

with variables taking the same meaning as in Section 2.2.2. The empirical term, $(M_{500c}/3 \times 10^{14} h_{70}^{-1} M_\odot)^{\alpha_P(x)}$, reflects the deviation from standard self-similar scaling with $\alpha_P(x) = 0.22/(1 + 8x^3)$. A GNFW profile, $\mathbb{P}(x)$, is fit against the (geometric) mean profile of the scaled REXCESS sample.

The hydrostatic bias that we found for M_{500c} in the REXCESS sample is transferred to the normalization of observed pressure profiles through the resultant changes in P_{500c} and R_{500c}. For each REXCESS cluster, we use the GNFW pressure profile provided in Arnaud et al. (2010) and rescale P_0, and c_{500} according to Eq. 2.15 and 2.16 to get the debiased fits for each cluster. We then evaluate the geometric mean of the scaled profiles, P_m, and fit it with a GNFW model in the log-log plane. We also estimate the uncertainty in the mean profile by approximating the uncertainty in each corrected pressure profile via lognormal distributions with variances $\sigma_{\ln R}$ and $\sigma_{\ln P}$. Moreover, we use this uncertainty to define the 68% range for the mean profile confined by a high profile, P_h, and a low profile, P_l.

We fit new GNFW models to the mean, high and low profiles discussed above, fixing the outer slope parameter to $\beta = 5.490$ as was done in the original UPP model. In Arnaud et al. (2010), the GNFW model of the UPP is fitted to the observed average scaled profile in the radial range $[0.03–1]R_{500c}$, combined with the average simulation profile beyond R_{500c} which is crucial for determining the outer slope β. In our paper, the GNFW model is fitted to the debiased observed profiles within R_{500c}, but we lack information beyond this radius. So we choose to keep β as same as its original value in the UPP model. The best fitting parameters of the GNFW models for P_m, P_h, and P_l are reported in Table 2.2.

GNFW parameters	P_0	c_{500}	α	γ
UPP	8.403	1.177	1.051	0.3081
$P_{\rm m}$	5.048	1.217	1.192	0.433
$P_{\rm h}$	5.159	1.204	1.193	0.433
$P_{\rm l}$	4.939	1.232	1.192	0.432

Table 2.2: Parameters for GNFW fits to the mean ($P_{\rm m}$), high ($P_{\rm h}$; $+1\sigma$), and low ($P_{\rm l}$; -1σ) profiles, as well as parameters for the dimensionless pressure profile of the UPP model.

In the top panel of Figure 2.3, we plot corrected GNFW fits to the debiased pressure profiles for each of the 31 REXCESS clusters. As discussed in Section 2.3.1, the scatter in $B_{\rm M}$ is significant and introduces non-negligible uncertainty to the debiased pressure profiles of the REXCESS sample. We also show the uncertainty in the debiased pressure profile for each RECXESS cluster considering the uncertainty as determined by $\sigma_{\ln B_{\rm R}}$ and $\sigma_{\ln B_{\rm P}}$. We show the geometric mean of these scaled profiles, the fit to this curve, and the UPP model for comparison. The dispersion in these scaled pressure profiles is significant in the core both before and after debiasing regions due to the various dynamical states, including both the cool core and morphologically disturbed clusters of the REXCESS sample (Arnaud et al., 2010). The mean of the debiased scaled pressure profiles and its GNFW fit, $\mathbb{P}(x)$, is lower than in the original UPP model. In the bottom panel of Figure 2.3, we plot the fractional difference between both the UPP and the debiased mean scaled profile against our best fit to the mean scaled profile. We also show uncertainty in the pressure model with the red semitransparent region.

The UPP is $\approx 5\%$ higher than the mean of the debiased pressure profile in the center of the cluster and gradually climbs to 20% at $R_{500\rm c}$, and reaches almost $\approx$ 35% at the outermost outskirts. Only weak scattering is found for the adjusted scaled pressure profile compared to the uncertainty of scaled pressure profile of each REXCESS cluster, which is due to the assumption of using Gaussian approximating the uncertainty of individual profile in logarithmic scale at fixed radii, and uncertainty of the mean decreases with the growth of the sample size of the REXCESS clusters.

2.3.3 Self-similarity of the Pressure Profile

We also explore whether the REXCESS pressure profiles deviate from self-similarity by studying their radial variation as a function of mass. To do this, we look for mass trends in $P(x)/P_{500\rm c}$ in our debiased profiles. We evaluate these profiles at $x = r/R_{500\rm c} = 0.1,\ 0.2,\ 0.4,\ 0.8$. This range of radii avoids either too small or too large values of x. We avoid larger scaled radii because X-ray measurements pressure

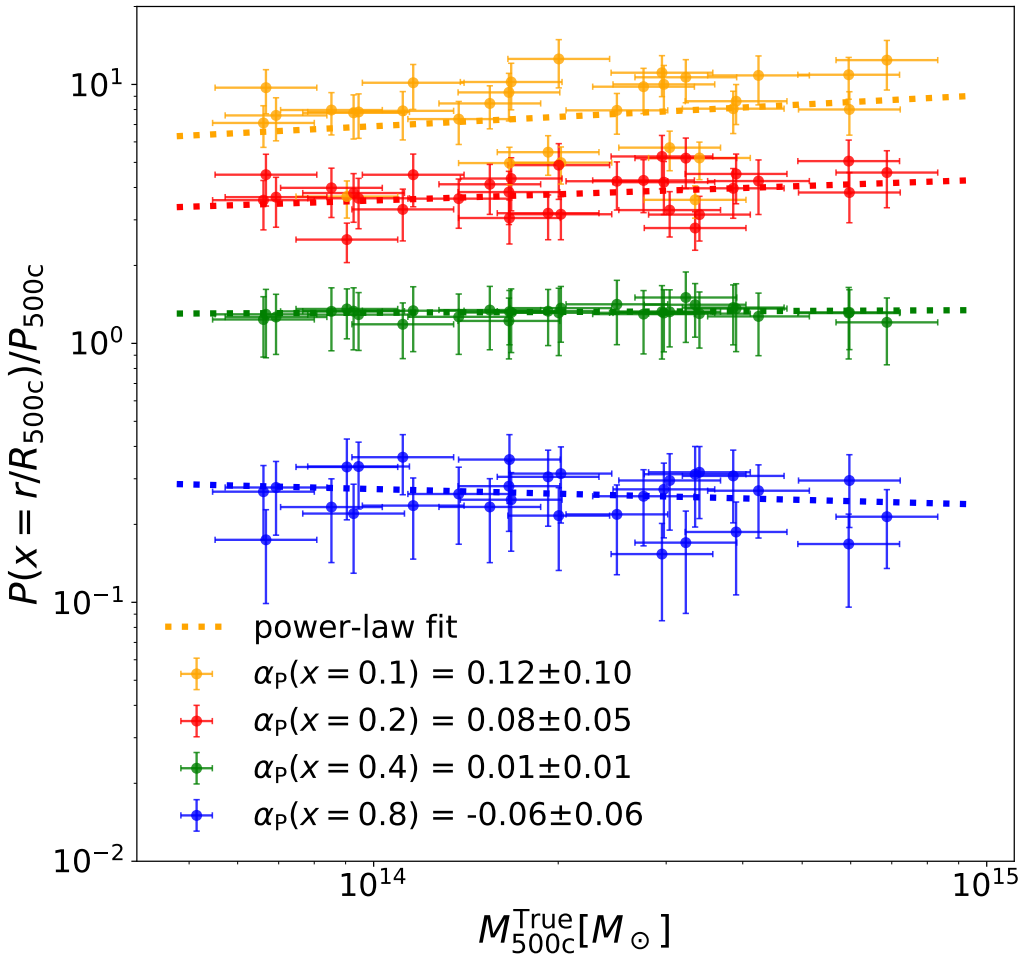

Figure 2.4: Deviations from self-similarity as a function of mass and radius. Debiased pressure is plotted against corrected M_{500c} at different scaled radii $x = r/R_{500c}$: 0.1 (red), 0.2 (orange), 0.4 (green) and 0.8 (blue). The pressure implied by the best-fitting GNFW pressure profiles at these radii for the 31 clusters in the REXCESS sample are shown as points. We fit power-laws for each value of x (dashed lines) to determine the mass dependence of cluster pressures. Error bars show the uncertainty introduced by the scatter in B_M while correcting cluster masses and recalibrating the GNFW fit of each RECXESS cluster. After debiasing the pressure profiles, we find no evidence for deviations from self-similarity.

$\alpha_{\rm P}(x)$	x=0.1	x=0.2	x=0.4	x=0.8
UPP	0.22	0.21	0.15	0.06
DPP	0.12 $\pm$0.10	0.08 $\pm$0.05	0.01 $\pm$0.01	-0.06 $\pm$0.06

Table 2.3: Comparison of the best-fitting $\alpha_{\rm P}(x)$ in the UPP and DPP models. Note that under the DPP model, $\alpha_{\rm P}(x)$ is consistent with zero at all radii.

profiles in REXCESS clusters rarely get beyond R_{500c} (Arnaud et al., 2010).[1] We avoid taking a smaller value of x because the REXCESS sample contains systems with various dynamical states which can alter the state of gas in the center of the cluster. Following Arnaud et al. (2010), we fit a power-law of the form $P/P_{500\rm c} \propto M_{500\rm c}^{\alpha_{\rm P}(x)}$ to each set of points weighted by uncertainties on both cluster masses and pressure following the orthogonal regression approach, proposed for the analysis when both the dependent and the independent variables are random. Best fitting results are represented in Table 2.3.

In Figure 2.4, we show the results of this fit, with different colors representing different scaled radii and error bars representing uncertainty due to the intrinsic scatter in $B_{\rm M}$. We show the best-fit power-laws to each set of points and the values of their power indices.

Our study of the debiased scaled pressure profiles of the REXCESS cluster sample finds that $\alpha_{\rm P}(x)$ at all radii are consistent with zero, which means a less significant deviation from standard self-similarity compare to the UPP model. We can observe a radial dependence of $\alpha_{\rm P}(x)$ similar to that found in the UPP model. However, this term in UPP is treated as a second-order deviation term in addition to a constant modification of the standard self-similarity, $\alpha_{\rm P} \sim 0.12$, which can be neglected in first-order approximation. Based on the discussion above, we see no evidence for deviations from self-similarity, which would require the mass-dependent term in Eq. 2.21. We modify the UPP by eliminating the deviation term and get a simplified model for ICM pressure profiles, Debiased Pressure Profile (DPP) :

$$P_{\rm DPP}(x, M_{500\rm c}, z) = P_{500\rm c}(M_{500\rm c}, z) \times \mathbb{P}(x). \tag{2.22}$$

Here, parameters take on the same meaning as in $P_{\rm m}$ in Table 2.2.

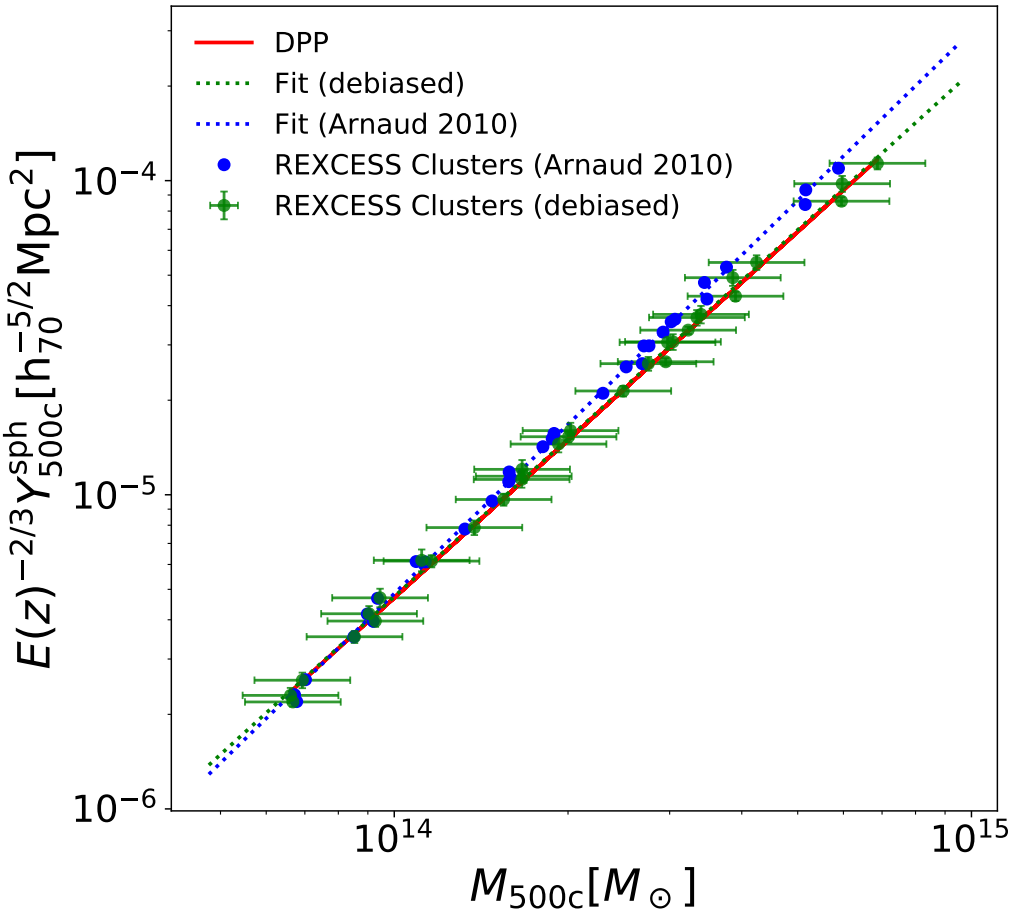

Figure 2.5: The spherical volume-integrated Compton parameter, $Y_{\rm sph}$, vs. mass, M_{500c}, for the REXCESS sample after correcting for hydrostatic bias (green dots) and the corresponding best-fit power-law relation (dashed green line). The analytical $Y_{\rm sph}(R_{500c}) - M_{500c}$ relation derived from the DPP model (solid red line) is also shown. The biased $Y_{\rm sph}(R_{500c})$ and M_{500c} (blue dots) and the corresponding best-fit power-law relation (dashed blue line) from Arnaud et al. (2010) are plotted for comparison.

2.3.4 $Y - M$ Relation

The spherical volume-integrated Compton parameter, $Y_{\rm sph}$, of a cluster is the integral of the gas's thermal pressure profile over a spherical region and is defined as:

$$Y_{\rm sph}(R) = \frac{\sigma_{\rm T}}{m_{\rm e}c^2} \int_0^R 4\pi P_{\rm e}(r) r^2 {\rm d}r, \tag{2.23}$$

where $\sigma_{\rm T}$ is the Thomson cross-section, $m_{\rm e}$ is the electron mass, and $P_{\rm e}$ is the thermal electron pressure. Since the pressure is directly related to the depth of cluster gravitation potential, the integrated Compton parameter, $Y_{\rm sph}$, is closely related to the mass of the cluster. Studies (e.g. Da Silva et al., 2004; Nagai, 2006) find a low intrinsic scatter in the relation between integrated Compton parameter and cluster mass, indicating that the Compton parameter $Y_{\rm sph}$ serves as a good proxy for cluster mass. The $Y_{\rm sph} - M$ relation was previously modeled with a power-law (Kravtsov et al., 2006; Nagai et al., 2007a; Arnaud et al., 2007). Accordingly, we parameterize the $Y_{\rm sph}(R_{\rm 500c}) - M_{\rm 500c}$ relation as

$$h(z)^{-2/3} Y_{\rm sph}(R_{\rm 500c}) = 10^A \left[\frac{M_{\rm 500c}}{3\times10^{14} M_\odot}\right]^\alpha h_{70}^{-5/2} {\rm Mpc}^2. \tag{2.24}$$

We fit Eq. 2.24 to the X-ray-measured Compton parameter and the biased X-ray hydrostatic masses of the REXCESS sample and find that $\alpha = 1.790 \pm 0.015$, and $A = -4.739 \pm 0.003$. The $Y_{\rm sph} - M$ relation can be derived from the UPP model by combining Eq. 2.21 for the UPP and Eq. 2.23 and gives $\alpha = 1.787$, and $A = -4.745$. The analytical calculations based on UPP and direct fits to observation data are in excellent agreement: both claimed a deviation from the slope predicted by self-similarity, $\alpha_{\rm s} = 5/3$, of approximately $\Delta\alpha = \alpha - \alpha_{\rm s} \approx 0.12$. Notice this deviation $\Delta\alpha$ corresponds to the $\alpha_P(x)$ for the pressure model, which is characterized by a function of cluster mass and radius, however, Arnaud et al. (2010) showed this term can be approximated by a constant in the calculation of the spherical Compton signal and only causes a difference of $\leq 1\%$ for clusters in the mass range $[10^{14} M_\odot, 10^{15} M_\odot]$.

However, the hydrostatic masses used for constructing the UPP model are systematically underestimated, which means that the cluster radii are also biased. Integrating an X-ray-measured pressure profile over a biased volume leads to a biased Compton signal. We apply the rescaling methods discussed in Section 2.2.2 to the GNFW fits to scaled pressure profiles and correct the X-ray measured radii of every REXCESS cluster, and correct the bias in the Compton parameter derived from X-ray measurements. We also calculate $Y_{\rm sph}$ analytically by integrating our DPP over

[1] Also note that the $R_{\rm 500c}$ values in (Arnaud et al., 2010) are biased low by $R_{\rm 500c}^{\rm X-ray}/R_{\rm 500c}^{\rm True} \sim 0.95$, meaning that the profiles extend to smaller radii than reported in the original paper.

the cluster within the radius $r = xR_{500c}$

$$Y_{\rm sph}(xR_{500c}) = \frac{4\pi\sigma_{\rm T}}{3m_{\rm e}c^2}R^3_{500c}P_{500c} \times \int_0^x 3(x')^2\mathbb{P}(x')\left[\frac{M_{500c}}{3\times10^{14}h_{70}^{-1}M_\odot}\right]^{\alpha_{\rm P}(x)}{\rm d}x', \tag{2.25}$$

then we simplify the integral, getting

$$h(z)^{-2/3}Y_{\rm sph}(xR_{500c}) = C(x)\left[\frac{M_{500c}}{3\times10^{14}h_{70}^{-1}M_\odot}\right]^{\alpha}, \tag{2.26}$$

where $\alpha = 5/3$ given by $P_{500c}R^3_{500c}$, since $\alpha_{{\rm P}(x)}$ is set to be 0 in DPP and has no contribution to α, and

$$C(x) = 2.925\times10^{-5}I(x)h_{70}^{-1}{\rm Mpc}^2, \quad I(x) = \int_0^x 3\mathbb{P}(x')(x')^2{\rm d}x'. \tag{2.27}$$

We use the value for the parameters $P_0, c_{500}, \alpha, \beta, \gamma$ of $P_{\rm m}$ reported in Table 2.2 to get $I(1) = 0.554$. Rewriting $C(1)$ to the logarithmic form 10^A, we get $A = -4.790$, along with $\alpha = 5/3$, as previously discussed for $Y_{\rm sph} - M$ relation, which agrees well with the direct fit to the REXCESS sample after correcting for hydrostatic bias: $\alpha = 1.673 \pm 0.014$ and $A = -4.786 \pm 0.004$.

In Figure 2.5, we plot fits for the integrated Compton signal versus cluster mass after correction for hydrostatic bias and analytical calculated $Y-M$ relation based on DPP. For comparison, we also plot $Y - M$ relation reported in Arnaud et al. (2010).

The corrected $Y-M$ relation leads to smaller Y values at a given M compared to the UPP model, which indicates that our $Y - M$ relation predicts a higher mass for the observed cluster given the same measured Compton signal. The new fit also shows a negligible difference from analytical results based on DPP. The value of the best-fit slope is close to the self-similar scaling with a tiny deviation $\Delta\alpha = 1.673-5/3 = 0.006$.

We find no evidence for a power-law index of the $Y_{\rm sph} - M_{500c}$ relation which deviates from the predictions of self-similarity, which is consistent with a small deviation from standard self-similarity of the $Y_{\rm sph}$-mass scaling relation in Gupta et al. (2017). The disappearance of the deviation from self-similarity is mainly due to the dependence of hydrostatic bias on cluster mass. We find changes in the spherical Compton signal of clusters in the REXCESS sample after adjusting for hydrostatic bias are much less significant, $< 2\%$ compared to the correction of cluster masses, which means the shift in cluster masses is the key factor for the modification on the power-law index of the $Y-M$ relation. Notice that the relation of $M_{500c}^{\rm True}$ vs. $M_{500c}^{\rm X-ray}$ for the REXCESS sample we derived yields $B_M \propto M^{\simeq0.08}$, equal to the shift of cluster mass after correction. To a great extent, this explains the variation – around 0.12 – of the power-law index of the $Y - M$ relation after adjusting for hydrostatic bias.

The slope of the $Y - M$ relation being consistent with the standard self-similar model after adjusting for hydrostatic bias indicates that the studies that claim deviations from self-similarity in mass scaling relation like $L_{\rm X} - M$ and $Y_{\rm X} - M$ (e.g. Allen et al., 2003; Arnaud et al., 2007) may need to be revised as their results are also affected by similar X-ray mass biases. Additionally, the existence of self-similarity in the mass independence of out pressure model and the Y-M relation makes us more confident in extrapolating out the DPP model to higher redshifts in the calculation of thermal SZ power spectrum by assuming a self-similarity in the redshift dependence according to the standard self-similar model. We also note that the REXCESS sample has a limited mass range. Further confirmation of self-similarity in the $Y - M$ relation requires joint work of simulations and further observations with extended mass range.

2.3.5 Thermal SZ Angular Power Spectrum

The tSZ power spectrum is a powerful probe of cosmology and can provide promising constraints on cosmological parameters: $C_\ell \propto \sigma_8^{7-9}$ (e.g. Komatsu & Seljak, 2002; Shaw et al., 2010; Trac et al., 2011). Since clusters are the dominant source of tSZ anisotropies, due to the number density of clusters and the gas thermal pressure profile, the tSZ power spectrum can be adequately modeled by an approach referred to as the halo formalism (e.g. Cole & Kaiser, 1988; Komatsu & Kitayama, 1999).

The tSZ angular power spectrum at a multipole moment, ℓ, for the one-halo term is given by

$$C_\ell^{\rm tSZ} = f^2(\nu) \int_z \frac{{\rm d}V}{{\rm d}z} \int_M \frac{{\rm d}n(M,z)}{{\rm d}M} |\tilde{y}_\ell(M,z)|^2 {\rm d}M {\rm d}z, \tag{2.28}$$

where $f(\nu) = x\coth(x/2) - 4$ is the spectral dependence with $x = h\nu/(k_{\rm B}T_{\rm CMB})$. Integration over redshift and mass are carried out from $z = 0.0$ to $z = 6.0$ and from $M = 10^{10} M_\odot$ to $M = 10^{16} M_\odot$ respectively. For the differential halo mass function ${\rm d}n(M,z)/{\rm d}M$, we adopt the fitting function from Tinker et al. (2008) based on N-body simulations.

Following Komatsu & Seljak (2002), the 2D Fourier transform of the projected Compton y-parameter, $\tilde{y}_\ell(M,z)$ is given by

$$\tilde{y}_\ell(M,z) = \frac{4\pi r_{\rm s}}{\ell_{\rm s}^2} \frac{\sigma_{\rm T}}{m_{\rm e}c^2} \int x^2 P_{\rm e}(x) \frac{\sin(\ell x/\ell_{\rm s})}{\ell x/\ell_{\rm s}} {\rm d}x, \tag{2.29}$$

with the limber approximation (Limber, 1953), which is used to relate the angular correlation function to the corresponding three-dimensional spatial clustering in an approximate way and to avoid spherical Bessel function calculations, where $x = r/r_{\rm s}$ is a scaled dimensionless radius, $r_{\rm s}$ is characteristic radius for a NFW profile defined by $R_{\rm 500c}/c_{\rm 500c}$, and we use average halo concentrations, $c_{\rm 500c}$, calibrated as a function of cluster mass and redshift from Diemer & Kravtsov (2015). The corresponding angular wave number $\ell_{\rm s} = d_{\rm A}/r_{\rm s}$, where $d_{\rm A}(z)$ is the proper angular-diameter distance

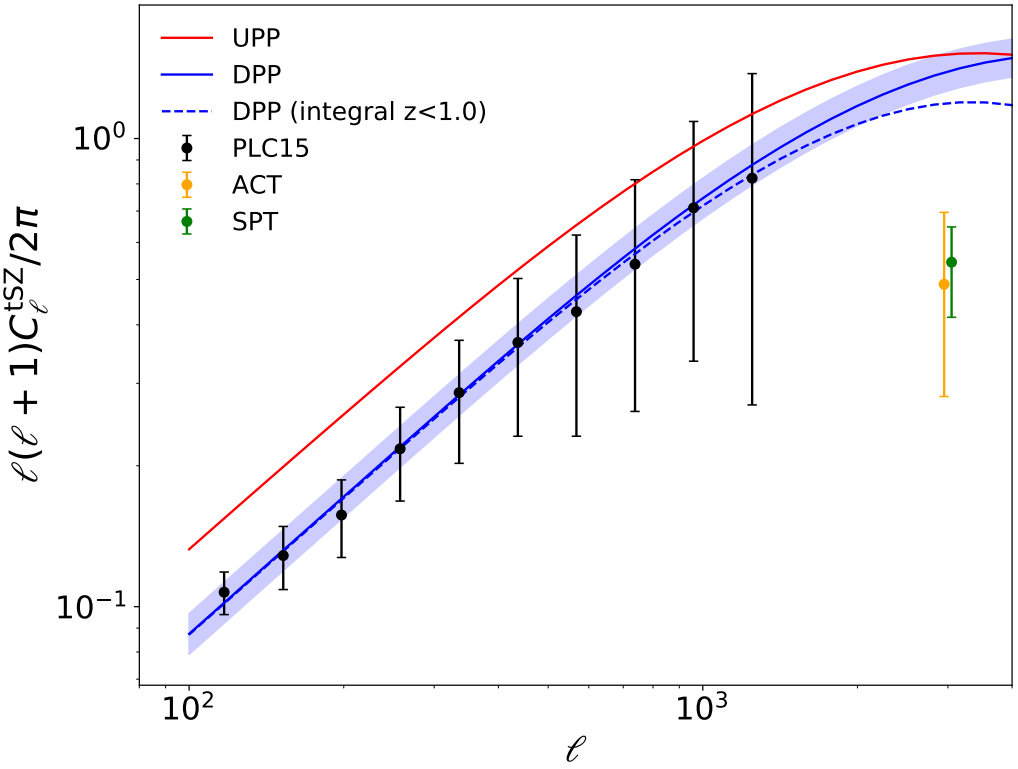

Figure 2.6: Predictions for the one-halo term of the tSZ power spectrum calculated with the UPP model (red line) and the DPP model (blue line). The tSZ power spectrum calculated with Equation 3.49 integrated from $z = 0.0$ to $z = 1.0$ based on the DPP model is plotted for comparison (dashed blue line). Planck 2015 analysis of the tSZ power spectrum(black dots) with error bars due to uncertainties of foreground contamination and statistical errors. ACT (orange dot with error bar), and SPT (green dot with error bar) values correspond to $\ell = 3000$ are also shown, but they have been shifted in the plot for clarity. All tSZ data are rescaled to 146GHz for direct comparison, the uncertainty of the tSZ power spectrum (blue semitransparent band) is due to the uncertainty in the pressure profile used for the integral.

at redshift z. $P_{\rm e}(x)$ is the electron pressure we've discussed about Section 2.2.1. The integral is carried out within a spherical region with radius $R \sim 4R_{500c}$.

In Figure 2.6, we compare the measured tSZ power spectrum to the one-halo term predicted by the UPP and DPP models. Our predictions for the tSZ spectrum are made by assuming the fiducial parameters $\Omega_m = 0.3,\ \Omega_\Lambda = 0.7,\ \Omega_b = 0.045,\ h = 0.7,\ n_s = 0.96,\ \sigma_8 = 0.8$. We use measurements of the tSZ power spectrum from the analysis of ACT (Dunkley et al., 2013), SPT (George et al., 2015), and Planck (Planck Collaboration et al., 2016a), all rescaled to 146 GHz, at which $f^2(\nu) = 1$, for direct comparison. The uncertainties in the Planck 2015 data points account for statistical and systematic errors, as well as modeling uncertainties associated with correcting for foreground contamination.

The tSZ power spectrum derived from the original UPP model predicts much higher values than observational data while our DPP model leads to the tSZ power spectrum matches the tSZ data of Planck within $1-\sigma$ uncertainty for multipoles $100 \leq \ell \leq 1300$. However, the tSZ power spectrum calculated with our DPP model still shows a significant tension with ACT and SPT data at $\ell = 3000$. Our work shows adjusting ICM pressure profiles for hydrostatic bias due to non-thermal pressure has a significant effect on lowering the amplitude of the power spectrum by 30-40%. This is in agreement with other work studying the change in the shape of the tSZ power spectrum after including the effect of non-thermal pressure (e.g. Shaw et al., 2010; Battaglia et al., 2010; Trac et al., 2011; Battaglia et al., 2012).

In the analytical calculation of the tSZ power spectrum, we extrapolate our pressure model to redshifts as high as $z = 6.0$, even though our pressure model is built on simulation data from a low redshift snapshot ($z = 0.1$). However, we show in Figure 2.6 that galaxy clusters of redshift $z \geq 1.0$ will not significantly affect our calculation of the tSZ power spectrum at $\ell \leq 1300$. The tSZ power spectrum at $\ell \geq 3000$ shows it is more sensitive to the high redshift clusters, which may indicate that redshift dependence could potentially lower the tension between our calculation of the tSZ power spectrum and high-multipole observations.

2.4 Discussion and Conclusions

In this chapter, we presented a simulation-based model to characterize the relation between the "true" masses and the X-ray-estimated hydrostatic masses of galaxy clusters. We use X-ray masses measured from synthetic images of simulated clusters drawn from the IllustrisTNG, the BAHAMAS, and the MACSIS simulations (Barnes et al., 2020) to fit a power-law relation for $M_{\rm 500c}^{\rm True}$ v.s. $M_{\rm 500c}^{\rm X-ray}$. We then use this model to correct the X-ray measured hydrostatic masses for the 31 clusters in the REXCESS sample:

1. We find that X-ray-measured hydrostatic masses underestimate masses of the clusters in the REXCESS sample by around 7% on average and that the bias

increases with mass from $\approx 0\%$ at $M_{500c}^{\mathrm{X-ray}} = 10^{14} M_{\odot}$ to $\approx 15\%$ at $M_{500c}^{\mathrm{X-ray}} = 10^{15} M_{\odot}$, showing the same significant mass dependence as the simulation results.

2. The significant scatter in simulation results has been incorporated into our model. This scatter also induces non-negligible uncertainties in the corrected of masses of individual REXCESS clusters, around $\pm 20\%$.

In this work, we assume mass bias does not or only weakly depends on the redshift. The REXCESS sample spans a redshift range of $0 < z < 0.2$ and our correction is based only on $z = 0.1$ snapshots. To study the dependence of mass bias on redshift, one could look into more snapshots of the simulations we used. As we mention in Section 2.3.2, the dynamical states of different of RECXESS clusters could vary significantly, which could also be considered a selection criterion in addition to the cluster mass. Furthering modeling may be improved by accounting for dynamical state when correcting X-ray-measured hydrostatic masses.

We discussed how the mass bias we found transfers to other X-ray observables. Scaling relations between cluster mass, radius, and characteristic pressure ($R \propto M^{1/3}$, $P \propto M^{2/3}$), enable a convenient correction of GNFW fits to scaled pressure profiles, through the modification of the P_0 and c_{500} parameters.

We adjusted the universal galaxy cluster pressure profile for hydrostatic mass bias through recalibrating the scaled pressure profiles of each cluster in the REXCESS samples used to construct the UPP model:

1. In our updated pressure model, DPP, pressures are 5% lower than the UPP model in the inner region of the clusters, and 15% lower at R_{500c}.

2. We achieve a good agreement on a small value of α_{P} in the respective study of pressure model and $Y_{\mathrm{sph}} - M$ relation, which implies standard self-similarity still stands for the scaling relation of the adjusted universal pressure model and the $Y_{\mathrm{sph}} - M$ relation.

3. An analytical calculation of the thermal SZ angular power spectrum derived from DPP is consistent with the analysis of Planck thermal SZ survey data without requiring extreme cosmological parameters.

Many avenues remain for future work on this topic. Our analysis is restricted to late times, meaning that we do not explore the redshift dependence of hydrostatic mass bias. Analysis that incorporates redshift evolution would likely lead to more accurate cosmological constraints from the tSZ power spectrum. Similar to the UPP, our DPP does not differentiate between relaxed and unrelaxed clusters or cool core and non-cool-core clusters. The impact of hydrostatic mass bias on these clusters sub-categories has not yet been determined. Lastly, we note that even our corrected fit cannot simultaneously match the $\ell = 3000$ tSZ power spectrum measurements from ACT and SPT. This discrepancy remains an open question.

Chapter 3

A Hydro-Particle-Mesh Code for Efficient and Rapid Simulations of the Intracluster Medium

3.1 Introduction

Cosmological simulations have greatly improved our understanding of the formation and evolution of the cosmic structures throughout our universe and are widely used to interpret observations and design new instruments and surveys. N-body simulations of gravitational dynamics make detailed and reliable predictions for the distributions of dark matter, which forms the backbone of structure formation, and dark energy responsible for the accelerated expansion of the universe (e.g. Springel et al., 2005; Boylan-Kolchin et al., 2009; Klypin et al., 2011; Angulo et al., 2012; Skillman et al., 2014; Klypin et al., 2016; Ishiyama et al., 2021). Hydrodynamic simulations, which model the coupled evolution of dark matter and cosmic gas (e.g. Iannuzzi & Dolag, 2012; Vogelsberger et al., 2014; Khandai et al., 2015; Schaye et al., 2015; Feng et al., 2016b; Dolag et al., 2016; Dubois et al., 2016; Kaviraj et al., 2017; McCarthy et al., 2017b; Barnes et al., 2017; Tremmel et al., 2017; Pillepich et al., 2018b; Davé et al., 2019), are also able to predict many directly observable properties of cosmic gas and galaxies.

Understanding the large scale structure of our universe requires two parts: (i) an accurate solution to the equations of motion for the dark matter and (ii) physically reasonable approximations for the behavior of baryonic components of the universe. Together, these two components build the foundation of the modern observational cosmology. Dark matter N-body simulations have achieved significant progress in developing the understanding of the structure of dark matter halos (e.g. Navarro et al., 1996, 1997, 2004) and their clustering (e.g. Springel et al., 2006; Tinker et al., 2008; Watson et al., 2013; Bocquet et al., 2016). They were instrumental in establishing the ΛCDM cosmological model as the dominant paradigm for the nature of both dark

matter and dark energy, but suffer from the fundamental limitation of being incapable of providing any direct prediction for the baryonic component. Thus, the hydrodynamic simulations that also simulate the baryons that form the visible components in our universe are crucial for interpretation and calibration of the results of observational data. A detailed review of the modern hydrodynamic simulations studying the properties, growth and evolution of galaxies is given in Vogelsberger et al. (2020).

Hydrodynamic simulations are generally preferred for solving the non-linear physics of structure formation and predicting the survey observable dependence on cosmological parameters. However, the effective volumes of modern surveys keep growing, and achieving the science goals of these surveys requires numerical simulations of exceptionally large volumes - both for correctly capturing the statistics of the rare objects and for computing the covariance matrices between the observables. Simulations in spatial volumes comparable to the surveys in size are generally too expensive to make many large-scale mock observations and explore both astrophysical and cosmological parameter space. In the face of increasing demand for multiple realizations of simulated mock catalogs for comparison with the large-scale structure observations, fast approximate approaches for dark matter simulations based on semi-numerical methods and lagrangian perturbation theory have been developed. For example, PTHALOS (Scoccimarro & Sheth, 2002) has been used for efficiently generating mock galaxy distributions, PINOCCHIO (Monaco et al., 2002) is capable of accurately predicting formation and evolution of individual dark matter halos, COLA (Tassev et al., 2013) and FastPM (Feng et al., 2016a) can be used for cheaply generating large ensembles of accurate mocks that properly account for non-linear evolution. These fast approximate methods have shown their ability to reduce computational complexity and required computational resources by orders of magnitude without sacrificing accuracy on large scales.

Though we have seen significant progress in various approaches aiming to speed up dark matter only N-body simulations, there is still a notable lack of fast approximate hydro simulation methods. Previously, Gnedin & Hui (1998) used the particle-mesh (PM) solver for dark matter dynamics and allowed for the additional gas pressure force to approximate hydrodynamics. Their hydro-particle-mesh (HPM) algorithm substantially relies on the existence of a tight temperate-density relation in the intergalactic medium (IGM) and has been successfully used to model the high-redshift Lyman alpha forest with moderate precision (McDonald et al., 2002). However, the tight correlation between the gas density and temperature in the low density IGM breaks down in denser regions. Yet, it is possible to extend the range of validity of HPM-like techniques further. For example, in order to model the intracluster medium (ICM) of galaxy clusters we can adopt empirical or simulated ICM pressure profiles (e.g. Arnaud et al., 2010; Battaglia et al., 2012; He et al., 2021a) and build a mapping relation between the gas temperature or pressure and some properties of cosmic gas that can be captured by, say, a simple PM solver. Such an approach will allow to implement a fast approximate method for modeling hydrodynamics in the high-density

ICM; the gas physics can then be modeled very efficiently in both the IGM and the ICM regime, which together fill most of the spatial volume in a fast hydro simulation.

This chapter introduces an innovative hydro-particle-mesh code for efficient and rapid (HYPER) simulations of gas and dark matter. HPM simulations take approximately two to three times as long to run as PM simulations and are orders of magnitude faster than expensive hydrodynamic simulations. HYPER allows one to systematically vary the ICM and IGM models to study different baryonic physics and effects. We organize this chapter as follows: Section 3.2 discusses the model for radial profiles of dark matter and gas in the ICM. Section 3.3 briefly reviews the HPM algorithm in the IGM, then describes the implementation of the HPM for the ICM regime, including how to modify the PM code to calculate the designed HPM fields and infer the gas temperature and pressure from the local field information using a pre-computed mapping derived from a given ICM model. In Section 3.4 we evaluate our new fast hydro simulation performance by comparing the radial profiles, the integrated halo quantities, and the statistical quantities of the tSZ effect in our simulation to the predictions of the ICM model we use to implement the HPM algorithm. In Section 3.5 we conclude with our findings for the output of a HYPER simulation, and at the end, we also bring out some perspective of use cases and the future extensions of this work.

3.2 Models

This section introduces our approach for constructing an analytical model for the radial profiles of different components in galaxy clusters, under the assumption of hydrostatic equilibrium. It is based on thoroughly studied modeling work on dark matter distribution and gas pressure support. We also briefly introduce the analytical relation used by the HPM algorithm (Gnedin & Hui, 1998) to simulate gas thermal properties in the IGM.

3.2.1 Halo Model

As a model for the mass distribution in a dark matter halo of a galaxy cluster we adopt a universal NFW density profile (Navarro et al., 1997)

$$\rho_{\rm m}(r) \simeq \frac{\rho_{\rm s}}{\frac{r}{r_{\rm s}}(1+\frac{r}{r_{\rm s}})^2}, \tag{3.1}$$

where $r_{\rm s}$ is the scale radius and $\rho_{\rm s}$ is the scale density. These two variables can be specified by the halo concentration as

$$r_{\rm s} = R_{\rm 500c}/c_{\rm 500c} \tag{3.2}$$

and

$$\rho_{\rm s} = \frac{500\rho_{\rm crit}(z)c_{\rm 500c}^3}{3\left[\ln(1+c_{\rm 500c}) - c_{\rm 500c}/(1+c_{\rm 500c})\right]}, \tag{3.3}$$

where R_{500c} defines the radius of a spherical overdensity region with average density 500 times of the critical density $\rho_{\rm crit}(z)$. The total mass of the overdensity region can be used to define the halo mass as $M_{500c} = \frac{4\pi}{3} 500 \rho_{{\rm crit}(z)} R^3_{500c}$. The halo concentration c_{500c} has been calibrated as a function of cluster mass and redshift (e.g. Diemer & Kravtsov, 2015). Thus given the halo mass and redshift, we can specify the halo density profile of dark matter. The total mass enclosed within the radius r then has an analytical expression

$$\begin{aligned} M(r) &= \int_0^r 4\pi x^2 \rho_{\rm m}(x) dx \\ &= 4\pi \rho_{\rm s} r_{\rm s}^3 \left[\ln\left(\frac{r + r_{\rm s}}{r_{\rm s}}\right) - \frac{r}{r + r_{\rm s}} \right]. \end{aligned} \tag{3.4}$$

We use the NFW profile to approximate the total matter distribution, considering that dark matter dominates the mass contribution to the halo. The error on the total mass profile is mainly caused by the difference between the gas density profile and the NFW profile, which is generally considered to be a goof approximation to the dark matter distribution of halos. Though the deviation of the normalized gas density profile from the NFW model may not be negligible, the difference between the total matter density of halos and the NFW profile is much less significant since gas is subdominant in the total matter distribution. The difference between the total matter density profile and the NFW model decreases by a factor of the baryonic fraction $f_{\rm b} \sim 0.15$ compare to the gas density profile and should be much less than unity. Thus a lot of analytical work choose to model the total matter density profile with the NFW model, so that $\rho_{\rm m}(r) = \rho_{\rm dm}(r) + \rho_{\rm gas}(r) \simeq \rho_{\rm NFW}(r)$ (e.g. Olamaie et al., 2012; Shi & Komatsu, 2014). X-ray and lensing studies have also shown that NFW profiles can generally provide adequate descriptions of the mass distribution of cluster halos (e.g. Mandelbaum et al., 2006; Schmidt & Allen, 2007; Morandi & Limousin, 2012).

3.2.2 ICM Model

We construct an analytical model of the ICM based on the assumption of hydrostatic equilibrium and models for describing the gas pressure of galaxy clusters. The gas thermal pressure profile has been widely studied by both hydrodynamic simulations and SZ and X-ray observations. In most of these studies, the thermal pressure of gas generally follows an analytical form

$$P_{\rm th}(M, r) = P_{500c}(M, z) \mathbb{P}(r/R_{500c}) f(M) g(z), \tag{3.5}$$

where P_{500c} is the pressure scale derived from the self similar scaling relation

$$P_{500c} \quad = 1.65 \times 10^{-3} E(z)^{8/3} \times \left(\frac{M_{500c}}{3 \times 10^{14} M_\odot} \right)^{2/3}, \tag{3.6}$$

where $E(z) = H(z)/H_0$ and $\mathbb{P}(x = r/R_{500c})$ is a generalized NFW (GNFW) model (e.g. Nagai et al., 2007a),

$$\mathbb{P}(x) = \frac{P_0}{(c_{500}x)^{\gamma}[1 + (c_{500}x)^{\alpha}]^{\frac{\beta-\gamma}{\alpha}}}. \tag{3.7}$$

Parameters $P_0, c_{500}, \alpha, \beta, \gamma$ are normally fitted to the observed or simulated scaled pressure profiles.

The ICM gas pressure profile modelled with only the GNFW term assumes a simple self-similar behavior (e.g. Kaiser, 1986; Voit, 2005). However, several numerical and observational works (e.g. Arnaud et al., 2010; Gupta et al., 2017) claimed to observe a deviation from the self-similar scaling relation in the gas pressure, which we denote by the additional terms $f(M)$, $g(z)$ in Eq. 3.5. We adopt power-law forms for these terms, $f(M) = (M/M_{\star})^{\alpha_{\rm P}}$ and $g(z) = E(z)^{c_{\rm P}}$, where $M_{\star}$ is a chosen constant referred to as the characteristic cluster mass. However, the dependence on halo mass and redshift of the gas pressure model needs further study, as the studies on these deviation terms with numerical simulations and observations have not reached the final agreement.

In this work, we adopt the debiased pressure profile (DPP) from a recent study of the gas pressure model of the galaxy clusters (He et al., 2021a), which adjusted the Universal Pressure Profile (UPP) (Arnaud et al., 2010) for hydrostatic mass bias in X-ray observation. The DPP model strictly follows the GNFW model and get rid of the terms describe the deviation from $f(M)$ and $g(z)$ for the gas thermal pressure $P_{\rm th}(r)$. The GNFW parameters $P_0, c_{500}, \alpha, \beta, \gamma$ of the pressure model are [5.048,1.217,1.192,5.490,0.433].

Further studies of the cluster outskirts with the latest cosmological simulations (e.g. Shaw et al., 2010; Nelson et al., 2012; Battaglia et al., 2012; Lau et al., 2013; Nelson et al., 2014; Gupta et al., 2017) and the observations of galaxy clusters (e.g. Bautz et al., 2009; George et al., 2009; Reiprich et al., 2009; Hoshino et al., 2010; Kawaharada et al., 2010; Urban et al., 2011; Simionescu et al., 2011) showed existence of the non-thermal pressure support, which is non-negligible particularly in the outskirt of galaxy clusters. The non-thermal pressure is mainly due to the non-thermal gas processes like virialized bulk motions and turbulent gas flows, which are primarily generated by mergers and accretion during the cluster formation. Then the total pressure of gas $P_{\rm tot}(r)$ should consist of both thermal and non-thermal contributions, modeled by

$$\begin{aligned} P_{\rm tot}(r) &= P_{\rm th}(r) + P_{\rm nth}(r) \\ &= f_{\rm th}P_{\rm tot}(r) + f_{\rm nth}P_{\rm tot}(r) \end{aligned} \tag{3.8}$$

where $f_{\rm th}(r)$ and $f_{\rm nth}(r)$ are ratios of the thermal and nonthermal terms to the total pressure.

Studying the sample of 65 galaxy clusters from a high resolution hydrodynamic cosmological simulation, Nelson et al. (2014) characterized the non-thermal pressure

fraction profile $f_{\rm nth}(r)$, and found it was universal across redshift and cluster mass of the studied 65 galaxy clusters. When scaling the cluster radii with respect to the mean matter density of the universe, the thermal fraction we mentioned above can be then expressed as

$$f_{\rm th}(r) = 1 - f_{\rm nth}(r) = A\left\{1 + \exp\left[-\left(\frac{r/R_{\rm 200m}}{B}\right)^{\gamma}\right]\right\}, \tag{3.9}$$

with the best fitted parameters $A = 0.452$, $B = 0.841$, $\gamma = 1.628$.

Then based on the assumption of the cluster dynamical state being in hydrostatic equilibrium,

$$\frac{{\rm d}P_{\rm tot}(r)}{{\rm d}r} = -\rho_{\rm gas}(r)\frac{GM(r)}{r^2}, \tag{3.10}$$

we are able to predict the gas density profile from analytic models for the enclosed mass function of halo $M(r)$, the gas thermal pressure profile $P_{\rm th}(r)$ and the gas thermal fraction $f_{\rm th}(r)$ as

$$\rho_{\rm gas}(r) = -\frac{r}{GM(r)}\frac{f_{\rm th}(r)\frac{{\rm d}P_{\rm th}(r)}{{\rm d}r} - P_{\rm th}(r)\frac{{\rm d}f_{\rm th}(r)}{{\rm d}r}}{f_{\rm th}^2(r)}. \tag{3.11}$$

The gas temperature profile of the cluster is derived by the ideal gas equation of state,

$$T_{\rm gas}(r) = \frac{\mu P_{\rm th}(r)}{k_{\rm B}\rho_{\rm gas}(r)}, \tag{3.12}$$

where μ is the mean mass per gas particle and $k_{\rm B}$ is the Boltzmann constant.

We emphasize that the analytical models we choose for both the thermal and non-thermal pressure of the gas in this work are only presented as an example, not some hard-coded choice. In HYPER, the hydro part that drives the gas particles hydrodynamics can be constructed based on general models for the gas pressure. Thus we can systematically vary the pressure profiles and study different ICM models with HYPER.

3.2.3 IGM Model

In the low-density IGM regime, where the local density is less than the mean density of the universe that $\rho_{\rm m}/\bar{\rho}_{\rm m} \lesssim 10$, shock-heating is not important, and the gas physics is set by different processes than in the ICM regime in Gnedin & Hui (1998).

Hui & Gnedin (1997) proposed a semi-analytical method to predict the temperature-density relation for any given cosmology and reionization history, using the Zel'dovich approximation. They find a tight correlation (to better than 10%) between the gas density and temperature (and hence pressure as well), well described by a power-law,

$$T = T_0\Delta^{\gamma-1}, \tag{3.13}$$

where $T_0(z)$ is a function of redshift only and is of order of 10^4K, Δ is the relative gas density, $\Delta = \rho_{\rm gas}/\bar{\rho}_{\rm gas}$, and γ is between 1 and 1.62.

Both T_0 and γ are found evolving with time. Hui & Gnedin (1997) derived analytical approximations to the temperature-density relation in a scenario when the universe reionizes rapidly, which is often considered a suitable approximation for low redshift evolution of γ and T_0.

3.3 Methods

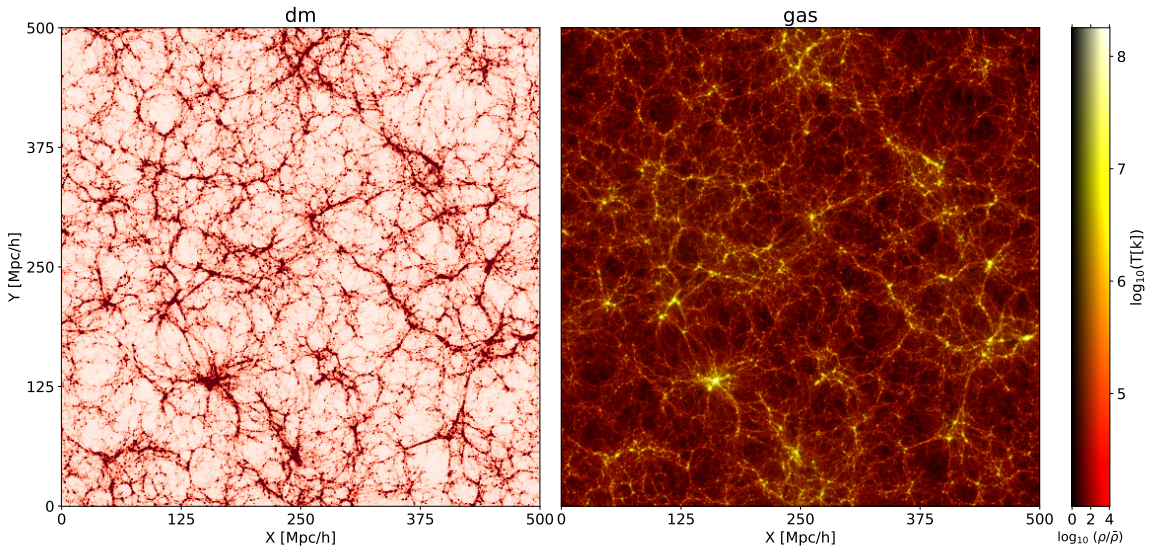

Figure 3.1: Visualization of dark matter and gas in the HYPER simulation at $z = 0.0$. The simulation box size is 500 Mpc/h per side with a thickness of 20 Mpc/h. **Left:** Shown is a projection of the dark matter density field. The cosmic large-scale structures like massive collapsed halos, elongated filaments and near-empty voids in the HYPER simulation can be easily identified in the thin slice. **Right:** The projection of gas density field is shown to have a strong correlation with the dark matter distribution. In this slice, brightness indicates the projected mass density and color hue visualizes the mean projected temperature (dull-red to brilliant-yellow indicating cold to hot, as shown by the color bar aside).

In this section we introduce our further development of the HPM algorithm, which has already shown its potential for being an efficient and accurate alternative to full hydrodynamic simulations for simulating the low column density Lyman-alpha forest (Gnedin & Hui, 1998), by expanding it from the IGM regime to the high-density ICM with the help of the analytical ICM model discussed in Section 3.2.

3.3.1 Particle-Mesh

The PM solver, which laid the foundation of the HPM algorithm, is widely used for tracking the evolution of collisionless dark matter (e.g. Hockney & Eastwood, 1981). We start with introducing a PM code developed by Trac & Pen (2004), which demonstrates how we resolve the evolution of collisionless dark matter particles in our HPM algorithm. This PM code has been adapted for solving Newton's equations of motion for dark matter particles in a Friedman-Robertson-Walker (FRW) universe. In the expanding FRW background, we use comoving coordinates $\vec{x}_{\rm c} = \vec{x}/a$, where the scale factor a is governed by the Friedman equation

$$\frac{{\rm d}a}{{\rm d}t} = aH_0(\Omega_{\rm m}a^{-3} + \Omega_\Lambda)^{1/2}, \tag{3.14}$$

assuming a spatially flat background. And to preserve the time-invariant conservation form of the Euler fluid equations, we take a new variable

$${\rm d}\tau = \frac{{\rm d}t}{a^2}, \tag{3.15}$$

for the time coordinate (e.g. Doroshkevich et al., 1980; Gnedin, 1995; Martel & Shapiro, 1998; Pen, 1998; Trac & Pen, 2004).

The time-dependence of the cosmological expansion remains only in the gravitational source term,

$$\nabla^2\Phi = 4\pi aG(\rho_{\rm m} - \bar{\rho}_{\rm m}). \tag{3.16}$$

Here the matter density is per comoving volume ${\rm d}^3\vec{x}_{\rm c} = a^{-3}{\rm d}^3\vec{x}$, and is related to the proper mass density by $\rho_{\rm m} = a^3\rho_{\rm m}^{\rm p}$. The dynamical equations of dark matter particle under the spatial and time coordinate transformations are

$$\frac{{\rm d}\vec{x}_{\rm c}}{{\rm d}\tau} = \vec{v}, \tag{3.17}$$

$$\frac{{\rm d}\vec{v}}{{\rm d}\tau} = -\vec{\nabla}\Phi, \tag{3.18}$$

where code quantities velocity $\vec{v}$ and gravitational potential Φ are related to the corresponding physical proper quantities by $\vec{v} = a\vec{v}^{\rm p}$, $\Phi = a^2\Phi^{\rm p}$.

The PM solver solves the equation of motion for the dark matter particles treating the gravitational force as a field and approximating it on a uniform mesh. We firstly use the "Cloud-in-a-Cell" (CIC) scheme (Hockney & Eastwood, 1981) to deposit mass, including both the dark matter and gas, to the mesh to create the density field, then calculate the gravitational potential Φ by solving the Poisson's equation, with the Fast Fourier Transform. In Fourier space, the modified Poisson's equation of the continuous system is expressed as

$$\tilde{\Phi}(\vec{k}) = \frac{4\pi aG\tilde{\rho}_{\rm m}(\vec{k})}{k^2}, \tag{3.19}$$

For the PM solver in our HPM algorithm, the Green function is obtained from directly transforming the finite-difference approximation of the Laplacian in the Poisson's equation,

$$\tilde{\Phi}(\vec{k}) = \frac{4\pi a G \tilde{\rho}_{\rm m}(\vec{k})(\frac{\Delta l}{2})^2}{\sin^2(\frac{\Delta l k_x}{2}) + \sin^2(\frac{\Delta l k_y}{2}) + \sin^2(\frac{\Delta l k_z}{2})}, \tag{3.20}$$

where $\Delta l = L/N$ is the length of unit grid cell, L is the length of simulation box, and N is the number of mesh cells per side. When calculating the force field, differential operators, such as the gradient ∇, are replaced by the finite difference approximations. Potential and accelerations at particle positions are obtained by interpolating on the array of mesh-defined values.

We adopt the *kick-drift-kick* (KDK) leapfrog integrator also used for GADGET-2 (Springel, 2005) in our simulation, updating the position and velocity for each particle with the time evolution operator $U(\Delta\tau) = K(\frac{\Delta\tau}{2})D(\Delta\tau)K(\frac{\Delta\tau}{2})$. The kick and drift operators, K and D, are defined as

$$K(\Delta\tau) = \begin{cases} \vec{x}_i \rightarrow \vec{x}_i \\ \vec{v}_i \rightarrow \vec{v}_i + \vec{a}_i \Delta\tau \end{cases} \tag{3.21}$$

$$D(\Delta\tau) = \begin{cases} \vec{x}_i \rightarrow \vec{x}_i + \vec{v}_i \Delta\tau \\ \vec{v}_i \rightarrow \vec{v}_i \end{cases} \tag{3.22}$$

where the acceleration $\vec{a}_i$ is interpolated for each particle from the acceleration field on the grid.

3.3.2 Hydro-Particle-Mesh

In a hydro simulation, the main difference between dark matter and gas, dynamically, is that the latter is subject to pressure forces in addition to the gravity. Our HPM method is designed by modifying the dark matter only PM algorithm to also solve the dynamical equation for gas particles,

$$\frac{{\rm d}\vec{v}_{\rm gas}}{{\rm d}\tau} = -\nabla\Phi - \frac{\nabla P}{\rho_{\rm gas}}, \tag{3.23}$$

which, in addition to the gravitational force, also includes the pressure force $-\nabla P/\rho_{\rm gas}$. The comoving gas pressure P is related to the proper pressure $P_{\rm p}$ by $P = a^5 P_{\rm p}$.

The pressure force on gas particles is inferred from HPM variables calculated and saved for each gas particle interpolated to the particle positions on HPM fields and a mapping relation derived from the gas model of ICM and IGM we have already discussed in Section 3.2.2 and 3.2.3. We will show how to select the HPM fields in Section 3.3.3 and how to construct the mapping relationship in detail in Section 3.3.4. We calculate the gravitational force $-\nabla\Phi$ following the same procedure as for the original PM code described above. The pressure force $-\nabla P/\rho_{\rm gas}$ is calculated by depositing the particle pressure to the mesh, applying the finite difference, and

finally interpolating it back to the particles in the simulation. Specific details of the implementation of the gas pressure calculation with the constructed mapping relation between the gas particle thermal properties and the HPM variables is discussed in Section 3.3.4.

Notice that we are no longer adopting a single component model to reduce computational cost as in the original HPM. As explained by Gnedin & Hui (1998), in the IGM regime the gas pressure is dynamically subdominant on large scales; hence, if one is only interested in modeling the baryonic component, one can treat the part of the gravitational force acting on baryons from the dark matter as if the dark matter followed the baryons. However, in the high-density ICM regime, pressure and gravity are comparable quantities, dark matter distribution can not be accurately approximated by the distribution of baryons, and the difference between the two components can not be neglected when solving for the evolution of baryons. Hence, this difference between the IGM and the ICM requires one to track gas and dark matter particles separately.

The results in this chapter are drawn from a HPM simulation of box whose per side length $L = 500h^{-1}$Mpc with periodic boundary conditions and equal numbers of dark matter and gas particles $N_{\rm dm} = N_{\rm gas} = 1024^3$, and the mesh size is set to be $N_{\rm mesh} = 4096^3$. The simulation runs from start point $z = 100$ to $z = 0$ while the hydro part for gas particle is turned on at $z = 6$ takes ~ 4500 CPU hours in total. In the simulation, we adopt a "concordance" ΛCDM model ($\Omega_{\rm m} = 0.3$, $\Omega_\Lambda = 0.7$, $\Omega_{\rm b} = 0.045$, $h = 0.7$ and $\sigma_8 = 0.8$).

3.3.3 HPM Variables and Fields

For the ICM model we have discussed in Section 3.2.2, if the halo mass M and the distance of the gas to the halo center r are specified, one can derive the gas thermal properties from these two variables,

$$X = X(M, r), \tag{3.24}$$

where X refers to the gas thermal quantities like temperature T or pressure P. However, in the HPM algorithm, the halo mass and the displacement of gas particles with respective to the halo center are not directly available (without adding on-the-fly halo finding), and evaluating the gas properties in the ICM region after specifying the halo it resides in will also enforce unwanted spherical symmetry. Our goal is to avoid mapping the gas temperature or pressure directly from the halo mass and the gas particle displacement in the halo. Instead of identifying the halo where gas resides and locating the gas particle with respective to the halo center, we choose to use designed HPM variables and fields that could more accurately reflect the local environment information of simulated particles. The HPM variables interpolated to the position of gas particles with the HPM fields should also show enough connection to the halo mass and radius when assuming an ideal spherical symmetry scheme,

so that we can use them to build a pre-computed mapping for inference of the gas thermal properties based on the ICM model. Since it requires two variables M and r to calculate the thermal quantities of the gas in the ICM model, the number of HPM fields used for calculating the HPM variables as alternative to halo variables M and r should also be at least 2 to break the degeneracy.

According to the description above, the HPM fields chosen should satisfy two conditions to keep our HPM algorithm efficient enough: (a) the calculation of the HPM fields in the HPM method should be efficient enough, and (b) derivation of HPM variables in the adopted ICM model should be simple, preferably with analytical expressions as a function of halo mass and radius.

In HYPER, we adopt the matter density and a new field, the scalar force, to be our HPM variables for the inference of gas thermal properties. We choose the matter density because this quantity is readily available, since it is used to solve the Poisson's equation and is saved for each particle in the simulation. For the other HPM variable, the scalar force, we create a new variable based on the idea that originates from the gravitational force calculation. Recall, that the gravitational force (per unit mass) is defined by

$$\vec{f}_{\rm g}(\vec{x}) = \int \frac{G\rho_{\rm m}(\vec{x}')(\vec{x}' - \vec{x})}{|\vec{x}' - \vec{x}|^3} {\rm d}^3\vec{x}' = G\rho_{\rm m}(\vec{x}) \otimes \frac{\vec{x}}{|\vec{x}|^3}, \tag{3.25}$$

where G is the gravitational constant, $\otimes$ denotes the operation of convolution. For the newly designed scalar force (per unit mass) variable we simply replace $\frac{\vec{x}}{|\vec{x}|^3}$ in the convolution with $\frac{1}{|\vec{x}|^2}$. The new variable shares the same units as the gravitational force, but is a scalar instead,

$$f_{\rm scalar}(\vec{x}) = G\rho_{\rm m}(\vec{x}) \otimes \frac{1}{|\vec{x}|^2}. \tag{3.26}$$

The scalar force $f_{\rm scalar}$ satisfies the requirements for the HPM variables. Thus we can quickly implement it in the PM solver, since the Fourier transform of $\frac{1}{|\vec{x}|^2}$ is

$$\int \frac{1}{|\vec{x}|^2} e^{i\vec{x}\cdot\vec{k}} {\rm d}^3\vec{x} = \frac{2\pi^2}{k} \tag{3.27}$$

and

$$\tilde{f}_{\rm scalar}(\vec{k}) = \frac{2\pi^2 G\tilde{\rho}_{\rm m}(\vec{k})}{k}, \tag{3.28}$$

which can be solved directly analogous to computation of the gravitational potential with the PM solver described in Section 3.3.2. And in the halo model, we can calculate the radial profile of the scalar force by using the NFW profile for the matter density of the halo convolved with $\frac{1}{|\vec{x}|^2}$. For the scalar force of a halo at radius $|\vec{x}| = r$, we

can can rewrite the integral in the spherical coordinates, so that

$$
\begin{aligned}
f_{\rm scalar}(r) &= \int G\rho_{\rm NFW}(\vec{x}') \times \frac{1}{|\vec{x}-\vec{x}'|^2}{\rm d}^3\vec{x}' \\
&= \int_0^\infty G\rho_{\rm NFW}(r') \int_0^\pi \frac{2\pi(r')^2{\rm d}\theta}{(r')^2+x^2-2r'x\cos\theta}{\rm d}r' \\
&= \frac{2\pi G r_{\rm s}}{x}\left[\int_0^r \frac{\rho_{\rm s}}{(1+r'/r_{\rm s})^2}\ln\left(\frac{r'+r}{r-r'}\right){\rm d}r' + \right. \\
&\quad \left. \int_r^\infty \frac{\rho_{\rm s}}{(1+r'/r_{\rm s})^2}\ln\left(\frac{r'+r}{r'-r}\right){\rm d}r'\right] \\
&= \frac{2\pi G\rho_{\rm s} r_{\rm s}\ln(r/r_{\rm s})}{1-(r/r_{\rm s})^2}.
\end{aligned}
\tag{3.29}
$$

Thus, for the given halo mass and radius we can calculate the scalar force with Eq. 3.29, which will facilitate our construction of the mapping relation between the HPM variables and the gas thermal properties in Section 3.3.4.

Other candidates for the HPM variables that have been considered are gas density or gravitational acceleration, since they are also computed by HPM code. However, if the gas density is one of the fields determining the gas temperature and pressure, then there is no way to prevent artificial numerical fragmentation when the local Jeans' length becomes too small (Truelove et al., 1997) with the fixed spatial resolution of the uniform PM grid. With using the total mass density as the HPM variable, such numerical artifacts are greatly suppressed.

For another candidate, the gravitational acceleration mentioned above is similar to the matter density since dark matter also dominates the source of gravitational force. Thus, this quantity is also very stable against numerical fragmentation. However, the gravitational acceleration is significantly affected by finite mesh resolution and is underestimated in the center regions of simulated halos. The finite resolution effect in the simulation results in a nonmonotonic profile of the gravitational acceleration. The nonmonotonicity leads to multiple solutions if the gravitational acceleration is used to predict the thermal properties of gas particles in simulated halos, while we find that the scalar force is not subject to the nonmonotonicity problem. We have also considered using the gravitational potential as one of the HPM variable, whose radial profiles of simulated halos are also monotonic. However, the gravitational potential suffers from the dynamic range being too narrow, and it has large-scale contributions that bias the local environment. After experimentation we found that using the gravitational potential is less optimal than the scalar force.

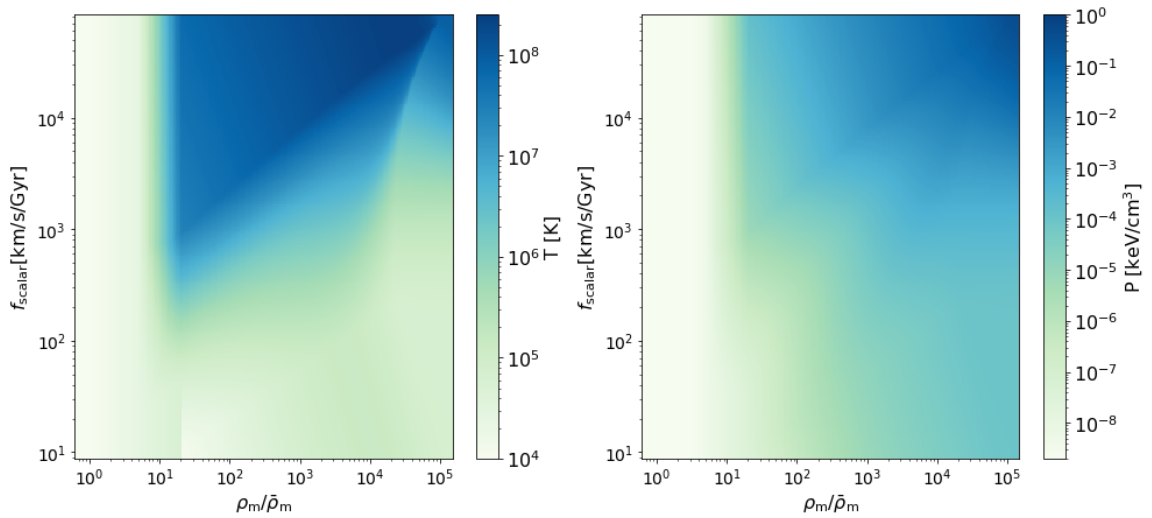

Figure 3.2: Mapping relation from the HPM variables matter density, $\rho_{\rm m}$, and the scalar force, $f_{\rm scalar}$, discussed in Section 3.3.3, to the gas temperature (left) and pressure (right). Both panels show that the HPM variables have a significant correlation with the target mapped quantities, though the mapping relation for the gas temperature has a more complicated pattern in the top right corner due to the nonmonotonicity of the temperature profile in the core region of halos in the ICM model.

3.3.4 HPM Table

With the HPM variables discussed in Section 3.3.3, matter density and scalar force, we aim to construct a mapping relation between the gas thermal properties and these designed halo variables. This mapping relation plays a crucial role in efficiently modelling the properties of gas in the HPM method for both the IGM and the ICM, and is referred to as the HPM table.

Construction of the HPM table in the low-density IGM regions where $\rho_{\rm m}/\bar{\rho}_{\rm m} \lesssim 10$ and in the high-density ICM region where $\rho_{\rm m}/\bar{\rho}_{\rm m} \gg 10$ in the simulation follows very different rules due to the dissimilar behavior of the gas in these two regimes. In the low-density IGM regime, the gas thermal properties can be very easily characterized through a power-law temperature-density relation mentioned in Section 3.2.3 with just one of the HPM variables, the matter density $\rho_{\rm m}$. In the high density regime, the tight correlation between the gas density and the gas pressure breaks down, and we are no longer able to describe the density-temperature relation by a power-law. However, with the help of the ICM model which introduces a mapping relation between the gas thermal properties and halo information, M and r, we can construct a bridge between the HPM variables and the halo information and a mapping relation from the halo variables to the gas thermal properties.

We construct a probabilistic relation between the gas thermal properties, like temperature or pressure, and the designed HPM variables using a Bayesian analysis.

Given the HPM variables for a gas particle $\rho_{\rm m}$ and $f_{\rm scalar}$, its average temperature or pressure can be estimated using a Monte Carlo approach:

$$\begin{aligned} < X|\rho_{\rm m}, f_{\rm scalar} > &= \int X(M,r)p(M,r|\rho_{\rm m}, f_{\rm scalar}){\rm d}M{\rm d}r \\ &= \frac{\int X(M,r)p(\rho_{\rm m}, f_{\rm scalar}|M,r)p(M,r){\rm d}M{\rm d}r}{\int p(\rho_{\rm m}, f_{\rm scalar}|M,r)p(M,r){\rm d}M{\rm d}r} \\ &\simeq \frac{\sum\limits_{M,r\sim p(M,r)} X(M,r)p(\rho_{\rm m}, f_{\rm scalar}|M,r)}{\sum\limits_{M,r\sim p(M,r)} p(\rho_{\rm m}, f_{\rm scalar}|M,r)}, \end{aligned} \tag{3.30}$$

and $X(M,r)$ is the gas pressure or temperature defined by the ICM model discussed in Section 3.2.2.

In the continuous limit this mapping is deterministic, since $p(\rho, f|M,r)$ should be modelled as

$$p(\rho, f|M,r) = \delta(\rho - \rho_{\rm m}(M,r))\delta(f - f_{\rm scalar}(M,r)), \tag{3.31}$$

where $\rho_{\rm m}(M,r)$ and $f_{\rm scalar}(M,r)$ are obtained from the ICM model with Eq. 3.1 and Eq. 3.29. In HYPER, we consider a discretized sampling method for our temperature estimation scheme, where we use a top-hat function to approximate $p(\rho_{\rm m}, f_{\rm scalar}|M,r)$

$$\begin{aligned} &p(\rho_{\rm m}, f_{\rm scalar}|M,r) = \Pi\left(\frac{x}{H}\right), \\ &x = \sqrt{\left(\log\frac{\rho_{\rm m}}{\rho_{\rm m}(M,r)}\right)^2 + \left(\log\frac{f_{\rm scalar}}{f_{\rm scalar}(M,r)}\right)^2} \end{aligned} \tag{3.32}$$

where H defines the width of the top-hat function. We note that in the limit of a vanishing width of the top hat, we recover the aforementioned deterministic relation.

For the prior distribution for M, r, we decompose the distribution as

$$p(M,r) = p(M)p(r|M)\ , \tag{3.33}$$

where the prior for mass $p(M)$ and the conditional $p(r|M)$ are given as

$$\begin{aligned} p(M) &\propto M\frac{dn}{dM} \\ p(r|M) &\propto \frac{r^2\rho_{\rm NFW}(M,r)}{M}\,. \end{aligned} \tag{3.34}$$

Here $\frac{dn}{dM}$ is the halo mass function and $\rho_{\rm NFW}(M,r)$ is the halo density function defined by the NFW model. Since we cannot directly sample from $p(M,r)$ without an on-the-fly halo finder, we apply the importance sampling, which is a general technique in statistics for estimating properties of a particular distribution while only having samples generated from a different distribution than the distribution of interest, for

estimation of temperature or pressure, where M, r are sampled from a uniform distribution on a logarithmic scale. We denote this covering distribution as $p_S(M, r)$. We can then re-weight the sampled points as

$$< X|\rho_{\rm m}, f_{\rm scalar} > \simeq \frac{\sum\limits_{M,r\sim p_S(M,r)} X(M,r)p(\rho_{\rm m}, f_{\rm scalar}|M,r)\frac{p(M,r)}{p_S(M,r)}}{\sum\limits_{M,r\sim p_S(M,r)} p(\rho_{\rm m}, f_{\rm scalar}|M,r)\frac{p(M,r)}{p_S(M,r)}}. \tag{3.35}$$

According to the analysis above, the procedure for building the HPM table consists of two steps:

1. Building a two dimensional halo table, by imposing a grid whose columns and rows represent designed halo masses M_i and radii r_j, where M_i and r_j are uniformly spaced within the mass and radius ranges on a logarithmic scale. This step simulates the process of sampling M, r from a uniform distribution on a logarithmic scale. For each element in the ICM table, we can calculate the HPM variables, matter density ρ_m and scalar force $f_{\rm scalar}$. Then we specify $\hat{\rho}_{\rm m}^{(i,j)} = \rho_{\rm m}(M_i, r_j)$, $\hat{f}_{\rm scalar}^{(i,j)} = f_{\rm scalar}(M_i, r_j)$.

2. Building the HPM table via HPM variables, a two dimensional table whose columns and rows represent the designed HPM variables $\rho_{\rm m}^{(k)}$ and $f_{\rm scalar}^{(l)}$, by traversing through the halo table we've built and looking into the designed distance between $(\rho_{\rm m}^{(k)}, f_{\rm scalar}^{(l)})$ and $(\hat{\rho}_{\rm m}^{(i,j)}, \hat{f}_{\rm scalar}^{(i,j)})$ defined in Eq. 3.32, we could relate the sampled points (M_i, r_j) that would contribute to the estimator of the thermal quantities defined by Eq. 3.35 corresponds to the mesh grid point $(\rho_{\rm m}^{(k)}, f_{\rm scalar}^{(l)})$ in the HPM table.

As mentioned above, we infer temperature and other thermal properties of the gas particles in simulation from a mapping relation between HPM variables and the thermal properties of gas particles we are interested in by

$$X = X(\rho_{\rm m}, f_{\rm scalar}). \tag{3.36}$$

For the intermediate region between the IGM and the ICM model we adopt a log-linear interpolation along the density axis of the HPM table.

In Figure 3.2 we plot the HPM tables, which show the mapping relation between the HPM variables, the matter density $\rho_{\rm m}$ and the scalar force $f_{\rm scalar}$, and the gas temperature and pressure. In both panels of the plot, we see a vertical band along the axis of the scalar force at $\rho_{\rm m}/\bar{\rho}_{\rm m} \sim 10$ that separates the HPM table into the IGM and the ICM parts. We find the HPM table for the gas pressure generally follows a trend of larger pressure for particles with higher density and larger scalar force. However, the mapping relation for the gas temperature has a more complicated pattern in the top right region of the HPM table, where particles with high density and large scalar force are found. These particles are more likely to reside in the halo centers, where the temperature profile is not necessarily monotonic.

3.3.5 Smoothing and Clumping Effects

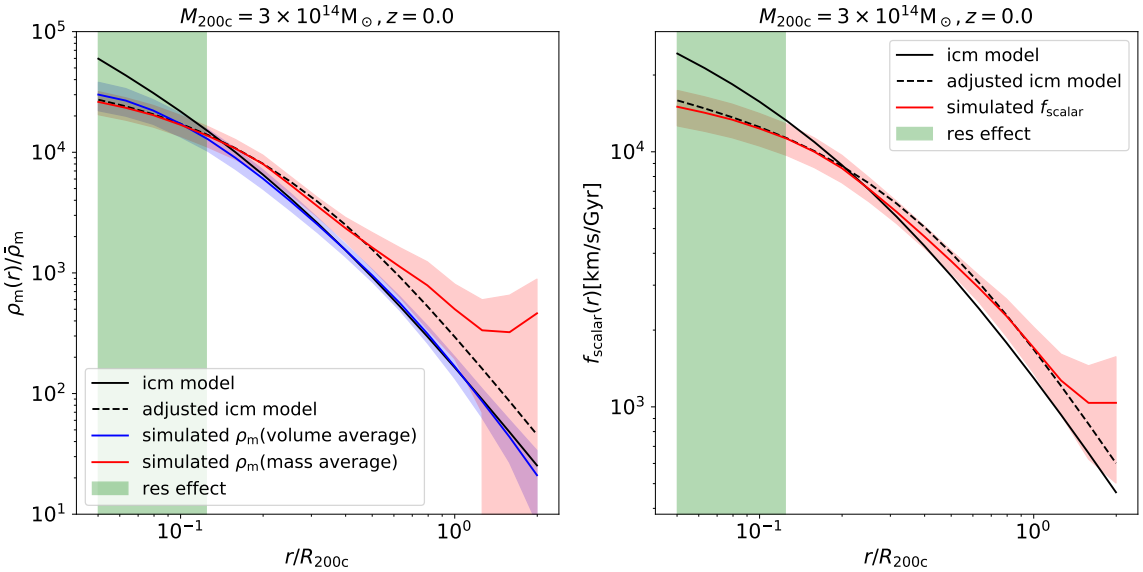

Figure 3.3: Halo profiles of the HPM variables, matter density (left) and the scalar force (right), of halo mass bin centered at $3 \times 10^{14} M_\odot$ at redshift $z = 0.0$. Also shown is the resolution limit of the simulation (thin green band), where the simulated radial profiles of the HPM variables systematically deviate from the adopted ICM model. The volume weighted profiles of both the mass density and the scalar force of simulated halos (solid blue lines) are in good agreement with the NFW profile of the ICM model (solid black lines), except in the inner core, where they suffer from the limited resolution of the simulation. The mass weighted profiles (solid red lines) are greater than the ICM model at larger radii, and agree better with the adjusted ICM model described in the text (dashed black lines). The scatter of the volume weighted mass density profile (thin blue band) shows less dependence on the radius than the mass weighted one (thin red band).

In the HPM simulation, due to the finite resolution of the mesh and the finite number of particles, the simulation results in the highest density regions like the inner cores of simulated halos suffer from a smoothing effect, which leads to underestimating output quantities of the simulation like the density and the scalar force. In addition, few of the simulated halos are completely relaxed (especially in the outskirts) or perfectly spherical, which violates the spherical symmetry assumption in the ICM model. We refer to the asymmetry and inhomogeneity in the distribution of particles in the outskirt region of simulated halos as the clumping effect. Both the smoothing effect and the clumping effect will cause the deviation of the simulated profiles for the HPM variables from the ICM model prediction. The smoothing effect will lead to an underestimation of simulated HPM variables calculated for the gas particles in

the halo inner region, while the clumping effect in the outer region will lead to an overestimation.

In Figure 3.3 we show the comparison between the radial profiles of HPM variables, the matter density and the scalar force, and their ICM model predictions calculated for gas particles of simulated halos within the halo mass bin centered at $3 \times 10^{14}\mathrm{M}_{\odot}$ at redshift $z = 0$. In both panels the simulation results tend to underestimate the HPM variables from the ICM model in the inner core region due to the smoothing effect of the finite numerical resolution of the simulation. Outside the core the volume weighted matter density profile is in good agreement with the NFW profile. We also find that the mass weighted profiles are significantly higher than the volume weighted ones, which indicates that the clumping effect in the outer regions of simulated halos is non-negligible.

Notice that since we infer the gas pressure or temperature from the HPM variables calculated for each particle, the offset between the simulation results and the ICM model would introduce bias to the inference of gas temperature or pressure with the HPM table and will result in incorrect dynamics in simulation. We must treat the smoothing and clumping effects carefully when using the HPM variables calculated for each gas particle to model their thermal properties in the simulation. In Figure 3.4 we plot the temperature profiles of simulated halos within the mass bin centered at $M_{200\mathrm{c}} = 3 \times 10^{14}\mathrm{M}_{\odot}$ at redshift $z = 0.5$, where the temperature of gas particles are interpolated from the HPM table built with the original ICM model. Ignoring the smoothing and clumping effects on HPM variables results in underestimating the temperature of gas particles in the center of the halo and an overestimating it in the outer region, and the deviation from the ICM model prediction on the gas temperature could be up to 20%.

The reason for this mismatch is that the smoothing effect in the inner region of simulated halos suppresses magnitude of the HPM variables to the values below the ICM model prediction. According to the HPM table we show in Figure 3.2, the HPM variables have a significantly positive correlation with the temperature. Thus, underestimating the HPM variables means we are also very likely to underestimate the inferred temperature simultaneously. Then gas particles that reside in the halo center are more likely to be assigned a temperature value that is biased low. In the outer region of simulated halos the clumping effect leads to HPM variables for a substantial number of particles being higher than the ICM prediction. Due to the same reason that temperature and HPM variables are positively correlated in the HPM table, overestimating of the HPM variables leads to the temperature of gas being too high in the outer region.

To mitigate this inconsistency in the temperature inference caused by the limited resolution and break down of spherical symmetry, we need to take the smoothing and clumping effects into account while building the halo table. We first run a dark matter only simulation and fit a calibration function $C(r, \zeta)$ to the ratio of simulated profiles of HPM variables to their ICM model predictions, which enables us to capture

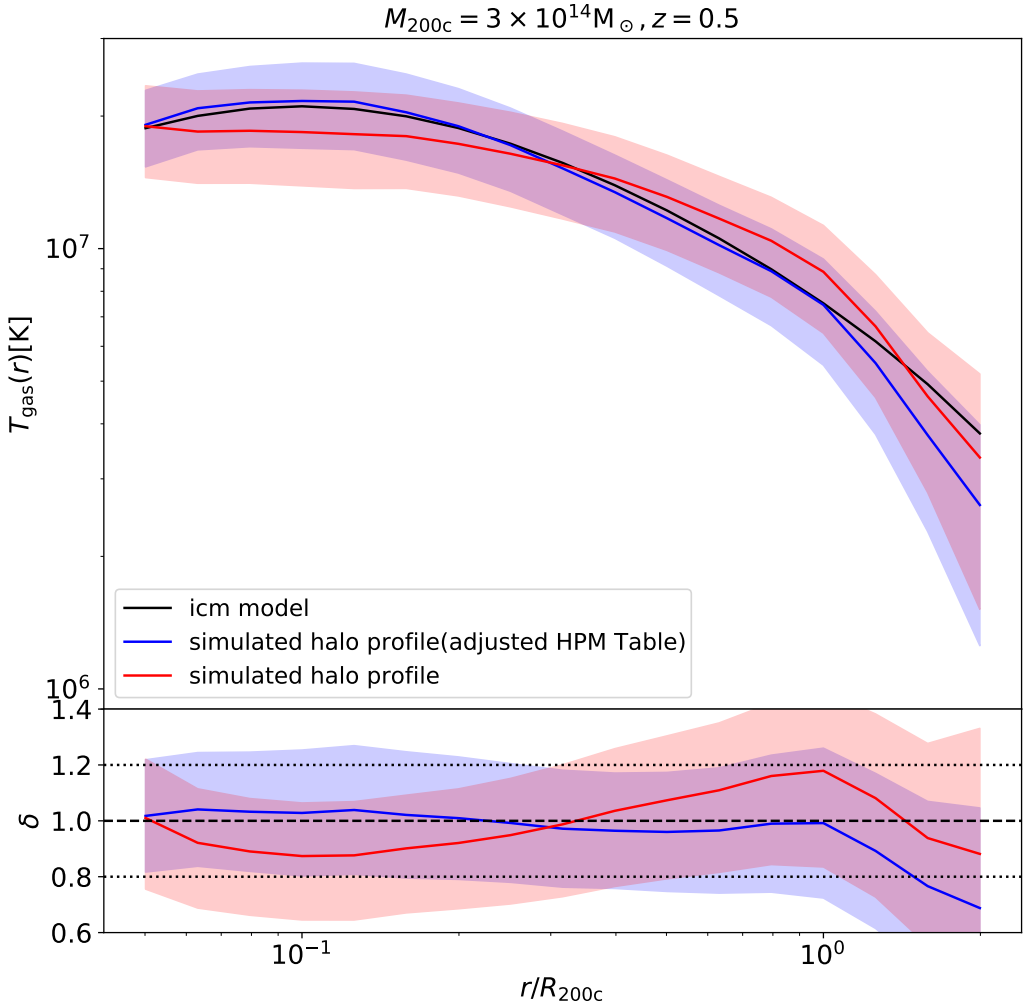

Figure 3.4: **Top:** Stacked temperature profiles of simulated halos (solid lines) and the scatter (thin bands) for the mass bin centered at $3 \times 10^{14} M_\odot$ at redshift $z = 0.5$. The profile measured in the simulation using the HPM table built on the original ICM model (red) underestimates the gas temperature in the inner region and overestimates the temperature in the outskirts up to 20%. The temperature profile measured in the simulation that uses the HPM table adjusted for smoothing and clumping effect (blue) agrees better with the temperature profile of the ICM model (black). **Bottom:** Relative difference of simulated profiles with the ICM model and a $\pm 20\%$ region (dotted black lines)

the differences between the simulation results and the original ICM model. We have discussed in Section 3.3.3 that the HPM variables are only mildly affected by the gas distribution, so the profiles of HPM variables derived from the dark matter only simulation can properly emulate their values in an HPM simulation. We verified

that the offset between simulated profiles of HPM variables and their ICM model predictions measured in the dark matter only simulation and HPM simulation were indeed very similar.

The calibration function measured from a dark matter only simulation can effectively correct the gas temperature or pressure inference in HYPER. We adjust the calculation with the fitted calibration function when deriving the HPM variables in the halo table as

$$\begin{aligned} \hat{\rho}_{\rm m}^{(i,j)} &= \rho_{\rm m}(M_i, r_j) * C_{\rho_{\rm m}}(r_j, \zeta), \\ \hat{f}_{\rm scalar}^{(i,j)} &= f_{\rm scalar}(M_i, r_j) * C_{f_{\rm scalar}}(r_j, \zeta), \end{aligned} \tag{3.37}$$

where ζ refers to any information needed to specify numerical resolution. The HPM table built with the adjusted halo table more accurately relates the HPM variables of simulated particles to their thermal properties and better approximates the hydrodynamics of gas particles through the ICM model. The profiles of HPM variables adjusted for the calibration functions are also shown in Figure 3.3. More details about the calibration functions are presented in Section 3.6.1.

After adjusting the HPM table for the effects mentioned above, we show in Figure 3.4 that the temperature inferred from the adjusted HPM table is in good agreement with the ICM prediction. We observe a downturn in the radial temperature profile beyond $R_{\rm 200c}$, which is due to the existence of a substantial amount of low-temperature IGM gas at the outskirt region of the massive halos.

3.3.6 Artificial Viscosity and Pressure Filtering

Shocks are a generic feature of gas flows. When solving the fluid equations in a particle-based simulation like SPH, the entropy generation on shocks is captured by an artificial viscosity term. HYPER is a Lagrangian particle method for the dynamical evolution of gas similar to SPH, and hence needs an artificial velocity term in the gas momentum equation:

$$\frac{{\rm d}\vec{v}_{\rm gas}}{{\rm d}\tau} = -\nabla\Phi - \frac{\nabla P}{\rho_{\rm gas}} - \vec{a}^{\rm visc}. \tag{3.38}$$

Though we don't need to resolve the conversion between kinetic energy and thermal energy in HYPER as the thermal properties of gas are directly inferred from the HPM table built on the ICM model, we still need to include the artificial viscosity term to prevent particle interpenetration in shocks. The artificial viscosity in HYPER removes the part of the kinetic energy that should be converted into heat. Otherwise, we won't be able to accurately resolve the motion and distribution of the gas in our simulation (Section 3.6.2). Many different forms have been suggested for the artificial viscosity, with the Von Neuman-Richtmyer artificial viscosity being the simplest one:

$$\vec{a}^{\rm visc} = \frac{\nabla Q}{\rho_{\rm gas}} \tag{3.39}$$

with

$$Q = \begin{cases} \alpha h \rho_{\rm gas} c |\nabla \cdot \vec{v}| + \beta h^2 \rho_{\rm gas} |\nabla \cdot \vec{v}|^2 & \nabla \cdot \vec{v} < 0, \\ 0 & \nabla \cdot \vec{v} \geq 0, \end{cases} \tag{3.40}$$

where h is the particle smoothing length, proportional to the local mean inter-particle separation, $h \propto \rho_{\rm gas}^{-1/3}$; c is the speed of sound of gas. In this work, $\alpha \sim 0.1, \beta \sim 0.05$ are found to be the best fit values when calibrating the gas radial profiles and scaling relations of different integrated quantities of the simulated halos. The viscosity term we adopt has a similar form as the gas pressure force term $\nabla P/\rho_{\rm gas}$, with Q acting as an excess pressure assigned to gas particles. To integrate the artificial viscosity in HYPER, we only need to solve the dynamical equation for gas particles 3.23 with the modified pressure $\nabla(P+Q)/\rho_{\rm gas}$.

In our HPM simulation, in addition to adopting the artificial viscosity for gas particles, we also apply a force filter on the pressure force $\nabla P/\rho_{\rm gas}$. This approach aims to sustain a proper hydrostatic equilibrium in the central core region of simulated halos, since the interpolated temperature of gas particles in the center of the halos suffers is not affected as much by the smoothing effect of finite resolution as the gas density, and that in turn leads to less smoothing of the gas pressure compared to the gravitational force. Filtering on the small-scale structure of the pressure field will impose a same degree of smoothing effect on the hydro force as the gravitational force in the center region of the simulated halos. Filtering also suppresses the numerical noise introduced by the interpolation of gas temperature from a model-based HPM table. We filter the gas pressure field in the Fourier space by

$$\tilde{P}^f(\vec{k}) = \tilde{P}(\vec{k}) f(\vec{k}) \tag{3.41}$$

and the filtered pressure force is given by replacing the gas pressure P in $\nabla P/\rho_{\rm gas}$ with the filtered pressure P^f. For the specific functional form for the filtering we adopt the Weibull function

$$f(\vec{k}) = A_{\rm L}^f - (A_{\rm L}^f - A_{\rm H}^f) \exp[-(A_{\rm S}^f k)], \tag{3.42}$$

where $A_{\rm H}^f = 1.0$ for the high frequency filter. Parameters $A_{\rm L}^f$ and $A_{\rm S}^f$ are tuned to match the simulated results with the ICM model predictions: $A_{\rm L}^f = 0.5, A_{\rm S}^f = 10.0$.

A combination of the artificial viscosity and filtering on gas pressure helps to prevent too much gas from being ejected of the halos in our simulation and to ensure we get a reasonable gas fraction for the simulated halos. Tuning the small scale filter and artificial viscosity are presented in Section 3.6.2.

3.4 Results

In this section we compare the results from a HYPER simulation to the predictions of the ICM model used to implement the HPM mapping relation for gas thermal properties. Good consistency in the properties of the ICM such as the radial profiles, scaling relation of integrated halo properties, and measurements of the tSZ effect implies one can systematically control the ICM physics in HYPER simulation by varying the ICM model while constructing the HPM mapping relation.

3.4.1 Halo Radial Profiles

We first compare the profiles of matter density and gas thermal properties of simulated halos to the profiles derived with the ICM model. In Figure 3.5 we show the radial profiles of matter density and their scatter for the simulated halos whose masses fall into three mass bin centered at $10^{14}\mathrm{M}_{\odot}$, $3\times10^{14}\mathrm{M}_{\odot}$, and $10^{15}\mathrm{M}_{\odot}$ at redshift $z=0$ and $z=0.5$. We find that the volume-weighted density profiles agree with the NFW model well except in the inner region, where they suffer from the smoothing effect due to the limited resolution of the simulation. The clumping effect in the mass-weighted density profiles mentioned in Section 3.3.5 leads to an overestimate of the matter density at the outskirts of halos.

In Figure 3.6 we plot the simulated profiles of gas density, temperature, and pressure and their scatter for the halos whose masses fall into the mass bin centered at $3\times10^{14}\mathrm{M}_{\odot}$ at redshift $z=0$ and $z=0.5$. We also plot the prediction for the gas profiles in the ICM model used for implementing the hydro part of the simulation for comparison, and we also show the ratio of simulated profiles to the ICM model predictions in the bottom panels. We find that the radial profiles of the gas density, temperature, and pressure for simulated halos are in about 5% agreement with the ICM model from $0.1R_{200\mathrm{c}}$ to $R_{200\mathrm{c}}$ and remain within 20% even in the inner core and in halo outskirts up to about $1.5R_{200\mathrm{c}}$.

In the inner core we observe the smoothing effect due to the limited resolution of the simulation in the gas density and pressure profiles. An analogous smoothing effect in the simulated gas temperature profiles in the halo centers is much less significant because we already account for the numerical resolution effect when constructing the HPM table.

3.4.2 Integrated Halo Quantities

X-ray observables, such as luminosity, temperature, mass of the ICM, and SZ flux of galaxy clusters have been proposed and used as proxies for the total cluster mass (e.g. Voit, 2005). Calibrating relations between cluster mass and these observables is important for exploiting the full statistical power of the cluster surveys. In this section we show further comparison between the simulation results and the ICM

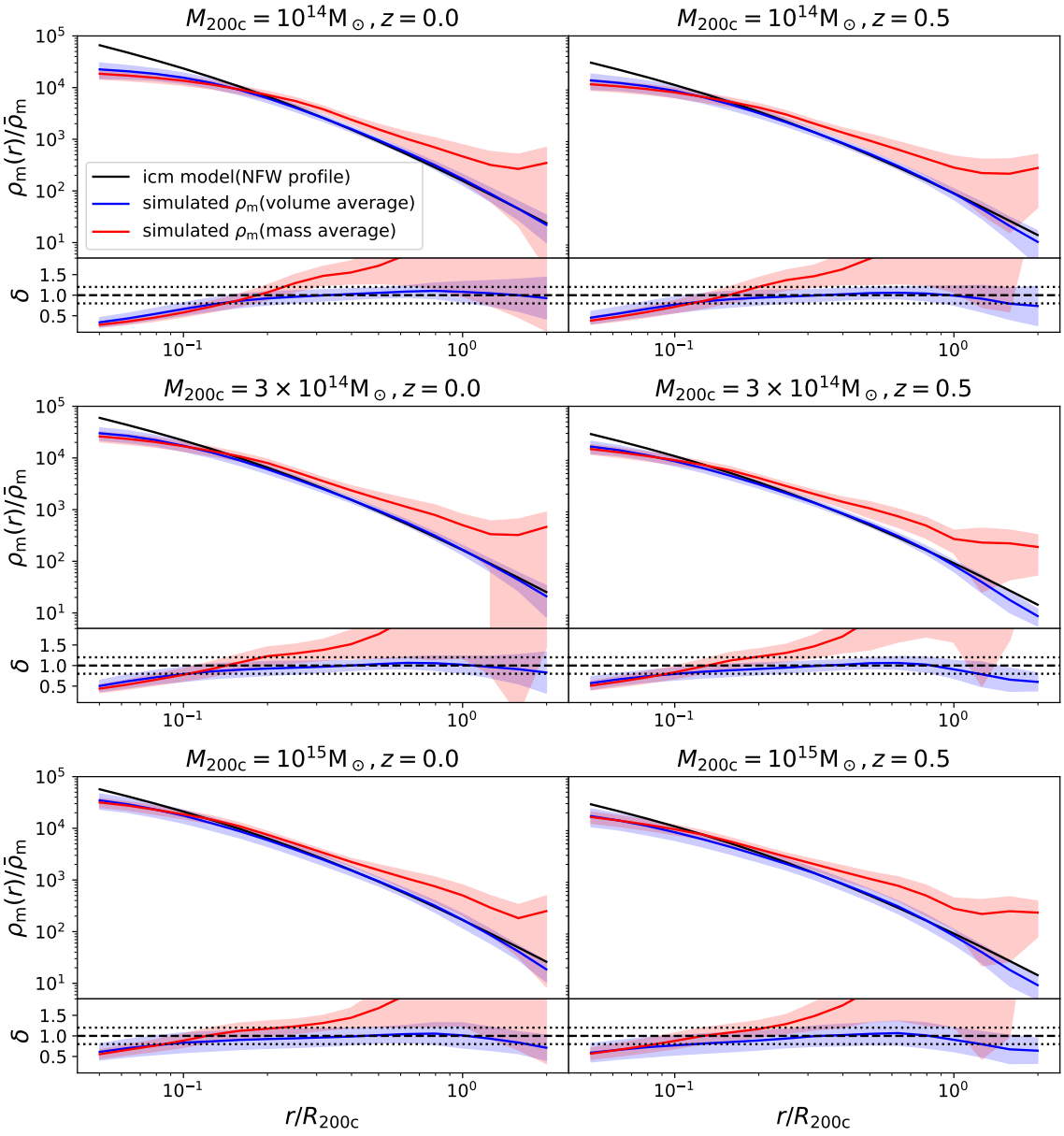

Figure 3.5: Comparison between the simulation results and the ICM model (NFW profile) for the radial profiles of matter density for halos in mass bins centered at $10^{14} M_\odot$ (1st row), $3 \times 10^{14} M_\odot$ (2nd raw), and $10^{15} M_\odot$ (3rd raw) at redshift $z = 0$ (1st column) and $z = 0.5$ (2nd colum). In each plot the top panel shows that the simulated volume weighted matter density profile (blue line) agrees well with the NFW profile (black line). In contrast, the mass weighted matter density profile (red line) overestimates the matter density in the outskirt region compared to the standard ICM model due to the clumping effect. Also shown are the scatter in the simulated matter density profiles (thin blue/red bands); the bottom panel shows the ratio between the simulation results and the ICM model and a $\pm 20\%$ region (dotted black lines).

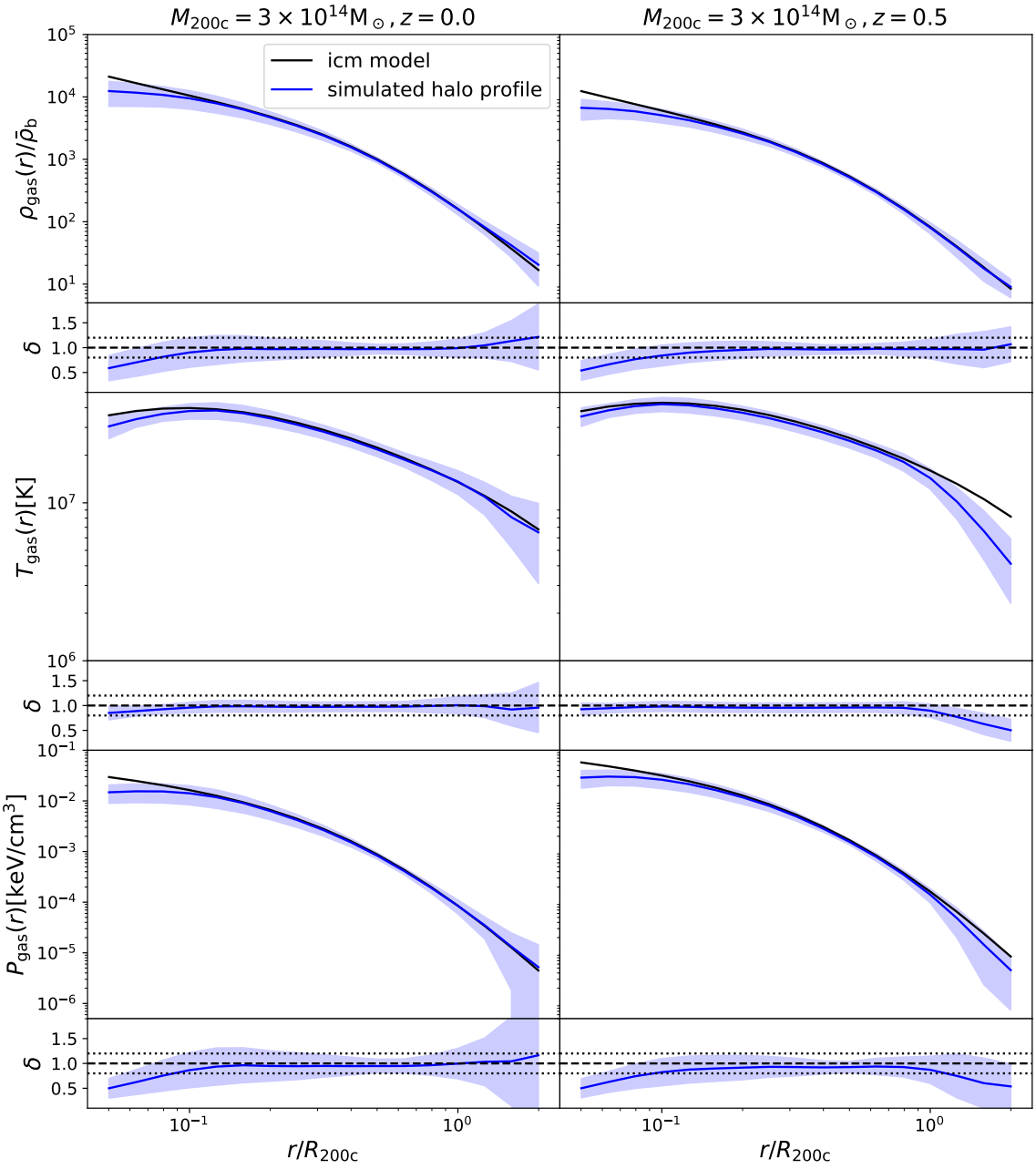

Figure 3.6: Comparison between the simulation results and the ICM model prediction for the volume weighted radial profiles of gas density (1st raw) and pressure (3rd raw) and mass-weighted temperature (2nd raw) for halos in mass bins centered at $3 \times 10^{14} M_\odot$ at redshift $z = 0$ (1st column) and $z = 0.5$ (2nd column). For each plot, the top panel shows the simulated halo profile and its scatter (blue line and band), which is found to be in good agreement with the profile of the ICM model (black line); the bottom panel shows the ratio between the simulation results and the ICM model and a $\pm 20\%$ region (dotted black lines).

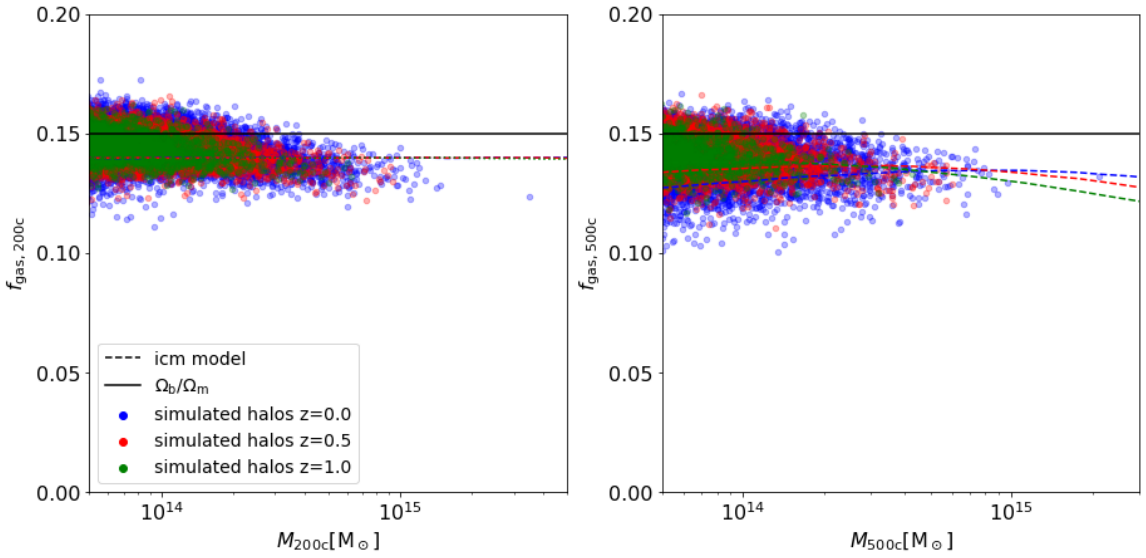

Figure 3.7: Gas fraction of simulated halos (dots) compared to the ICM model prediction (dashed lines) at different redshift $z = 0$ (blue), $z = 0.5$ (red), and $z = 1.0$ (green) within a spherical region with the mean overdensity 200 (left) and 500 (right) times of critical density. The halo gas fractions in the simulation are lower than the universal baryonic fraction $\Omega_{\rm b}/\Omega_{\rm m} = 0.15$ for the adopted cosmology (solid black line).

model predictions by investigating the integrated quantities of identified halos and exploring the scaling relation between the SZ effect signal, X-ray observables and halo masses in the simulation.

In Figure 3.7, we plot the gas fractions of simulated halos enclosed within spheres with the averaged density of 200 and 500 times the critical density respectively at different redshifts $z = 0, 0.5, 1.0$. For comparison, we also plot the gas fraction derived from the ICM model and the universal baryonic fraction $f_{\rm b} = \Omega_{\rm b}/\Omega_{\rm m}$ where $\Omega_{\rm b}$ and $\Omega_{\rm m}$ are the cosmological parameters set for the simulation. As shown in the plots, after implementation of gas pressure in solving motion of baryonic components in the simulation, the gas fraction of simulated halos are substantially lower than the fraction baryon mass takes of the mass of all the matters in the universe, which means a considerable portion of gas gets propelled out of the gravitational potential well of collapsed halos due to existence of gas pressure. Furthermore, we find simulation results of gas fraction match the prediction derived from analytical models of gas pressure profiles by assuming hydrostatic equilibrium reasonably well. Scatter in the results of simulated halos is not negligible, as the dynamical state of different halos can vary significantly in a real simulation. We observe slightly more scatter inside the radius encompassing the overdensity of 500 times the critical density, since the inner

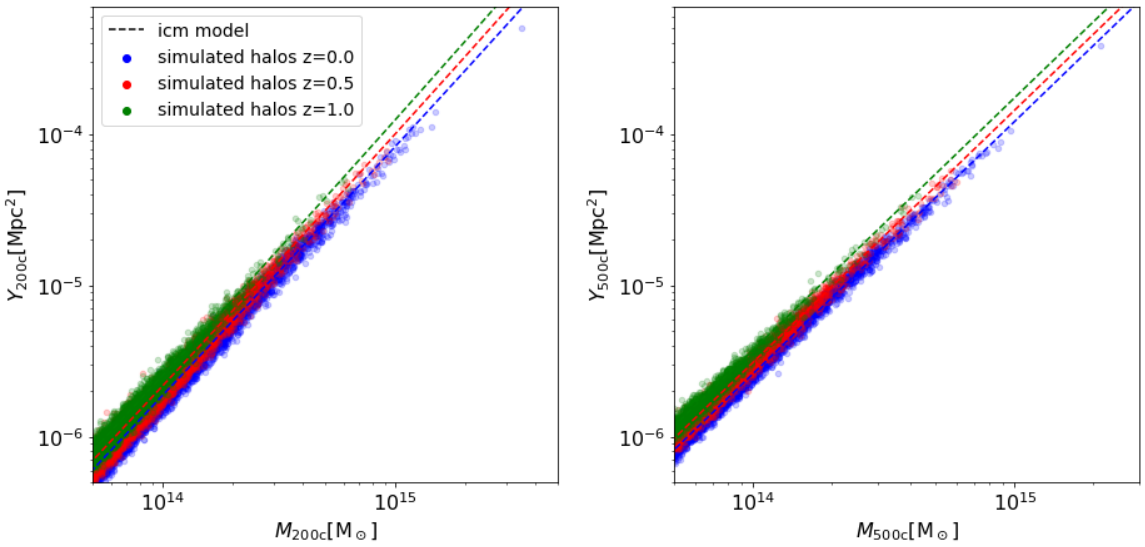

Figure 3.8: Integrated Compton-Y parameter within a spherical region with the mean overdensity of 200 (left) and 500 (right) times the critical density for simulated halos (dots) compare with the ICM model prediction (dashed lines) at different redshifts $z = 0$ (blue), $z = 0.5$ (red) and $z = 1$ (green).

region is more sensitive to the dynamic state of the halos. The failure of simulation to resolve the inner cores of halos may also contribute to the overall scatter.

In Figure 3.8, we plot the Compton Y-parameter integrated over a spherical volume,

$$Y_{\mathrm{R}} = \frac{\sigma_{\mathrm{T}}}{m_{\mathrm{e}}c^2} \int_0^R 4\pi P_{\mathrm{e}}(r) r^2 \mathrm{d}r, \tag{3.43}$$

for the simulated halos and compare it with the $Y - M$ relation derived from the gas pressure model for two different mass definitions at different redshifts. The Compton parameter $Y_{200\mathrm{c}}$ and $Y_{500\mathrm{c}}$ integrated within a spherical region with the mean overdensity of 200 and 500 times the critical density of simulated halos is consistent with the $Y - M$ relation derived from the gas pressure model, which is not surprising since Figure 3.6 shows that the simulated gas pressure profiles agree well with the analytical pressure model. Scatter in the $Y - M$ scaling relation in the simulation is smaller than the scatter in gas fractions and other X-ray observables; apparently the Compton Y signal of simulated halos is less affected by the poorly resolved inner core region. Our results agree with the conclusion in other studies of the SZ effect (e.g. Komatsu & Seljak, 2002) that the Compton Y signal is less sensitive to gas physics in the core of clusters.

In Figure 3.9 we plot the bolometric X-ray luminosity L_{X},

$$L_{\mathrm{X}} = \int \Lambda(T) n_{\mathrm{gas}}^2 \mathrm{d}V, \tag{3.44}$$

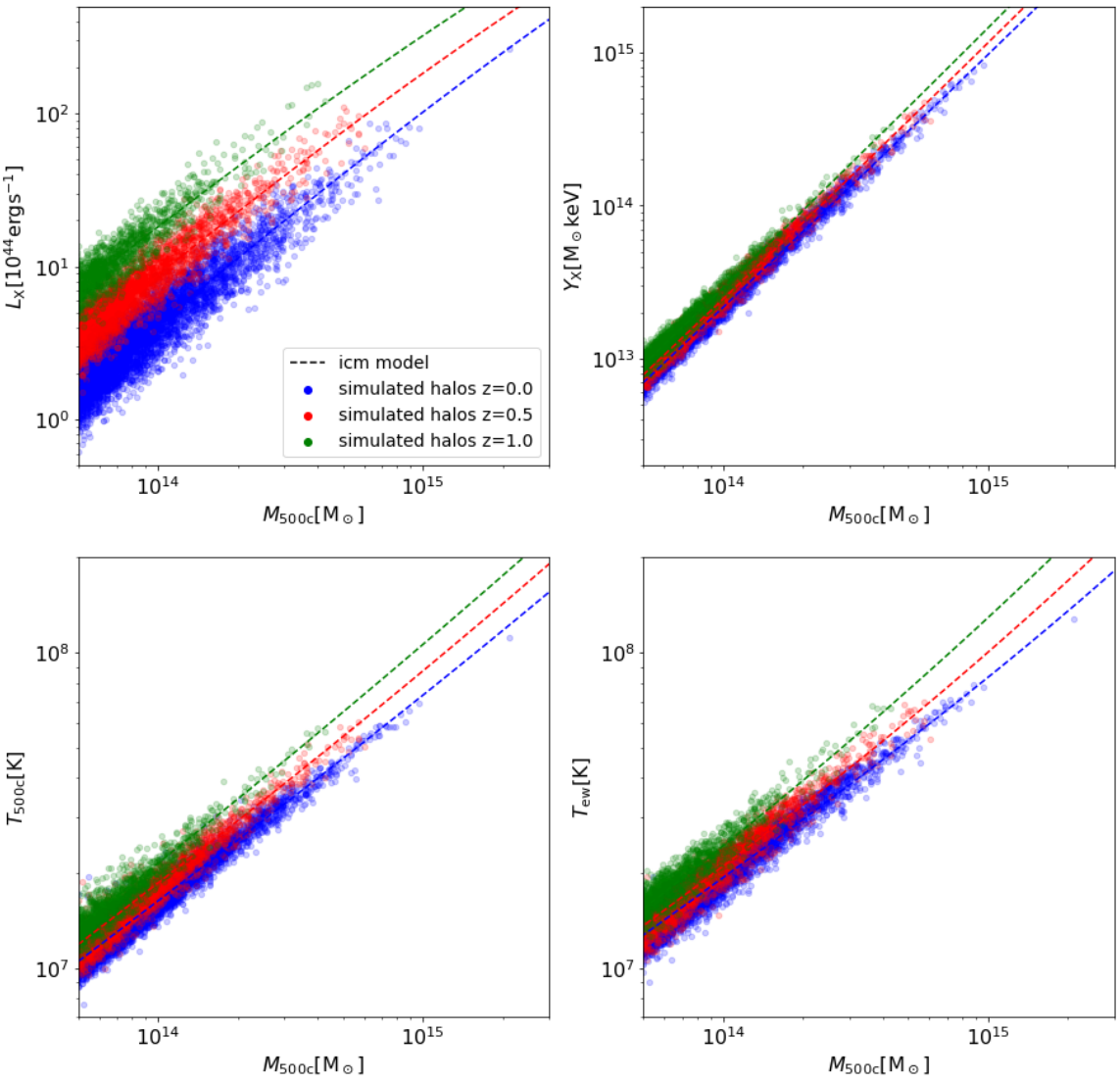

Figure 3.9: Integrated X-ray quantities: the bolometric X-ray luminosity (top left), the spherical Compton-like Y_x parameter (top right), the mass-weighted average temperature (bottom left), and the emission-weighted temperature (bottom right) of the simulated halos (dots) compared with the ICM model prediction (dashed lines) at different redshifts $z = 0$ (blue), $z = 0.5$ (red) and $z = 1$ (green).

where $\Lambda(T) \propto \sqrt{T}$ is the cooling function assuming that Bremsstrahlung emission dominates, and $n_{\rm gas}$ is the gas density. We also plot the emission weighted temperature $T_{\rm ew}$

$$T_{\rm ew} = \frac{\int \Lambda(T) n_{\rm gas}^2 T \mathrm{d}V}{\int \Lambda(T) n_{\rm gas}^2 \mathrm{d}V}. \tag{3.45}$$

Another common X-ray observable is the $Y_{\rm X}$ parameter (Kravtsov et al., 2006), proportional to the gas thermal energy as defined by the product of the gas mass and the spectroscopic X-ray temperature,

$$Y_{\rm X} = M_{\rm gas} T_{\rm X}, \tag{3.46}$$

where $M_{\rm gas}$ is the gas mass within the spherical overdensity region of radius $R_{\rm 500c}$ and $T_{\rm X}$ is the spectroscopic X-ray temperature. Finally, we also show in Figure 3.9 the characteristic temperature $T_{\rm 500c}$,

$$T_{\rm 500c} = \frac{\mu_{\rm e} m_{\rm e} m_{\rm p} c^2}{k_{\rm B} \sigma_{\rm T}} \frac{Y_{\rm 500c}}{M_{\rm gas}}. \tag{3.47}$$

Scaling relation of the integrated X-ray quantities and halo mass in the simulation results are in good agreement with the ICM gas model predictions from redshift $z = 0$ to $z = 1$. Notice that all these X-ray observables are exclusively defined by the density and the temperature of the gas in halos. Since we have shown in Figure 3.6 that the radial profiles of both gas density and temperature are in good agreement with the analytical model, this explains the consistency between the integrated X-ray quantities of the simulated halos and the ICM model prediction. Simulation results for the $Y_{\rm X} - M$ relation have been shown to have less scatter than the $L_{\rm X} - M$ relation, which may be due to the anti-correlation between the deviation of $M_{\rm gas}$ and $T_{\rm X}$ from the scaling relation prediction, which has been found in X-ray observations (Kravtsov et al., 2006).

We also look into the scatter about the scaling relation in HYPER simulation, as it could reflect the information on important dynamical effects. Gupta et al. (2017) studies the scatter about $Y - M$ relation in the Magneticum simulation and finds that the scatter $\sigma_{\ln Y}$ about the mass-observable relations at overdensity 500c is consistent with the lognormal distribution. We also calculate the distribution of scatter about the $Y_{\rm 500c}$-$M_{\rm 500c}$ relation in HYPER and fit it to a lognormal distribution. We find that the rms scatter $\sigma_{\ln Y} = 0.094 \pm 0.002$ is in good agreement with the value $\sigma_{\ln Y} = 0.088 \pm 0.006$ from the Magneticum simulation. We show the probability distributions of scatter about the $Y_{\rm 500c}$-$M_{\rm 500c}$ for HYPER and its best lognormal fit, as well as the best-fit lognormal from the Magneticum simulation in Figure 3.10. We also measure the scatter about the X-ray observable-mass relation by calculating the RMS dispersion

$$\sigma_{\log_{10} Y} = \sqrt{\frac{1}{N} \sum_{i=1}^{N} \left[\log_{10}(Y_i) - \log_{10}(Y_{\rm model})\right]^2} \tag{3.48}$$

following Barnes et al. (2017), where Y_i is the X-ray observables as i runs over all simulated halos and $Y_{\rm model}$ is the corresponding ICM model prediction. We present the comparison between our measurement for the scatter about $L_{\rm X} - M_{\rm 500c}$, $Y_{\rm X} - M_{\rm 500c}$, and $T_{\rm 500c} - M_{\rm 500c}$ and the MACSIS simulation results in Table 3.1.

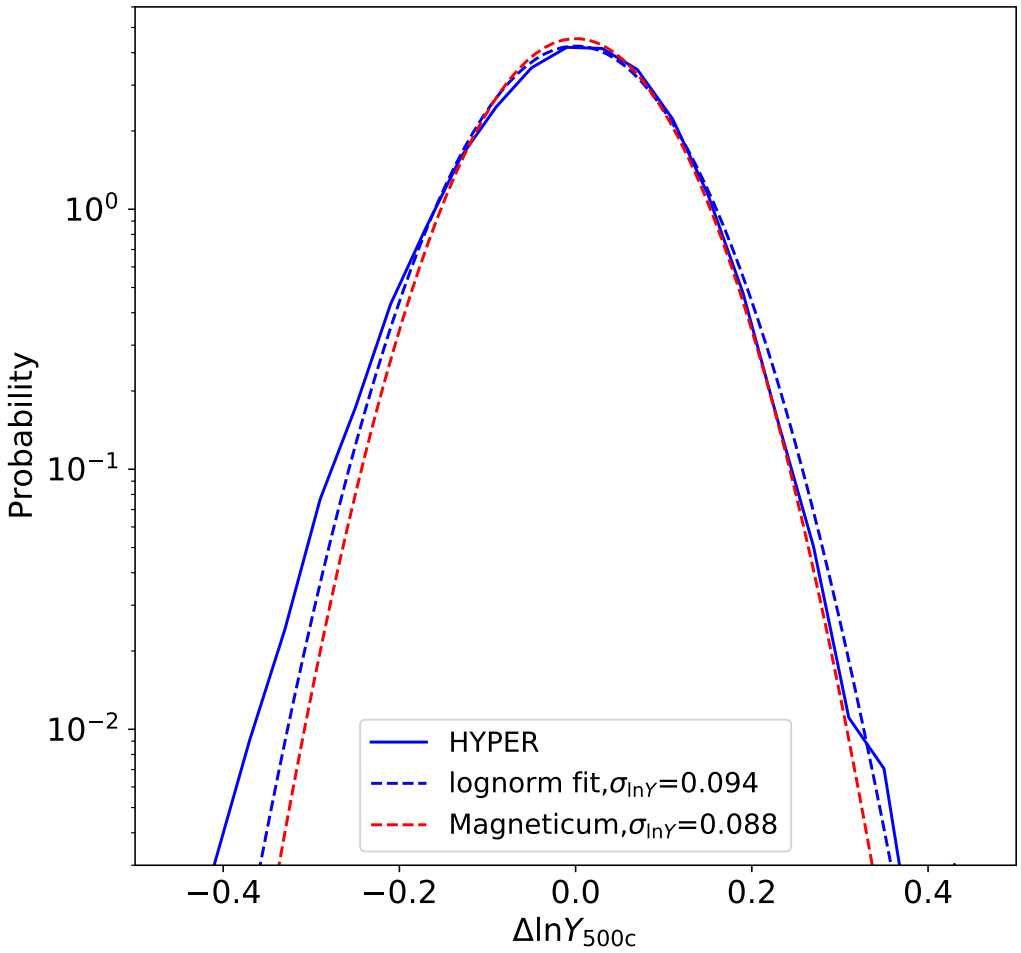

Figure 3.10: Probability distribution of the scatter about the Y_{500c}-M_{500c} relation for the HYPER simulation output at redshift $z = 0.0$ (solid blue line), and its best lognormal fit (dashed blue line). The lognormal fit to the Magneticum simulation output at redshift $z = 0.0$ (dashed red line) is also shown for comparison and agrees well with the HYPER results.

$\sigma_{\log_{10}Y}$	L_X-M_{500c}	Y_X-M_{500c}	T_{500c}-M_{500c}
HYPER	0.153	0.083	0.038
MACSIS	0.15 ±0.02	0.12 ±0.01	0.048 ±0.003

Table 3.1: Scatter about the X-ray observable - mass relation for HYPER and MACSIS at redshift $z = 0$.

We find the scatter about the scaling relation in HYPER is in general consistent with the state-of-art full hydro simulations, suggesting that HYPER captures the important dynamical effects modeled in full simulations. However, to further verify this point, we need to adopt the ICM model drawn from the full hydro simulations to construct the HPM table for inferring the gas thermal properties. Studies show that the ICM physics could also affect the scatter about the scaling relation (e.g. Battaglia et al., 2012). The excellent agreement on the scatter about the $Y_{500c} - M_{500c}$ relation between HYPER and Magneticum may result from the ICM gas pressure model we adopt being similar to that found in the Magneticum simulation, which implies HYPER adopting current ICM model may properly emulates the ICM physics in Magneticum simulation and the good match on the scatter is a result of a more fair comparison. Hence, more detailed comparison for scatter about the observable-mass relation of HYPER and full hydrodynamic simulations is required in the future study.

3.4.3 Thermal SZ Angular Power Spectrum

The tSZ power spectrum C_ℓ is a powerful probe of cosmology and can provide promising constraints on cosmological parameters, in particular σ_8, since $C_\ell \propto \sigma_8^{7-9}$ (e.g. Komatsu & Seljak, 2002; Shaw et al., 2010; Trac et al., 2011). Because the cluster signal dominates tSZ anisotropies, we can model the analytical prediction of the tSZ power spectrum using the standard halo model (e.g. Cole & Kaiser, 1988; Komatsu & Kitayama, 1999). The tSZ angular power spectrum at a multipole moment ℓ for the one-halo term is given by

$$C_\ell^{\rm tSZ} = f^2(\nu) \int_z \frac{{\rm d}V}{{\rm d}z} \int_M \frac{{\rm d}n(M,z)}{{\rm d}M} |\tilde{Y}_\ell(M,z)|^2 {\rm d}M {\rm d}z, \tag{3.49}$$

where $f(\nu) = x_\nu \coth(x_\nu/2) - 4$ with $x_\nu = h\nu/(k_{\rm B}T_{\rm CMB})$ is the spectral shape of the tSZ signal. Integration over redshift and mass are carried out from $z = 0$ to $z = 5$ and from $M = 10^{10}{\rm M}_\odot$ to $M = 10^{16}{\rm M}_\odot$ respectively. For the differential halo mass function ${\rm d}n(M,z)/{\rm d}M$ we adopt the fitting function from Tinker et al. (2008) based on N-body simulations.

Following Komatsu & Seljak (2002), the 2D Fourier transform of the projected Compton Y-parameter, $\tilde{Y}_\ell(M,z)$ is given in the Limber approximation (Limber, 1953) as

$$\tilde{Y}_\ell(M,z) = \frac{4\pi r_{\rm s}}{\ell_{\rm s}^2} \frac{\sigma_{\rm T}}{m_{\rm e}c^2} \int x^2 P_{\rm e}(x) \frac{\sin(\ell x/\ell_{\rm s})}{\ell x/\ell_{\rm s}} {\rm d}x, \tag{3.50}$$

where $x = r/r_{\rm s}$ is a scaled dimensionless radius, $r_{\rm s}$ is characteristic radius for a NFW profile defined as R_{500c}/c_{500c}, and we use the average halo concentration c_{500c} calibrated as a function of the cluster mass and redshift from Diemer & Kravtsov (2015). The corresponding angular wave number $\ell_{\rm s} = d_{\rm A}/r_{\rm s}$, where $d_{\rm A}(z)$ is the proper angular-diameter distance at redshift z. Here $P_{\rm e}(r) = P_{\rm th}(r)\mu/\mu_{\rm e}$ is the electron pressure, and μ and $\mu_{\rm e}$ are the mean mass per gas particle and per electron

respectively, and $P_{\rm th}(r)$ is the gas thermal pressure profile of the ICM model we discuss in Section 3.2. The integral is carried out within a spherical region with radius $R \sim 4R_{\rm 500c}$.

In the Limber approximation we can also relate the thermal SZ angular power spectrum to the 3D thermal pressure power spectrum by

$$C_\ell^{\rm tSZ} = \frac{16 f^2(\nu)\pi^2}{(2\ell+1)^3} \int_0^{z_{\rm max}} \Delta_{\rm tSZ}(k,z)|_{k=\ell/\chi} \chi(z) d\chi(z), \tag{3.51}$$

where $z_{\rm max} = 5$, $\chi(z)$ is the comoving distance to redshift z, and

$$\Delta_{\rm tSZ}(k,z) = \left[\frac{\langle P_{\rm e}(z)\rangle \sigma_{\rm T}}{(1+z) m_{\rm e} c^2}\right]^2 \frac{k^3}{2\pi^2} P_p(k,z). \tag{3.52}$$

Here $P_p(k,z) = \langle \delta_P(\vec{k},z) \delta_P^*(\vec{k},z)\rangle$ is the power spectrum of the Fourier transform $\delta_P(\vec{k},z)$ of the fractional thermal pressure fluctuations $\delta_P(\vec{x},z) \equiv P_{\rm e}(\vec{x},z)/\langle P_{\rm e}(\vec{x},z)\rangle - 1$. We approximate the tSZ power spectrum as a sum over the finite number of simulation outputs,

$$C_\ell^{\rm tSZ} = \frac{16 f^2(\nu)\pi^2}{(2\ell+1)^3} \sum_i \Delta_{\rm tSZ}(\ell/\chi_i, z_i) \chi_i \Delta\chi_i, \tag{3.53}$$

and we use the fast Fourier transform to calculate the power spectrum of the gas pressure field drawn from the simulation snapshots at redshift z_i to directly estimate the thermal SZ angular power spectrum from our simulation output.

In Figure 3.11 we show the tSZ power spectrum measured from the HYPER simulation, which is calculated with the 3D power spectrum of the gas thermal pressure. We compare our result to the analytical prediction evaluated with the ICM pressure model and the halo model assuming the same fiducial cosmological parameters as adopted by simulation. We also plot the measurements of the tSZ power spectrum by Planck, which are in good agreement with the analytical calculation of the tSZ power spectrum derived from DPP in He et al. (2021a). The frequency-dependent terms are all scaled to $f^2(\nu) = 1$ for direct comparison.

The tSZ power spectrum measured with the output of the HYPER simulation is in good agreement with the analytical prediction calculated with the ICM model, within $\sim 10\%$. It shows that the HYPER simulation results are consistent with the assumed ICM model used to implement the hydrodynamics in our simulation not only for properties of simulated halos, but also for the most widely used statistical measures of the tSZ effect. According to Eq. 3.49, Compton signals of galaxy clusters dominates the contribution to the tSZ power spectrum, and we show in Section 3.4.2 that scaling relation between the Compton Y-parameter and the mass of simulated halos matches the ICM model derivation very well, which also indicates a good agreement on the tSZ power spectrum calculation.

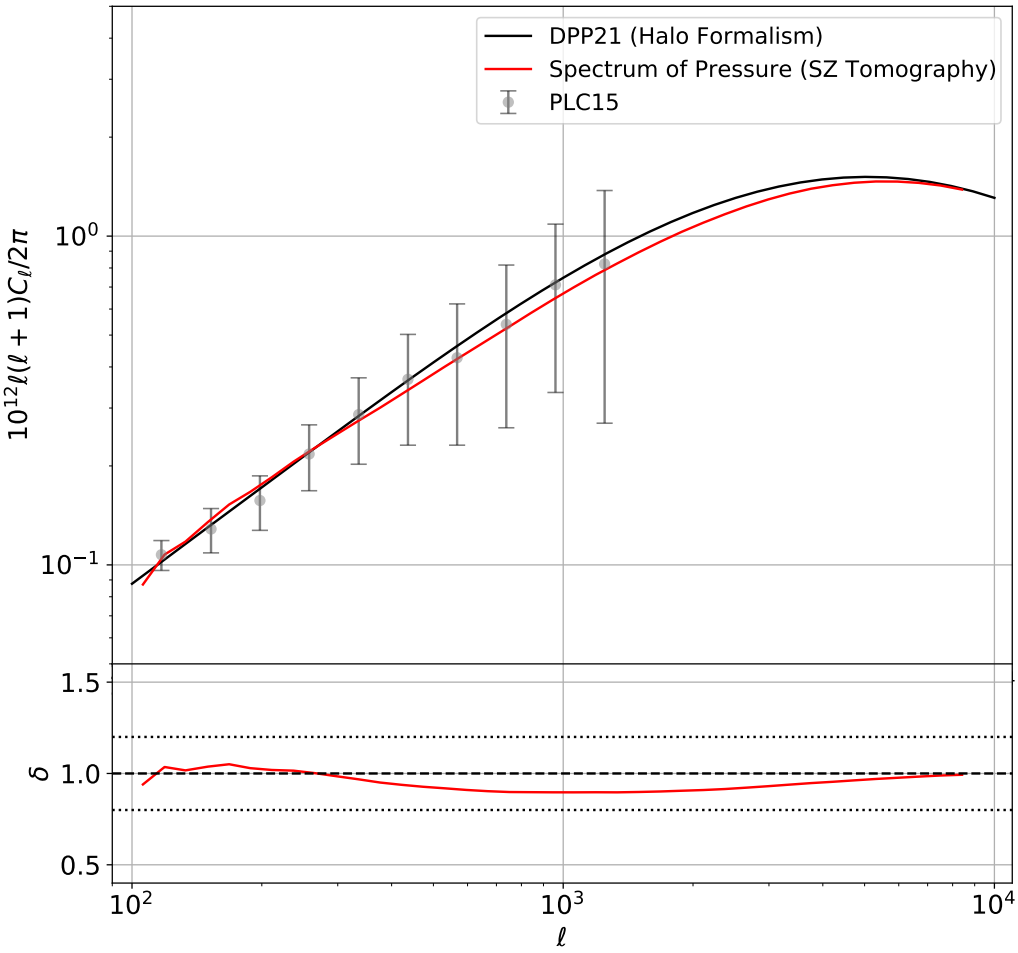

Figure 3.11: **Top:** tSZ angular power spectrum evaluated with the 3D power spectrum of the gas thermal pressure and Eq. 3.53 (red) using the outputs from the HYPER simulation at different redshifts from $z = 0$ to $z = 5$. The HYPER result agrees within around 10% with the predictions for the tSZ power spectrum calculated with the ICM pressure model used for constructing the HPM mapping relation, DPP (He et al., 2021a), and the halo formalism (black line). Planck 2015 analysis (Planck Collaboration et al., 2016a) of the tSZ power spectrum (gray dots) with error bars due to uncertainties of foreground contamination and statistical errors is also plotted for comparison. **Bottom:** Ratio of the tSZ power spectrum evaluated from the simulation outputs to the analytical prediction (red line) and ±20% region (dotted black lines).

3.5 Conclusion and Discussion

In this chapter we introduce HYPER, a new implementation of a fast approximate hydro simulation based on an N-body solver. HYPER applies a power-law density-temperature relation for the gas in the IGM regime of low-density and constructs a mapping relation between two designed HPM variables and the gas temperature and pressure in the high-density ICM regime (which based on the adopted ICM gas pressure model) to simulate the evolution of baryonic matter in an efficient way.

We investigate the properties of gas inside the simulated halos by measuring the radial profiles of density, temperature, and pressure of the gas for the identified halos in the simulation. We also present the integrated quantities of observables in the X-ray and SZ survey and calculate the tSZ angular power spectrum from the simulation outputs. We emphasize that one of the crucial strength of HYPER is one can systematically control the gas physics of simulated halos with the adopted ICM model. We show that

1. the radial profiles of density, temperature and pressure of gas inside the identified halos in the simulation are in good agreement with the ICM model predictions within 5% for $0.1R_{200c} - R_{200c}$ and the deviation is limited to 20% in the inner core $r < 0.1R_{200c}$ and outer skirt region $R_{200c} - 1.5R_{200c}$. Mild inconsistency found in the inner region might be due to the resolution limit of the HPM solver.

2. the integrated X-ray and SZ observables of simulated halos are in good agreement with the scaling relations derived from the gas radial profiles of the ICM model at redshifts from $z = 0$ to $z = 1$. The scatter in the relation comes from two primary sources: the variations in the dynamical states of different simulated halos and the finite numerical resolution in the inner core of cluster. The latter may also contribute to the bias of the gas fraction of simulated halos as compared to the model prediction. The scatter in the simulation results of different observables is comparable to that in the full hydrodynamic simulation Magneticum and MACSIS.

3. the tSZ angular power spectrum measured for the HYPER simulation, which is calculated using the 3D power spectrum of the gas thermal pressure drawn from the simulation at different redshift snapshots, is in good agreement with the analytical predictions evaluated with the halo model and the ICM model used to implement the HPM algorithm. Good consistency in the simulation output and ICM model derivation for properties of the ICM regime includes the cluster radial profiles, SZ and X-ray observable-mass relation, and statistical quantities of the tSZ effects indicates HYPER simulation allows us to systematically control the ICM physics by varying the ICM model implemented in the HPM mapping relation construction.

We envision three main use cases for HYPER.

1. HYPER runs orders of magnitude faster than ordinary hydrodynamic simulations. It can be useful for generating a large number of mock catalogs and creating maps of various physical quantities (like X-Ray, temperature, SZ effect, etc.) for galaxy clusters. These outputs will help in the development of data reduction and analysis pipelines, for understanding systematics and selection effects, and for interpreting cosmological and astrophysical constraints. One can also envision training a multi-band deep learning model with mock observations generated by HYPER for the mass estimation and mass distribution measurement of galaxy clusters.

2. In HYPER we implement the dynamics of baryons via the HPM mapping relation built on the ICM model for the gas profiles. Modifications of the matter power spectrum due to baryonic physics are one of the major theoretical uncertainties in cosmological weak lensing measurements. The ability of HYPER simulations to efficiently model the joint effects and varied cosmological parameters is a powerful tool for studying mitigation schemes for baryonic effects in weak lensing cosmic shear measurements (e.g. Huang et al., 2019).

3. Baryonic physics such as star formation, energetic feedback, and nonthermal pressure support affect the tSZ angular power spectrum in nontrivial ways (e.g. Trac et al., 2011). The difference in gas physics is imprinted in the cluster gas pressure profile. With HYPER one can systematically vary the gas pressure model of galaxy clusters. For example, one can implement different ICM models drawn from current state-of-art high resolution hydrodynamic simulations in a large scale fast hydro simulation of size up to $\sim$ 1-2 Gpc, which would be unrealistically expensive for ordinary hydrodynamic simulations. With this approach one can systematically study how different gas physics influences, for example, the tSZ angular power spectrum. Moreover, from an inverse perspective, the efficiency of HYPER also enables us to generate a large number of mock observations, combined with proper statistic techniques (e.g. Gaussian Process) allows us to quickly explore parameter space for ICM model and use observation data of the SZ effect to put constraints on the ICM model; furthermore, it can be used to examine the gas physics implemented in cosmological simulation.

In future extensions of this work we will focus on improving the finite spatial resolution of HYPER. One avenue could be adopting an hybrid scheme combining the multigrid method with the fast Fourier transform (e.g. Kravtsov et al., 1997), which could eliminate the resolution effect in the high-density ICM regime and sustain the high computational efficiency throughout the rest of the simulation volume. It may help solve the problem of overestimating the gas velocity dispersion in the inner

region of halos. We also plan to study the performance of HYPER compared to other large-scale state-of-art hydrodynamic simulations like Magneticum, Illustris, etc, by replacing the ICM pressure model adopted in this work with a simulated ICM pressure profile drawn from the corresponding hydrodynamic simulation. That would allow a direct comparison between HYPER and full hydro simulations, and would enable us to study further the reliability of our new HPM algorithm.

3.6 Supplemental Materials

3.6.1 HPM Variables Adjustment

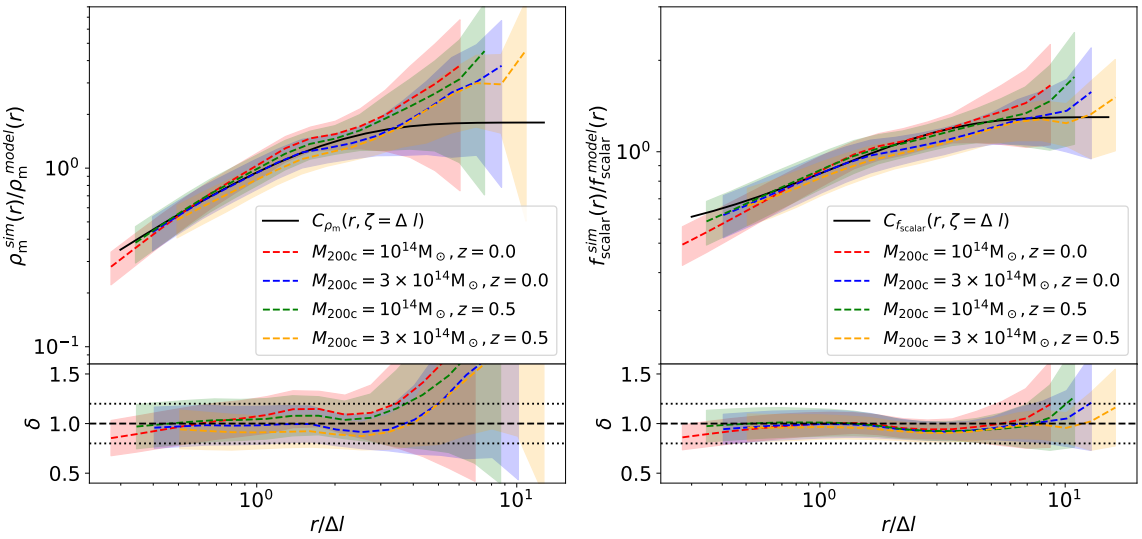

Figure 3.12: Ratio of simulated mass-weighted profiles of the HPM variables, $\rho_{\rm m}$ (left panel) and $f_{\rm scalar}$ (right panel), to the theoretical derivation in the ICM model for mass bins $M_{200c} = 10^{14}M_\odot$ and $3 \times 10^{14}M_\odot$ at redshift $z = 0$ and $z = 0.5$ (dashed colorful lines) and their uncertainties (thin bands). Also shown are the best fits for the calibration functions $C(r, \zeta)$ (solid black line). Fitted calibration functions are found to be in good agreement with the simulation results, while deviation appears at large radii where the uncertainties for the simulated radial profiles become great more significant and data points are less important in the fitting. The bottom panels show the ratio between the simulation results and the best fits for the calibration functions and the $\pm 20\%$ band (dotted black lines)

We adopt the form of the Weibull function for the calibration function $C(r, \zeta)$ to characterize the difference between the simulated radial profiles of HPM variables and their theoretical values in the ICM model:

$$C_Y(r, \zeta) = A_{\rm L}^C - (A_{\rm L}^C - A_{\rm H}^C) \exp[-(A_{\rm S}^C(r/\zeta))], \tag{3.54}$$

where Y denote the HPM variables ρ_m and $f_{\rm scalar}$ and $\zeta = \Delta l = L/N$ is the length of the grid cell in our simulation. We fit the calibration function to the ratio of the simulated mass-weighted profiles of $\rho_{\rm m}$ and $f_{\rm scalar}$ to the radial profiles derived in the standard ICM model for two mass bins $M_{200c} = 10^{14}{\rm M}_\odot, 3\times10^{14}{\rm M}_\odot$ at redshift $z = 0.0, 0.5$, and importance of the data points in fitting are weighted by the uncertainties of the radial profiles. The best fit results for the parameters $A^C_{\rm H}, A^C_{\rm L}, A^C_{\rm S}$ are [1.80,0.01,0.70] and [1.30,0.48,0.60] for HPM variables $\rho_{\rm m}$ and $f_{\rm scalar}$ respectively. These parameters of the calibration functions may be spatial resolution dependent.

In Figure 3.12 we plot the ratio of simulated radial profiles of $\rho_{\rm m}$ and $f_{\rm scalar}$ to their respective values in the adopted ICM model and its uncertainty. We also show the best fit results for our calibration function. The fitted calibration functions agree well with the simulated mean profiles in the inner regions of halos, but show more deviation as the uncertainties of the simulation results grow in the outskirt region.

3.6.2 Pressure Filtering and Artificial Viscosity Tuning

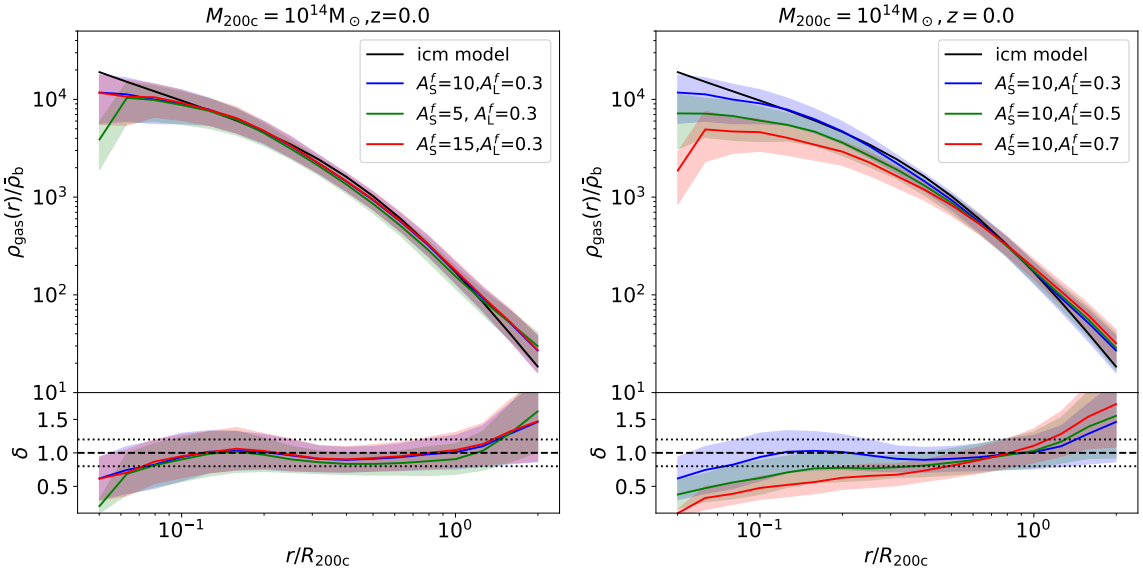

Figure 3.13: **Left:** Simulated gas density profiles as compared to the ICM model (solid black line) when we apply pressure filters with filter parameters set to $A^f_{\rm S} = 5$ (green), $A^f_{\rm S} = 10$ (blue), and $A^f_{\rm S} = 15$ (red). Simulation results for the gas density profiles are insensitive to the pressure filter parameter $A^f_{\rm S}$. Ratio between simulated gas density profile and the ICM model and the $\pm$ 20% region are shown in the bottom panel. **Right:** Simulated gas density profiles with filter parameters $A^f_{\rm L} = 0.3$ (blue), $A^f_{\rm L} = 0.5$ (green), and $A^f_{\rm L} = 0.7$ (red) compare to the ICM model (black).

As discussed in Section 3.3.6, we apply a pressure filter on the gas pressure field in Fourier space to smooth the gas pressure in the inner region of the halos and

suppress the numerical noise. The pressure filter is in the form of the Weibull function expressed by Eq. 3.42. We tune the parameters $A_{\rm L}$ and $A_{\rm S}$, which determine the scale range and the degree of smoothing at small scales for the pressure filter, to make the simulated gas density profiles match the ICM profiles.

In Figure 3.13 we compare the simulated gas density profiles with the analytical derivation in the ICM model after filtering the gas pressure field in Fourier space. We experiment with using the pressure filters with different combinations of $A_{\rm S}^f$ and $A_{\rm L}^f$. We find that the simulation results are less sensitive to the filter parameter $A_{\rm S}^f$, and we choose to adopt $A_{\rm S}^f = 10$ for our simulation. We tune the $A_{\rm L}^f$ starting from $A_{\rm L}^f = 1.0$ then gradually decrease to adjust the smoothing effect on the gas pressure imposed by the filter until we can balance the hydro force and the gravity and get a proper density profile when $A_{\rm L}^f = 0.3$.

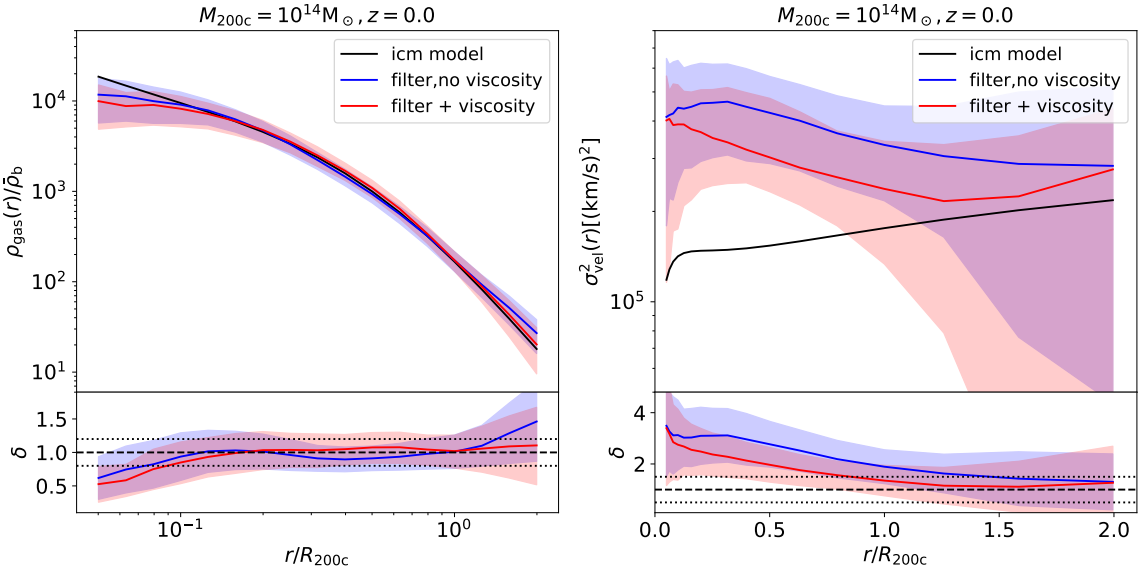

Figure 3.14: Simulated gas density profile (left) and gas velocity dispersion (right) and their uncertainties with both pressure filter and artificial viscosity applied in the simulation (red) as compared to the case with only the pressure filter being applied (blue). Both cases show good agreements with the ICM model (solid black line). Their ratio and the ± 20% (left), ± 50% (right) region (dotted black lines) are shown in the bottom panel.

However, with only the pressure filter, we can obtain a proper density profile but overestimate the velocity dispersion for gas particles in the simulated halos. By applying the artificial viscosity, which removes the extra kinetic energy of gas particles that should have been converted into heat, we can reduce the discrepancy, although not eliminate it completely. As shown in the right panel of Figure 3.13, smoothing the gas thermal pressure field avoids an excessive hydro force in the inner region of the simulated halos and prevents pushing too much gas out of the halo. We also

find that the artificial viscosity can effectively reduce the gas velocity dispersion and decreases the non-thermal pressure. Since both pressure filter and artificial viscosity can mitigate the gas pressure to balance the hydro force and gravity, we can tune the pressure filter and the artificial viscosity jointly to keep the simulated gas density profile matching the model derivation and reduce the gas velocity dispersion at the same time. In this case, we find the pressure filter with slightly larger $A_{\rm L}^f$ that $A_{\rm L}^f = 0.5$ and $\alpha \sim 0.1, \beta \sim 0.05$ for the parameters of artificial viscosity in Eq. 3.40 work best for our simulation.

In Figure 3.14 we plot the ICM gas profiles with (a) both pressure filter and artificial viscosity and (b) the pressure filter only. We show that by tuning the pressure filtering and the artificial viscosity jointly, we can make the gas density profile match the ICM model and obtain a lower gas velocity dispersion in the halo outskirt region.

Even with the artificial viscosity included into our simulation, it is still difficult to match the gas velocity dispersion in the inner region of the simulated halos to the ICM model. This may be because the finite resolution of the HPM algorithm limits the ability to accurately resolve the local artificial viscosity exerted on the gas particles in our simulation, especially in the high-density halo center region where hundreds even thousands of particles can co-locate in one grid cell. Further studies are required to explore the reason for the discrepancy and improve the simulation fidelity. One possible solution to increase the resolution in high-density regions is to use the adaptive mesh refinement.

Chapter 4

Templates for Sunyaev-Zel'dovich Angular Power Spectrum with HYPER

4.1 Introduction

The Sunyaev-Zel'dovich (SZ) effect imprinted in maps of the cosmic microwave background (CMB) is a promising probe of the evolution of large-scale structures. CMB photons are scattered by energetic electrons in the intracluster medium and intergalactic medium when passing through the expanding universe, which provides the most substantial contribution to temperature anisotropies on arcminute scales. Most recent CMB experiments have achieved unprecedented sensitivity and resolution to observe the temperature anisotropies in order of $\sim 10\mu$K noise and arcminute beams. Measurements of the secondary distortions caused by the SZ effect can be used to study the growth of structure and probe the epoch of reionization.

Different research has been conducted with the measurements of SZ signal includes direct detection of galaxy clusters, the autocorrelation of temperature fluctuations, and cross-correlation with large-scale structure from galaxy surveys. In this chapter, I mainly focus on an interesting statistic, the SZ angular power spectrum, whose amplitude depends strongly on the cosmological parameter σ_8, which describes the present root-mean-square matter fluctuation averaged over a sphere of radius $8h^{-1}$Mpc. If assuming the SZ power scales as $C_\ell \propto (\sigma_8/0.8)^\alpha$, theoretical calculations find the effective scaling index $\alpha_{\rm tSZ} \gtrsim 7$ (e.g. Seljak et al., 2001; Komatsu & Seljak, 2002) for the thermal SZ (tSZ) component and $\alpha_{\rm kSZ} \gtrsim 4$ (e.g. Vishniac, 1987) for the kinetic SZ (kSZ) component. Trac et al. (2011) model the SZ effect by post-processing a dark matter simulation of the large-scale structure of the universe to include gas in dark matter halos and the filamentary intergalactic medium (IGM), and find $7 \lesssim \alpha_{\rm tSZ} \lesssim 9$, $4.5 \lesssim \alpha_{\rm kSZ} \lesssim 5.5$. Thus, even a measurement with uncertainty up to a factor of two will result in a better than 15% determination of σ_8.

Currently, two publicly available sets of templates for the frequency-dependent SZ angular power spectrum have been widely used in the analyses of the SZ surveys. Komatsu & Seljak (2002) calculate the angular power spectrum of the SZ effect using an analytical halo model assuming the gas has a polytropic equation of state and is in hydrostatic equilibrium with an NFW gravitational potential. This template finds the angular power spectrum scales with the cosmological parameters σ_8 and $\Omega_{\rm b}$ as $C_\ell \propto \sigma_8^7(\Omega_{\rm b}h)^2$. Another template is proposed by Trac et al. (2011) constructing SZ maps for an octant of the sky by tracing through a dark matter simulation processed to include gas in dark matter halos and the filamentary IGM. This template have been used by Atacama Cosmology Telescope (ACT) and South Pole Telescope (SPT) groups to constrain cosmological parameter σ_8 (e.g. Lueker et al., 2010; Fowler et al., 2010; Dunkley et al., 2011,).

However, the template proposed by Komatsu & Seljak (2002) only accounts for the thermal but not kinetic contributions to the temperature anisotropies. The Sehgal et al. (2010) template approximates the gas physics in collapsed halos and the filamentary IGM by tracing through a dark matter simulation, which may not be accurate and flexible enough to model the gas properties and evolution in collapsed objects. As discussed in Trac et al. (2011), to constrain the reionization epoch through the kSZ angular power spectrum, we need a better understanding of the nonlinear contribution from collapsed objects in the post-reionization epoch. The HYPER code that has been discussed in Chapter 3 can be used to model both the thermal and kinetic contributions to the temperature anisotropies. HYPER also solves the gas equations of motion using robust thermodynamical models and more properly approximate the gas evolution in both the lower-density intergalactic medium and the higher-density intracluster medium. Thus, HYPER can be a perfect candidate for the templates calculating the SZ angular power spectrum.

In this chapter, I will discuss using the outputs of HYPER simulations to calculate the frequency-dependent SZ temperature anisotropies, with thermal and kinetic contributions in Section 4.2, study how the amplitude of the SZ angular power spectrum scales with the cosmological parameter σ_8 in Section 4.3. In Section 4.4, I will conclude our finds and discuss the future avenue.

4.2 Sunyaev-Zel'dovich Angular Power Spectrum

In this section, I will introduce how to use the simulation output of HYPER to calculate the tSZ and kSZ angular power spectra. For the calculation, I compare two different methods for both. For the tSZ and kSZ temperature anisotropies in the non-relativistic limit, the change in the CMB temperature at frequency ν in the direction $\hat{n}$ on the sky is expressed as

$$\frac{\Delta T_{\rm SZ}(\hat{n})}{T_{\rm CMB}} = \frac{\Delta T_{\rm tSZ}(\hat{n})}{T_{\rm CMB}} + \frac{\Delta T_{\rm kSZ}(\hat{n})}{T_{\rm CMB}} = f(\nu)y - b \tag{4.1}$$

where y is the dimensionless Compton parameter

$$y = \frac{k_{\rm B}\sigma_{\rm T}}{m_{\rm e}c^2}\int n_{\rm e}T_{\rm e}{\rm d}l, \tag{4.2}$$

and b is the Doppler parameter

$$b = \frac{\sigma_{\rm T}}{c}\int n_{\rm e}v_{\rm los}{\rm d}l, \tag{4.3}$$

$n_{\rm e}$, $T_{\rm e}$ are the number density and temperature of the electron distribution, $v_{\rm los}$ is the electron velocity along the line of sight and we choose the convention $v_{\rm los} > 0$ when the electrons are moving away from the observer. $f(\nu)$ is the frequency dependence term $f(\nu) = x_\nu \coth(x_\nu/2) - 4$ with $x_\nu = h\nu/(k_{\rm B}T_{\rm CMB})$. The temperature anisotropies is decomposed into harmonic components by

$$\frac{\Delta T(\hat{n})}{T_{\rm CMB}} = \sum_{\ell,m} a_{\ell m}Y_{\ell m}(\hat{n}). \tag{4.4}$$

The angular power spectrum is then defined as

$$C_\ell = \frac{1}{2\ell+1}\sum_{m=-\ell}^{\ell}\langle a_{\ell m}a^*_{\ell m}\rangle. \tag{4.5}$$

In this section, I use the HEALPix[1] scheme to integrate the electron pressure and momentum along the line of sight for pixelation of full-sky map of the tSZ and kSZ signal, then calculate the angular power spectra of the temperature anisotropies directly from the simulated maps using the software `healpy`[2]. In the Limber approximation, we can also relate the tSZ and kSZ angular power spectra to the 3D electron pressure power spectrum and electron momentum spectrum (e.g. Shao et al., 2011; Park et al., 2013). The simulation outputs we use for calculating the SZ angular power spectra are generated by the HYPER simulation with per side length of simulation box $L = 500h^{-1}$Mpc with periodic boundary conditions and equal numbers of dark matter and gas particles $N_{\rm dm} = N_{\rm gas} = 1024^3$, and the mesh size is set to be $N_{\rm mesh} = 4096^3$. The simulation runs from start point $z = 100$ to $z = 0$, while the hydro part for gas particle is turned on at $z = 6$ and adopt the DPP model (He et al., 2021a) for resolving the hydrodynamics of the simulation. A "concordance" ΛCDM model ($\Omega_{\rm m} = 0.3$, $\Omega_\Lambda = 0.7$, $\Omega_{\rm b} = 0.045$, $h = 0.7$ and $\sigma_8 = 0.8$) is adopted for the simulation. More details are described in Chapter 3.

[1] `https://healpix.sourceforge.io`

[2] `https://healpy.readthedocs.io/en/latest/index.html`

4.2.1 tSZ Angular Power Spectrum

We make full-sky maps of the tSZ effect in Healpix format with a pixel resolution of 0.4 arcmins (Nside = 8192). For the spherical shell that represents the full-sky map, particles are subdivided by angular coordinates using the HEALPix scheme for pixelation of a sphere. The projected electron pressure in each pixel of the shell is computed and saved. Then the angular power spectrum of the tSZ effect can be directly calculated from the sky maps using `healpy`. We also calculate the tSZ angular power spectrum with the 3D electron pressure power spectrum by

$$C_\ell^{\rm tSZ} = \frac{16 f^2(\nu)\pi^2}{(2\ell+1)^3} \int \Delta_{\rm tSZ}(k,z)|_{k=\ell/\chi} \chi(z) d\chi(z), \tag{4.6}$$

where $\chi(z)$ is the comoving distance to redshift z, and

$$\Delta_{\rm tSZ}(k,z) = \left[\frac{\langle P_{\rm e}(z)\rangle \sigma_{\rm T}}{(1+z) m_{\rm e} c^2}\right]^2 \frac{k^3}{2\pi^2} P_p(k,z). \tag{4.7}$$

Here $P_p(k,z) = \langle \delta_P(\vec{k},z) \delta_P^*(\vec{k},z)\rangle$ is the power spectrum of the Fourier transform $\delta_P(\vec{k},z)$ of the fractional thermal pressure fluctuations $\delta_P(\vec{x},z) \equiv P_{\rm e}(\vec{x},z)/\langle P_{\rm e}(\vec{x},z)\rangle - 1$. The $P_p(k,z)$ can be evaluated with output snapshots of HYPER simulation at different redshifts.

In Figure 4.1, I compare two different methods for calculating the tSZ angular power spectrum, results directly calculated from the full-sky map and calculated with the 3D power spectrum of electron pressure field of $0 \leq z \leq 1$ are found in excellent agreement for $\ell \gtrsim 1000$. We find extra power for the tSZ angular power spectrum calculated from the HEALPix map and disagrees with the Plank analysis (Planck Collaboration et al., 2016a) at $\ell \lesssim 500$. The tSZ angular power spectrum calculated with the spectrum of electron pressure field agrees very well with the Planck data, either integrated from $z = 0$ to $z = 1$ or to $z = 5$. We find the contribution from the tSZ signal of $z > 1$ to the total thermal power begins to increase at $\ell \gtrsim 3000$ and become more significant at $\ell \sim 8000$. Our calculation still shows a significant tension with ACT (Choi et al., 2020) and SPT (George et al., 2015; Reichardt et al., 2021) data at $\ell = 3000$.

The extra power found in the tSZ angular power spectrum calculation is due to replicating and stacking the simulation box based on periodic boundary conditions when constructing the light cone for the full-sky map following HEALPix format. Blaizot et al. (2005) suggests random transformations (e.g. shift, rotation, inversion) of the underlying simulation box could help in this situation. We find the tSZ signal at $z < 1$ contribute ∼80% of the total thermal power at $\ell = 3000$. This is because large fractions of the power at this scale come from massive halos, which are rare at high redshift. A more significant contribution from $z > 1$ at high multiples $\ell \sim 8000$ shows angular power of small scale is more sensitive to the high redshift clusters. The tension we find between the tSZ angular power spectrum calculated with the products

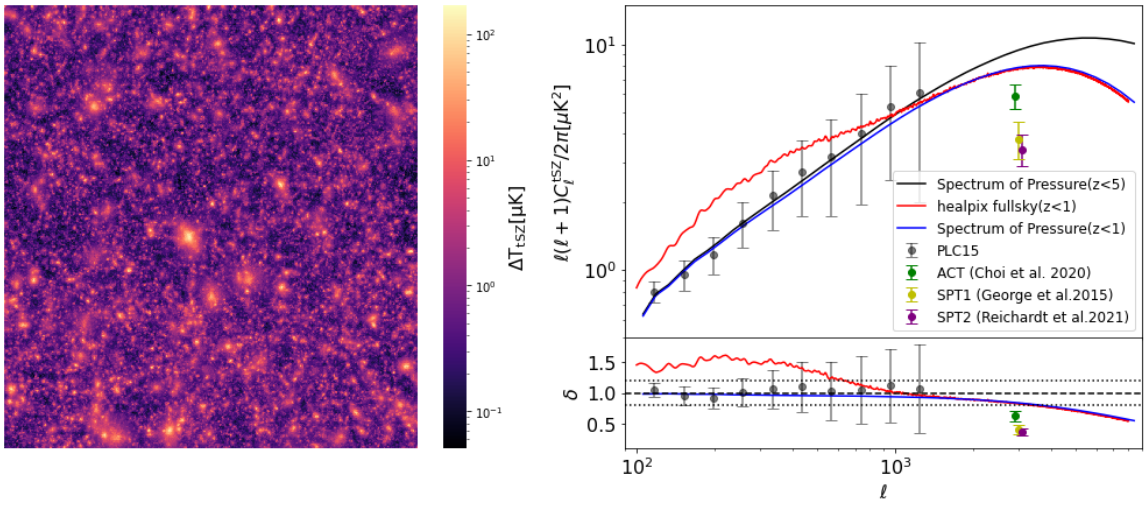

Figure 4.1: **Left**: the tSZ temperature anisotropies in μK at 280 GHz for a $4^\circ \times 4^\circ$ sample field from the full-sky map. The map is generated by HEALPix using HYPER simulation output integrated from $z = 0.0$ to $z = 1.0$. At this frequency, the tSZ signal appears as a temperature increment. The region where temperature anisotropy $\gtrsim 100\mu$K could sit a massive galaxy cluster. **Right**: tSZ angular power spectra for $0 \leq z \leq 1$ calculated with two different methods are compared. Spectrum calculated from the full-sky map by `healpy` (red) is in excellent agreement with that calculated with the spectrum of pressure (blue) for $\ell \gtrsim 1000$. The excess power shows up for the tSZ angular power spectrum calculated from the full-sky map at low ℓ due to the light cone is constructed by replicating and stacking from the periodic simulation box. The tSZ angular power spectrum calculated with the power spectrum of electron pressure integrated to $z = 5$ is plotted (black), which accounts for most of the total tSZ power for the scales of interest. Planck 2015 analysis of the tSZ power spectrum (gray dots with error bar), ACT (green dot with error bar) and SPT (yellow and purple dots with error bars) values correspond to $\ell = 3000$ are also shown for comparison. ACT and SPT data are shifted in the plot for clarity. All tSZ data are rescaled to 280 GHz for direct comparison. In the bottom panel, the ratios of different calculations and observations to the tSZ angular power spectrum integrated to $z = 5$ are plotted. The $\pm$ 20% region is also shown (dotted lines).

of HYPER simulation and ACT, SPT data may result from two causes. One possible reason is that ACT and SPT observations only adopt a limited number of frequency bands. The tSZ angular power spectrum extracted from the mixed component signal (e.g. kSZ, clustered CIB, radio point sources, infrared point sources, etc.) could be under-constrained. The ICM pressure model, DPP, we adopt for HYPER simulation is studied using X-ray observation and hydrodynamical simulation at low redshift ($z < 0.2$). Calibration of the theoretical pressure profiles using a fair sample of clusters and groups out to higher redshift could potentially lower the tension between our calculation of the tSZ power spectrum and high-multipole observations.

4.2.2 kSZ Angular Power Spectrum

The sky maps of the kSZ effect can also be generated in HEALPix format by projecting the component of the electron momentum along the line of sight to each pixel of the full-sky spherical shell, and the kSZ angular power spectrum is calculated from the sky maps with `healpy`. If define the electron momentum field of the ionized medium by

$$\mathbf{q}(\vec{x}, z) \equiv (1 + \delta(\vec{x}, z))\vec{v}, \tag{4.8}$$

where $\delta(\vec{x}, z) = n_{\rm e}(\vec{x}, z)/\langle n_{\rm e}(z)\rangle - 1$. We can also calculate the kSZ angular power spectrum with the 3D electron momentum power spectrum by

$$C_\ell^{\rm kSZ} = \frac{8\pi^2}{(2\ell+1)^3}\int \Delta_{\rm kSZ}(k, z)|_{k=\ell/\chi}\chi(z)d\chi(z), \tag{4.9}$$

and

$$\Delta_{\rm kSZ}(k, z) = \left[\frac{\langle n_{\rm e}(z)\rangle\sigma_{\rm T}}{(1+z)m_{\rm e}c^2}\right]^2 \frac{k^3}{2\pi^2}P_{q_\perp}(k, z). \tag{4.10}$$

Here $P_{q_\perp}(k, z) = \langle\tilde{\mathbf{q}}_\perp(\vec{k}, z)\tilde{\mathbf{q}}_\perp^*(\vec{k}, z)\rangle$, $\tilde{\mathbf{q}}_\perp(\vec{k}, z)$ is the the projection of $\tilde{\mathbf{q}}(\vec{k}, z) \equiv \int e^{i\vec{k}\cdot\vec{x}}\mathbf{q}(\vec{x}, z)\mathrm{d}^3\vec{x}$ on the plane perpendicular to the mode vector $\vec{k}$ that $\tilde{\mathbf{q}}_\perp(\vec{k}, z) = \tilde{\mathbf{q}}(\vec{k}, z) - \hat{k}[\tilde{\mathbf{q}}(\vec{k}, z)\cdot\hat{k}]$. Similar to the calculation of the tSZ angular power spectrum, we can evaluate the $\tilde{\mathbf{q}}_\perp(\vec{k}, z)$ with output snapshots of HYPER simulation at different redshifts to calculate the kSZ angular power spectrum.

In Figure 4.2, I compare two different methods for calculating the kSZ angular power spectrum, results calculated from the full-sky map and calculated with the 3D power spectrum of electron momentum field of $0 \leq z \leq 1$ are found in excellent agreement for $\ell \gtrsim 1000$. Extra power is also found for the kSZ angular power spectrum calculated from the HEALPix map due to replicating and stacking periodic simulation boxes without random rotations. We find that the contribution from the kSZ signal of $z > 1$ is more significant than the tSZ signal. The values for kSZ power at $\ell = 3000$ from ACT (Sievers et al., 2013) and SPT (George et al., 2015; Reichardt et al., 2021) analysis is also plotted for comparison.

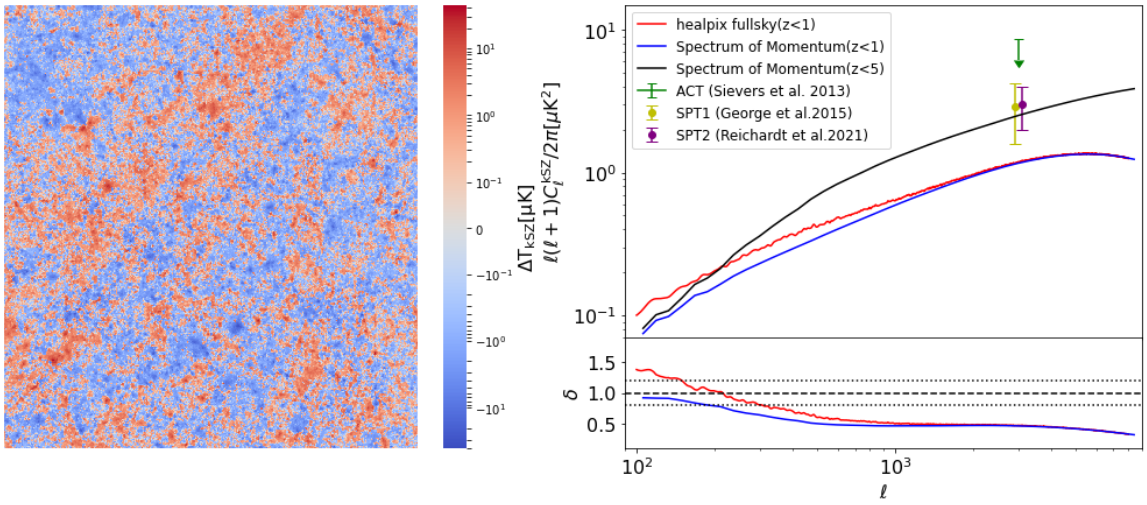

Figure 4.2: **Left**: the kSZ temperature anisotropies in μK for a $4^\circ \times 4^\circ$ sample field from the full-sky map. The map is generated by HEALPix using HYPER simulation output integrated from $z = 0.0$ to $z = 1.0$. The kSZ signal is a temperature decrement (increment) if the los peculiar velocity is positive (negative). The temperature anisotropy $\ll 100\mu$K is about an order-of-magnitude smaller than the tSZ signal at 280 GHz. **Right**: kSZ angular power spectra for $0 \leq z \leq 1$ calculated with two different methods are compared. Spectrum calculated from the full-sky map by `healpy` (red) is in excellent agreement with that calculated with the spectrum of momentum (blue) for $\ell \gtrsim 1000$. The excess power shows up for the kSZ angular power spectrum calculated from the full-sky map at low ℓ is also due to replicating and stacking of the periodic simulation box when constructing the light cone. The kSZ angular power spectrum calculated with the power spectrum of electron momentum integrated to $z = 5$ is plotted (black), which accounts for the contribution to the kSZ power in the post-reionization epoch. ACT (green arrow) and SPT (yellow and purple dots with error bars) analysis of the kSZ power spectrum correspond to $\ell = 3000$ are also shown for comparison. ACT and SPT data are shifted in the plot for clarity. In the bottom panel, the ratios of different calculations and observations to the kSZ angular power spectrum integrated to $z = 5$ are plotted. The $\pm$ 20% region is also shown (dotted lines).

The kSZ angular power spectrum amplitude is found several times smaller than the tSZ angular power spectrum at 280 GHz. This is not surprising since the temperature anisotropies of the kSZ effect is also found much less than the tSZ signal. The replica effect also introduces the excess power in the kSZ signal at low ℓ. In Sehgal et al. (2010), a simple filter is chosen to suppress the large-scale excess. We find the kSZ signal at $z < 1$ contributes $\gtrsim$50% of the kinetic power at $\ell = 3000$. This difference compared to what we find in tSZ angular power spectrum is due to the kSZ signal from the low-mass halos and the IGM are relatively more important, and the majority of the kSZ signal is from the high-redshift universe. We also emphasize here that the kSZ angular power spectrum calculated with the outputs of HYPER simulation only accounts for the contribution from the post-reionization epoch. Our results need to be combined with the contribution from the reionization epoch when compare to the observation data to provide enough information for constraints of cosmological parameters and the reionization epoch.

4.3 Dependence on cosmological parameter σ_8

In order to place constraints on σ_8, we first need to study how tSZ, kSZ, SZ angular power spectra scale with this cosmological parameter. In Trac et al. (2011), a rescaling method is adopted to avoid running additional simulations. Analytical models for contribution from halo terms and IGM terms are used to rescale the angular power spectrum to arbitrary σ_8. However, HYPER code is very efficient and allows us to run different realizations with σ_8 being varied. For both tSZ and kSZ angular power spectra calculation, we vary the σ_8 from 0.6 to 1.

Following Trac et al. (2011), we define a scaling amplitude $A_{\rm q}$ (q = SZ, tSZ, kSZ), expressed as

$$A_{\rm q} = \frac{C_\ell^{\rm q}(\ell, \sigma_8)}{C_\ell^{\rm q}(\ell, \sigma_8 = 0.8)} = (\frac{\sigma_8}{0.8})^{\alpha_{\rm q}} \tag{4.11}$$

to quantify how the SZ templates scale with σ_8. For scaling index $\alpha_{\rm q}$, it can be calculated through

$$\alpha_{\rm q} = \frac{{\rm d}\ {\rm ln}A_{\rm q}}{{\rm d}\ {\rm ln}s}, \tag{4.12}$$

where $s = \sigma/0.8$. Using the outputs of HYPER simulations realized with different σ_8 range from 0.6 to 1.0, we find $7.5 \lesssim \alpha_{\rm tSZ} \lesssim 8.5$ for $0.6 \leq \sigma \leq 1.0$ at $\ell = 3000$ which is consistent with the result $\alpha_{\rm tSZ} \gtrsim 7$ obtained by Komatsu & Seljak (2002) and $7 \lesssim \alpha_{\rm tSZ} \lesssim 9$ by Trac et al. (2011). For the kSZ component, we find $4.5 \lesssim \alpha_{\rm kSZ} \lesssim 5.0$ which also agrees well with the result in Trac et al. (2011) that $4.5 \lesssim \alpha_{\rm kSZ} \lesssim 5.5$. The $\alpha_{\rm kSZ}$ we find is much smaller than the tSZ scaling index. Considering the kSZ power has both linear and nonlinear component contributions and the linear-regime scale factor for kSZ follows $r_{\rm kSZ} = (\sigma_8/0.8)^4$ (Vishniac, 1987) in an approximation based on linear perturbation theory that the fluctuation of the peculiar velocity field

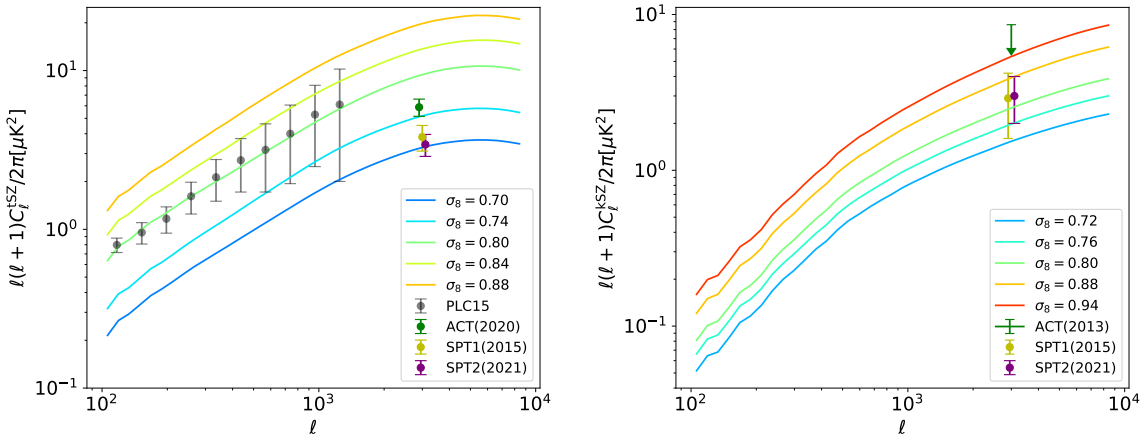

Figure 4.3: **Left**: tSZ angular power spectra calculated with the 3D power spectrum of electron pressure field produced by HYPER simulations when adopting different values of cosmological parameter σ_8 for the simulations (colorful solid lines). Planck 2015 analysis of the tSZ power spectrum (gray dots with error bars), ACT (green arrow) and SPT (yellow and purple dots with error bars) values correspond to $\ell = 3000$ are also shown. All the tSZ data are rescaled to 280 GHz for direct comparison. **Right**: kSZ angular power spectra calculated using the 3D power spectrum of electron momentum field of HYPER outputs when set different σ_8 values for the simulations (colorful solid lines). ACT (green arrow) and SPT (yellow and purple dots with error bars) values correspond to $\ell = 3000$ are plotted for comparison. ACT and SPT data are shifted in the plot for clarity.

is related to the linear matter power spectrum as $P_{vv}(k) \propto P_{\delta\delta}^{\rm lin}(k) \propto \sigma_8^2$. The weak variation with σ_8 for $\alpha_{\rm kSZ}$ is due to the linear component is generally more dominant in the kSZ signal.

In order to study how the amplitude of the total SZ angular power spectrum scale with σ_8, we model the total SZ power in the nonrelativistic limit by

$$C_\ell^{\rm SZ} = C_\ell^{\rm tSZ}(\nu) + C_\ell^{\rm kSZ}. \tag{4.13}$$

By combining the results for the calculation of the tSZ and kSZ angular power spectra, we find $7 \lesssim \alpha_{\rm SZ} \lesssim 7.5$ at 280 GHz and $\ell = 3000$, which is in good agreement with the SZ scaling index $6.5 \lesssim \alpha_{\rm SZ} \lesssim 8$ found in Trac et al. (2011). We notice that the scaling indices $\alpha_{\rm q}$ we calculate with the HYPER simulation outputs span a narrower range than the results in Trac et al. (2011). This is because they adopt four different halo gas models while HYPER only uses a fixed ICM pressure model.

In Figure 4.3, we show how our calculation of tSZ and kSZ angular power spectrum using the output of HYPER simulations vary with the cosmological parameter σ_8. In the figure, we only plot the results of certain σ_8 values that are comparable to the

observation data. For the angular power spectrum, we plot Planck analysis (Planck Collaboration et al., 2016a) for $\ell \lesssim 1300$ which favors $\sigma_8 \simeq 0.8$. We also plot ACT (Choi et al., 2020) and SPT (George et al., 2015; Reichardt et al., 2021) values at $\ell = 3000$ which yields $\sigma_8 \sim 0.75$ and $\sigma_8 \sim 0.70$ respectively. The kSZ angular power spectra we show in the figure only accounts for the contribution from the post-reionization epoch, the ACT (Sievers et al., 2013) and SPT (George et al., 2015; Reichardt et al., 2021) analysis of kSZ signal plotted here are more proper to be viewed as upper limits for our calculation.

We then consider a simplified case where we constrain the cosmological parameter σ_8 from the SZ or tSZ angular power alone. For $C_\ell^{\rm SZ} = 5.6 \pm 2.0\ \mu{\rm K}^2$ at $\ell = 3000$ converted to 280 GHz reported by Lueker et al. (2010) and SZ power of $6.8 \pm 2.9\ \mu{\rm K}^2$ reported by Dunkley et al. (2011), our template with HYPER simulation implemented using the DPP model yields $\sigma_8 = 0.72^{+0.03}_{-0.04}$ and $\sigma_8 = 0.74^{+0.04}_{-0.06}$ respectively. Our results on σ_8 using the SZ angular power reported in Dunkley et al. (2011) agree well with their constraints of σ_8 on SZ emission when using different templates TBO1 (Sehgal et al., 2010) $\sigma_8 = 0.74 \pm 0.05$, TBO2 (Trac et al., 2011) $\sigma_8 = 0.78 \pm 0.05$, Battaglia (Battaglia et al., 2010) $\sigma_8 = 0.77 \pm 0.05$, and Shaw (Shaw et al., 2010) $\sigma_8 = 0.77 \pm 0.05$. For tSZ angular power values at $\ell = 3000$ scaled to 280 GHz, we use data reported by ACT that $C_\ell^{\rm tSZ} = 5.88 \pm 0.73\ \mu{\rm K}^2$ (Choi et al., 2020) and by SPT that $C_\ell^{\rm tSZ} = 3.81^{+0.54}_{-0.73}\ \mu{\rm K}^2$ from George et al. (2015) and $3.20 \pm 0.50\ \mu{\rm K}^2$ from Reichardt et al. (2021). Our calculation with HYPER simulations favor $\sigma_8 = 0.75 \pm 0.01$ for ACT data and $\sigma_8 = 0.71^{+0.01}_{-0.02}, 0.70^{+0.01}_{-0.02}$ for SPT data. However, the Planck analysis of the tSZ power spectrum seems to favor a higher value $\simeq 0.80$ for σ_8. We see tension appears among Planck, ACT, and SPT observation data. Studies of the pressure profiles of galaxy clusters at higher redshift and future observation measuring SZ angular power spectrum at high multipoles could help to mitigate this tension we find for different observations.

4.4 Discussion and Conclusions

This chapter introduces a template for calculating the tSZ and kSZ angular power spectra with HYPER, an innovative HPM code for efficient and rapid simulation for the gas in dark matter halos and the filamentary IGM. The template we proposed can be applied to interpret observation data for future SZ surveys. Our template for the kSZ angular power spectrum can also be combined with the work modeling kSZ signal during the period of reionization to constrain cosmological parameters and the reionization epoch.

We take two different methods for the calculation of tSZ and kSZ angular power spectra. We adopt standard HEALPix format for the simulated maps, where integration about electron pressure and momentum along the line of sight are conducted for pixelization of the full-sky maps of tSZ and kSZ signal. Angular power spectra can be directly calculated from the maps generated by HYPER simulations. Adopting

the Limber approximation, we also calculate the tSZ and kSZ angular power spectra with the 3D power spectrum of electron pressure and momentum fields produced by HYPER simulations. Angular power spectra calculated using HEALPix maps and 3D power spectra produced by HYPER simulations are in excellent agreement for $\ell \gtrsim 1000$. We find extra power in the spectra calculated using the generated full-sky map in HEALPix format at low multipole due to replicating and stacking of the periodic simulation box when constructing the light cone. We see more contribution from low redshift to the total power for tSZ signal than kSZ signal, which is because large fractions of the tSZ power come from massive halos while the low-mass halos and the IGM are relatively more important to the kSZ signal.

We also calculate the dependence of the angular power spectra on cosmological parameter σ_8. HYPER is very efficient and allows us to run different realizations while varying σ_8 values. We study how tSZ, kSZ, SZ angular power spectra scale with σ_8 when assuming a power-law scaling relation $C_\ell \propto (\sigma_8/0.8)^\alpha$. Our findings for the scaling index α for tSZ, kSZ, and total SZ angular power spectra at $\ell = 3000$ are all in good agreement with the results in Trac et al. (2011). We find a weaker variation with σ_8 for kSZ angular power at $\ell = 3000$ because the linear component is generally more dominant in the kSZ signal.

We compare our calculation to the up-to-date observations and discuss a simplified case where we constrain the cosmological parameter σ_8 from the SZ or tSZ angular power alone. We find significant tension among Planck, ACT, and SPT observation data. We may require more robust studies of ICM pressure profiles at higher redshift and analysis from future SZ surveys with higher resolution and more frequency bands to mitigate this tension.

Many avenues remain for future work on completing the template we proposed for the SZ angular power spectrum. Our calculation of tSZ and kSZ angular power spectra using the HEALPix maps generated with HYPER simulations find extra power at $\ell \lesssim 1000$. We need to explore different approaches to suppress this large-scale excess. Methods like simple filtering (Sehgal et al., 2010) and random transformations (Blaizot et al., 2005) have been discussed could be the potential solutions. We could also increase the volume of our simulation box though this would make our template more computationally expensive. We also plan to adopt an ICM pressure model derived using a fair sample of clusters and groups out to higher redshift in our HYPER simulations, which may mitigate the tension between our calculation and the analysis of SZ angular power spectrum at high multipole in current SZ surveys.

Chapter 5

Conclusions and Future Work

This dissertation introduces a hydro-particle-mesh (HPM) code for efficient and rapid simulations (HYPER) of gas and dark matter. HYPER simulations are orders of magnitude faster than expensive hydrodynamic simulations and allow one to systematically vary the models for intracluster medium (ICM) and intergalactic medium (IGM) to study different baryonic physics and effects. HYPER simulations can also produce lightcone catalogs of dark matter halos and full-sky tomographic maps of the lensing convergence, Sunyaev-Zel'dovich (SZ) effect, and X-ray emission, which are useful for testing data analysis pipelines, generating training data for machine learning, understanding selection and systematic effects, and for interpreting astrophysical and cosmological constraints. For the science application of HYPER simulation, I propose a template for calculating the thermal SZ (tSZ) and kinetic SZ (kSZ) angular power spectra whose amplitudes are very sensitive to the cosmological parameters σ_8 and the latter one can also be used to constrain the epoch of reionization.

For the HPM algorithm of HYPER, dark matter halo model, ICM pressure profile, and IGM temperature-density relation are crucial for achieving high efficiency and high fidelity for the approximate hydrodynamics solver in both the IGM and the ICM regime, which together fill most of the spatial volume in a fast hydro simulation. Chapter 2 focuses on the study of ICM pressure profile, where I thoroughly discuss our updated analytical model for gas pressure profile of galaxy clusters by combining results from X-ray observations with cosmological simulations. In this work, we adjust the universal galaxy cluster pressure profile (UPP) (Arnaud et al., 2010) modeled on the X-ray measurements for the hydrostatic mass bias. Hydrostatic mass bias is mainly caused by neglecting the existence of non-thermal pressure in X-ray observations and has long been treated as a constant when being used to interpret observation data and constrain cosmological parameters (e.g. Planck Collaboration et al., 2014b; Bolliet et al., 2018). However, the possibility of hydrostatic bias could depend on cluster mass has been proposed and discussed recently. In Chapter 2, we presented a simulation-based model to characterize the relation between the "true" masses and the X-ray-estimated hydrostatic masses of galaxy clusters using the X-ray

masses measured from synthetic images of simulated clusters drawn from the IllustrisTNG, the BAHAMAS, and the MACSIS simulations. We apply this model to the REXCESS X-ray cluster sample and find X-ray-measured hydrostatic masses underestimate masses of the clusters in the REXCESS sample by around 7% on average. We show that the bias has a significant mass dependence increasing with mass from $\approx 0\%$ at $M_{500c}^{\mathrm{X-ray}} = 10^{14} M_{\odot}$ to $\approx 15\%$ at $M_{500c}^{\mathrm{X-ray}} = 10^{15} M_{\odot}$. We recalibrate the scaled pressure profiles of each cluster in the REXCESS sample used to construct the UPP model and propose an updated pressure model, debiased galaxy cluster pressure profile (DPP). Our DPP model is found 5% lower than the UPP model in the inner region of the clusters and 15% lower at the outskirt. Standard self-similarity still stands for the scaling relation of the DPP model and the $Y - M$ relation. The analytical calculation of the tSZ angular power spectrum derived from DPP is consistent with the analysis of Planck thermal SZ survey data without requiring extreme cosmological parameters.

We adopt the DPP model for the ICM pressure profile used to implement the HPM algorithm in HYPER code introduced in detail in Chapter 3. HYPER applies a power-law density-temperature relation for the gas in the IGM regime of low-density. For the high-density ICM regime, we construct a mapping relation between two designed HPM variables and the gas temperature and pressure based on the adopted ICM gas pressure model to simulate the evolution of baryonic matter efficiently. We show that the HYPER simulation results are in good agreement with the halo model expectations for the density, temperature, and pressure radial profiles. Simulated galaxy cluster scaling relations for SZ and X-ray observables are also in good agreement with mean predictions, with scatter comparable to that found in hydrodynamic simulations. The tSZ angular power spectrum measured for the HYPER simulation, which is calculated using the 3D power spectrum of the gas pressure drawn from the simulation at different redshift snapshots, is in good agreement with the analytical predictions evaluated with the halo model and the ICM model used to implement the HPM algorithm. Good consistency in the simulation output and ICM model derivation for properties of the ICM regime includes the cluster radial profiles, SZ and X-ray observable-mass relation, and statistical quantities of the tSZ effects indicate HYPER simulation allows us to systematically control the ICM physics by varying the ICM model implemented in the HPM mapping relation construction. We also envision some main use cases for HYPER: generating mock catalogs and creating maps of various physical quantities for galaxy clusters, producing training data for a multiband deep learning model, studying modifications of the matter power spectrum due to joint effects of baryonic physics and varied cosmological parameters, systematically studying how different gas physics influences the tSZ angular power spectrum, examining the gas physics implemented in the current state-of-art high-resolution hydrodynamic simulations, etc.

In Chapter 4, we discuss the application of HYPER simulation in SZ science. We introduce a template for calculating the tSZ and kSZ angular power spectra with

HYPER simulation products. We calculate the angular power spectra of tSZ and kSZ signals using two different methods: 1. generate simulated full-sky maps of tSZ and kSZ effects in standard HEALPix format. We integrate electron pressure and momentum along the line of sight for pixelization of the HEALPix maps, and angular power spectra can be directly calculated from the simulated maps. 2. adopt the Limber approximation and relate the tSZ and kSZ angular power spectra to he 3D power spectrum of electron pressure and momentum field produced by HYPER simulations. We find two methods lead to excellent agreement in tSZ and kSZ spectra calculation expect extra power is found in the spectra calculated from HEALPix maps due to the replica effect. We find more contribution from low redshift to the total power for tSZ signal than kSZ signal. This difference is caused by the different importance of the massive halos, low-mass halos, and IGM to tSZ and kSZ signals. We also run different realizations of HYPER varying the values of the cosmological parameter σ_8 to study the dependence of the angular power spectra on σ_8. Our calculation of the the scaling index α when assuming a power-law scaling relation $C_\ell \propto (\sigma_8/0.8)^\alpha$ is in good agreement with the results in Komatsu & Seljak (2002), Shaw et al. (2010) and Trac et al. (2011). We compare our calculation to the up-to-date observations and present a simplified case where we constrain the σ_8 form SZ angular power spectra.

For the future extension of this work, our study of the DPP model is restricted to the analysis of simulation results and observation data at low redshift. We need to explore the redshift dependence of hydrostatic mass bias and the ICM pressure model of galaxy clusters, which may help mitigate tension between the analytical calculation and observation data for the tSZ angular power spectrum. We will also focus on improving the finite spatial resolution of HYPER simulation. We consider adopting a hybrid scheme combining the multigrid method with the fast Fourier transform. This approach could eliminate the resolution effect in the high-density ICM regime and sustain the high computational efficiency throughout the rest of the simulation volume. Alleviation of the resolution effect may also help reduce the gas velocity dispersion in the inner region of halos. We plan to adopt simulated ICM pressure profiles drawn from large-scale state-of-art hydrodynamic simulations in HYPER, which allows a direct comparison with full hydro simulations and further examination of the reliability of our new HPM algorithm. We will keep consummating the template for SZ angular power spectrum with HYPER. We need to pursue proper methods for suppressing the large-scale excess in the angular power spectra calculated from HEALPix maps generated using HYPER outputs. We also envision that the kSZ angular power spectrum for the post-reionization epoch can be combined with the work modeling kSZ signal during the period of reionization to constrain cosmological parameters and the reionization epoch.

Bibliography

Allen, S. W., Evrard, A. E., & Mantz, A. B. 2011, , 49, 409, doi: 10.1146/annurev-astro-081710-102514

Allen, S. W., Schmidt, R. W., Fabian, A. C., & Ebeling, H. 2003, , 342, 287, doi: 10.1046/j.1365-8711.2003.06550.x

Angulo, R. E., Springel, V., White, S. D. M., et al. 2012, , 426, 2046, doi: 10.1111/j.1365-2966.2012.21830.x

Arnaud, M., Pointecouteau, E., & Pratt, G. W. 2007, , 474, L37, doi: 10.1051/0004-6361:20078541

Arnaud, M., Pratt, G. W., Piffaretti, R., et al. 2010, , 517, A92, doi: 10.1051/0004-6361/200913416

Barnes, D. J., Kay, S. T., Henson, M. A., et al. 2017, , 465, 213, doi: 10.1093/mnras/stw2722

Barnes, D. J., Vogelsberger, M., Pearce, F. A., et al. 2020, arXiv e-prints, arXiv:2001.11508. https://arxiv.org/abs/2001.11508

Barnes, J., & Hut, P. 1986, , 324, 446, doi: 10.1038/324446a0

Battaglia, N., Bond, J. R., Pfrommer, C., & Sievers, J. L. 2012, , 758, 74, doi: 10.1088/0004-637X/758/2/74

Battaglia, N., Bond, J. R., Pfrommer, C., & Sievers, J. L. 2012, The Astrophysical Journal, 758, 75. http://stacks.iop.org/0004-637X/758/i=2/a=75

Battaglia, N., Bond, J. R., Pfrommer, C., & Sievers, J. L. 2012, , 758, 75, doi: 10.1088/0004-637X/758/2/75

Battaglia, N., Bond, J. R., Pfrommer, C., Sievers, J. L., & Sijacki, D. 2010, , 725, 91, doi: 10.1088/0004-637X/725/1/91

Battaglia, N., Leauthaud, A., Miyatake, H., et al. 2016, Journal of Cosmology and Astroparticle Physics, 2016, 013, doi: 10.1088/1475-7516/2016/08/013

Bautz, M. W., Miller, E. D., Sanders, J. S., et al. 2009, , 61, 1117, doi: 10.1093/pasj/61.5.1117

Bernstein, J., & Dodelson, S. 1990, , 41, 354, doi: 10.1103/PhysRevD.41.354

Birkinshaw, M. 1999, , 310, 97, doi: 10.1016/S0370-1573(98)00080-5

Blaizot, J., Wadadekar, Y., Guiderdoni, B., et al. 2005, , 360, 159, doi: 10.1111/j.1365-2966.2005.09019.x

Bocquet, S., Saro, A., Dolag, K., & Mohr, J. J. 2016, , 456, 2361, doi: 10.1093/mnras/stv2657

Bode, P., & Ostriker, J. P. 2003, , 145, 1, doi: 10.1086/345538

Böhringer, H., Schuecker, P., Pratt, G. W., et al. 2007, , 469, 363, doi: 10.1051/0004-6361:20066740

Bolliet, B., Comis, B., Komatsu, E., & Macías-Pérez, J. F. 2018, , 477, 4957, doi: 10.1093/mnras/sty823

Bonamente, M., Joy, M. K., LaRoque, S. J., et al. 2006, , 647, 25, doi: 10.1086/505291

Boylan-Kolchin, M., Springel, V., White, S. D. M., Jenkins, A., & Lemson, G. 2009, , 398, 1150, doi: 10.1111/j.1365-2966.2009.15191.x

Brüggen, M., & Vazza, F. 2015, Astrophysics and Space Science Library, Vol. 407, Turbulence in the Intracluster Medium, ed. A. Lazarian, E. M. de Gouveia Dal Pino, & C. Melioli, 599, doi: 10.1007/978-3-662-44625-6_21

Bryan, G. L., & Norman, M. L. 1995, in American Astronomical Society Meeting Abstracts, Vol. 187, American Astronomical Society Meeting Abstracts, 95.04

Carlstrom, J. E., Holder, G. P., & Reese, E. D. 2002, , 40, 643, doi: 10.1146/annurev.astro.40.060401.093803

Chandrasekhar, S. 1950, Radiative transfer.

Choi, S. K., Hasselfield, M., Ho, S.-P. P., et al. 2020, , 2020, 045, doi: 10.1088/1475-7516/2020/12/045

Churazov, E., Forman, W., Vikhlinin, A., et al. 2008, , 388, 1062, doi: 10.1111/j.1365-2966.2008.13507.x

Cole, S., & Kaiser, N. 1988, , 233, 637, doi: 10.1093/mnras/233.3.637

Colella, P., & Woodward, P. R. 1984, Journal of Computational Physics, 54, 174, doi: 10.1016/0021-9991(84)90143-8

Croston, J. H., Pratt, G. W., Böhringer, H., et al. 2008, , 487, 431, doi: 10.1051/0004-6361:20079154

Da Silva, A. C., Kay, S. T., Liddle, A. R., & Thomas, P. A. 2004, Monthly Notices of the Royal Astronomical Society, 348, 1401, doi: 10.1111/j.1365-2966.2004.07463.x

Davé, R., Anglés-Alcázar, D., Narayanan, D., et al. 2019, , 486, 2827, doi: 10.1093/mnras/stz937

Dehnen, W. 2000, , 536, L39, doi: 10.1086/312724

Diemer, B., & Kravtsov, A. V. 2015, , 799, 108, doi: 10.1088/0004-637X/799/1/108

Dolag, K., Borgani, S., Murante, G., & Springel, V. 2009, , 399, 497, doi: 10.1111/j.1365-2966.2009.15034.x

Dolag, K., Komatsu, E., & Sunyaev, R. 2016, , 463, 1797, doi: 10.1093/mnras/stw2035

Dolgov, A. D., Hansen, S. H., Pastor, S., & Semikoz, D. V. 2001, , 554, 74, doi: 10.1086/321381

Doroshkevich, A. G., Kotok, E. V., Poliudov, A. N., et al. 1980, , 192, 321, doi: 10.1093/mnras/192.2.321

Dubois, Y., Peirani, S., Pichon, C., et al. 2016, , 463, 3948, doi: 10.1093/mnras/stw2265

Dunkley, J., Hlozek, R., Sievers, J., et al. 2011, , 739, 52, doi: 10.1088/0004-637X/739/1/52

Dunkley, J., Calabrese, E., Sievers, J., et al. 2013, , 7, 025, doi: 10.1088/1475-7516/2013/07/025

Efstathiou, G., Davis, M., White, S. D. M., & Frenk, C. S. 1985, , 57, 241, doi: 10.1086/191003

Ensslin, T. A., Biermann, P. L., Kronberg, P. P., & Wu, X.-P. 1997, , 477, 560, doi: 10.1086/303722

Evrard, A. E. 1990, , 363, 349, doi: 10.1086/169350

Feng, Y., Chu, M.-Y., Seljak, U., & McDonald, P. 2016a, , 463, 2273, doi: 10.1093/mnras/stw2123

Feng, Y., Di-Matteo, T., Croft, R. A., et al. 2016b, , 455, 2778, doi: 10.1093/mnras/stv2484

Foreman-Mackey, D., Hogg, D. W., Lang, D., & Goodman, J. 2013, , 125, 306, doi: 10.1086/670067

Foreman-Mackey, D., Farr, W., Sinha, M., et al. 2019, The Journal of Open Source Software, 4, 1864, doi: 10.21105/joss.01864

Fowler, J. W., Acquaviva, V., Ade, P. A. R., et al. 2010, , 722, 1148, doi: 10.1088/0004-637X/722/2/1148

George, E. M., Reichardt, C. L., Aird, K. A., et al. 2015, The Astrophysical Journal, 799, 177. http://stacks.iop.org/0004-637X/799/i=2/a=177

George, E. M., Reichardt, C. L., Aird, K. A., et al. 2015, , 799, 177, doi: 10.1088/0004-637X/799/2/177

George, M. R., Fabian, A. C., Sanders, J. S., Young, A. J., & Russell, H. R. 2009, , 395, 657, doi: 10.1111/j.1365-2966.2009.14547.x

Gingold, R. A., & Monaghan, J. J. 1977, , 181, 375, doi: 10.1093/mnras/181.3.375

Gnedin, N. Y. 1995, , 97, 231, doi: 10.1086/192141

Gnedin, N. Y., & Hui, L. 1998, , 296, 44, doi: 10.1046/j.1365-8711.1998.01249.x

Greengard, L., & Rokhlin, V. 1987, Journal of Computational Physics, 73, 325, doi: 10.1016/0021-9991(87)90140-9

Gupta, N., Saro, A., Mohr, J. J., Dolag, K., & Liu, J. 2017, , 469, 3069, doi: 10.1093/mnras/stx715

Hasselfield, M., Hilton, M., Marriage, T. A., et al. 2013, , 7, 008, doi: 10.1088/1475-7516/2013/07/008

He, Y., Mansfield, P., Rau, M. M., Trac, H., & Battaglia, N. 2021a, , 908, 91, doi: 10.3847/1538-4357/abd0ff

He, Y., Trac, H., & Gnedin, N. Y. 2021b, arXiv e-prints, arXiv:2107.04606. https://arxiv.org/abs/2107.04606

Henson, M. A., Barnes, D. J., Kay, S. T., McCarthy, I. G., & Schaye, J. 2017, Monthly Notices of the Royal Astronomical Society, 465, 3361, doi: 10.1093/mnras/stw2899

Hilton, M., Hasselfield, M., Sifón, C., et al. 2018, , 235, 20, doi: 10.3847/1538-4365/aaa6cb

Hitomi Collaboration, Aharonian, F., Akamatsu, H., et al. 2018, , 70, 9, doi: 10.1093/pasj/psx138

Hockney, R. W., & Eastwood, J. W. 1981, Computer Simulation Using Particles

Hoekstra, H., Herbonnet, R., Muzzin, A., et al. 2015, , 449, 685, doi: 10.1093/mnras/stv275

Hopkins, P. F. 2015, , 450, 53, doi: 10.1093/mnras/stv195

Hoshino, A., Henry, J. P., Sato, K., et al. 2010, , 62, 371, doi: 10.1093/pasj/62.2.371

Hu, W., & Dodelson, S. 2002, , 40, 171, doi: 10.1146/annurev.astro.40.060401.093926

Huang, H.-J., Eifler, T., Mandelbaum, R., & Dodelson, S. 2019, , 488, 1652, doi: 10.1093/mnras/stz1714

Hui, L., & Gnedin, N. Y. 1997, , 292, 27, doi: 10.1093/mnras/292.1.27

Iannuzzi, F., & Dolag, K. 2012, , 427, 1024, doi: 10.1111/j.1365-2966.2012.22017.x

Ishiyama, T., Prada, F., Klypin, A. A., et al. 2021, , doi: 10.1093/mnras/stab1755

Itoh, N., Kohyama, Y., & Nozawa, S. 1998, , 502, 7, doi: 10.1086/305876

Kaiser, N. 1986, , 222, 323, doi: 10.1093/mnras/222.2.323

Kaviraj, S., Laigle, C., Kimm, T., et al. 2017, , 467, 4739, doi: 10.1093/mnras/stx126

Kawaharada, M., Okabe, N., Umetsu, K., et al. 2010, , 714, 423, doi: 10.1088/0004-637X/714/1/423

Kay, S. T., Peel, M. W., Short, C. J., et al. 2012, Monthly Notices of the Royal Astronomical Society, 422, 1999, doi: 10.1111/j.1365-2966.2012.20623.x

Khandai, N., Di Matteo, T., Croft, R., et al. 2015, , 450, 1349, doi: 10.1093/mnras/stv627

Klein, R. I., McKee, C. F., & Colella, P. 1994, , 420, 213, doi: 10.1086/173554

Klypin, A., Yepes, G., Gottlöber, S., Prada, F., & Heß, S. 2016, , 457, 4340, doi: 10.1093/mnras/stw248

Klypin, A. A., Trujillo-Gomez, S., & Primack, J. 2011, , 740, 102, doi: 10.1088/0004-637X/740/2/102

Komatsu, E., & Kitayama, T. 1999, The Astrophysical Journal Letters, 526, L1. http://stacks.iop.org/1538-4357/526/i=1/a=L1

Komatsu, E., & Seljak, U. 2002, , 336, 1256, doi: 10.1046/j.1365-8711.2002.05889.x

Kompaneets, A. S. 1957, Soviet Journal of Experimental and Theoretical Physics, 4, 730

Kravtsov, A. V., Klypin, A. A., & Khokhlov, A. M. 1997, , 111, 73, doi: 10.1086/313015

Kravtsov, A. V., Vikhlinin, A., & Nagai, D. 2006, , 650, 128, doi: 10.1086/506319

Lau, E. T., Kravtsov, A. V., & Nagai, D. 2009, The Astrophysical Journal, 705, 1129. http://stacks.iop.org/0004-637X/705/i=2/a=1129

Lau, E. T., Nagai, D., & Nelson, K. 2013, , 777, 151, doi: 10.1088/0004-637X/777/2/151

Le Brun, A. M. C., McCarthy, I. G., Schaye, J., & Ponman, T. J. 2014, , 441, 1270, doi: 10.1093/mnras/stu608

Limber, D. N. 1953, , 117, 134, doi: 10.1086/145672

Lueker, M., Reichardt, C. L., Schaffer, K. K., et al. 2010, , 719, 1045, doi: 10.1088/0004-637X/719/2/1045

Mandelbaum, R., Seljak, U., Cool, R. J., et al. 2006, , 372, 758, doi: 10.1111/j.1365-2966.2006.10906.x

Marinacci, F., Vogelsberger, M., Pakmor, R., et al. 2018, , 480, 5113, doi: 10.1093/mnras/sty2206

Martel, H., & Shapiro, P. R. 1998, , 297, 467, doi: 10.1046/j.1365-8711.1998.01497.x

McCarthy, I. G., Schaye, J., Bird, S., & Le Brun, A. M. C. 2017a, , 465, 2936, doi: 10.1093/mnras/stw2792

—. 2017b, , 465, 2936, doi: 10.1093/mnras/stw2792

McDonald, P., Miralda-Escudé, J., & Cen, R. 2002, , 580, 42, doi: 10.1086/343031

Medezinski, E., Battaglia, N., Umetsu, K., et al. 2018, , 70, S28, doi: 10.1093/pasj/psx128

Miyatake, H., Battaglia, N., Hilton, M., et al. 2019, , 875, 63, doi: 10.3847/1538-4357/ab0af0

Monaco, P., Theuns, T., & Taffoni, G. 2002, , 331, 587, doi: 10.1046/j.1365-8711.2002.05162.x

Morandi, A., & Limousin, M. 2012, , 421, 3147, doi: 10.1111/j.1365-2966.2012.20537.x

Nagai, D. 2006, The Astrophysical Journal, 650, 538. http://stacks.iop.org/0004-637X/650/i=2/a=538

Nagai, D., Kravtsov, A. V., & Vikhlinin, A. 2007a, , 668, 1, doi: 10.1086/521328

Nagai, D., Vikhlinin, A., & Kravtsov, A. V. 2007b, , 655, 98, doi: 10.1086/509868

Naiman, J. P., Pillepich, A., Springel, V., et al. 2018, , 477, 1206, doi: 10.1093/mnras/sty618

Navarro, J. F., Frenk, C. S., & White, S. D. M. 1996, , 462, 563, doi: 10.1086/177173

Navarro, J. F., Frenk, C. S., & White, S. D. M. 1997, , 490, 493, doi: 10.1086/304888

Navarro, J. F., Hayashi, E., Power, C., et al. 2004, , 349, 1039, doi: 10.1111/j.1365-2966.2004.07586.x

Nelson, D., Pillepich, A., Springel, V., et al. 2018, , 475, 624, doi: 10.1093/mnras/stx3040

Nelson, K., Lau, E. T., & Nagai, D. 2014, The Astrophysical Journal, 792, 25. http://stacks.iop.org/0004-637X/792/i=1/a=25

Nelson, K., Rudd, D. H., Shaw, L., & Nagai, D. 2012, , 751, 121, doi: 10.1088/0004-637X/751/2/121

Olamaie, M., Hobson, M. P., & Grainge, K. J. B. 2012, , 423, 1534, doi: 10.1111/j.1365-2966.2012.20980.x

Park, H., Shapiro, P. R., Komatsu, E., et al. 2013, , 769, 93, doi: 10.1088/0004-637X/769/2/93

Pen, U.-L. 1998, , 115, 19, doi: 10.1086/313074

Penna-Lima, M., Bartlett, J. G., Rozo, E., et al. 2017, , 604, A89, doi: 10.1051/0004-6361/201629971

Pfanzagl, J., & Sheynin, O. 1996, Biometrika, 83, 891, doi: 10.1093/biomet/83.4.891

Phillips, P. R. 1995, , 455, 419, doi: 10.1086/176589

Pillepich, A., Nelson, D., Hernquist, L., et al. 2018a, , 475, 648, doi: 10.1093/mnras/stx3112

Pillepich, A., Springel, V., Nelson, D., et al. 2018b, , 473, 4077, doi: 10.1093/mnras/stx2656

Planck Collaboration, Ade, P. A. R., Aghanim, N., et al. 2014a, , 571, A20, doi: 10.1051/0004-6361/201321521

—. 2014b, , 571, A21, doi: 10.1051/0004-6361/201321522

Planck Collaboration, Aghanim, N., Arnaud, M., et al. 2016a, , 594, A22, doi: 10.1051/0004-6361/201525826

Planck Collaboration, Ade, P. A. R., Aghanim, N., et al. 2016b, , 594, A24, doi: 10.1051/0004-6361/201525833

—. 2016c, , 594, A27, doi: 10.1051/0004-6361/201525823

Price, D. J. 2012, Journal of Computational Physics, 231, 759, doi: 10.1016/j.jcp.2010.12.011

Rasia, E., Tormen, G., & Moscardini, L. 2004, , 351, 237, doi: 10.1111/j.1365-2966.2004.07775.x

Rasia, E., Meneghetti, M., Martino, R., et al. 2012, New Journal of Physics, 14, 055018. http://stacks.iop.org/1367-2630/14/i=5/a=055018

Rasia, E., Meneghetti, M., Martino, R., et al. 2012, New Journal of Physics, 14, 055018, doi: 10.1088/1367-2630/14/5/055018

Reese, E. D. 2004, in Measuring and Modeling the Universe, ed. W. L. Freedman, 138. https://arxiv.org/abs/astro-ph/0306073

Reese, E. D., Mohr, J. J., Carlstrom, J. E., et al. 2000, , 533, 38, doi: 10.1086/308662

Reichardt, C. L., Patil, S., Ade, P. A. R., et al. 2021, , 908, 199, doi: 10.3847/1538-4357/abd407

Reiprich, T. H., Hudson, D. S., Zhang, Y.-Y., et al. 2009, , 501, 899, doi: 10.1051/0004-6361/200810404

Rephaeli, Y. 1995, , 445, 33, doi: 10.1086/175669

Schaye, J., Crain, R. A., Bower, R. G., et al. 2015, , 446, 521, doi: 10.1093/mnras/stu2058

Schmidt, R. W., & Allen, S. W. 2007, , 379, 209, doi: 10.1111/j.1365-2966.2007.11928.x

Scoccimarro, R., & Sheth, R. K. 2002, , 329, 629, doi: 10.1046/j.1365-8711.2002.04999.x

Sehgal, N., Bode, P., Das, S., et al. 2010, , 709, 920, doi: 10.1088/0004-637X/709/2/920

Seljak, U., Burwell, J., & Pen, U.-L. 2001, , 63, 063001, doi: 10.1103/PhysRevD.63.063001

Sereno, M., Covone, G., Izzo, L., et al. 2017, , 472, 1946, doi: 10.1093/mnras/stx2085

Shao, J., Zhang, P., Lin, W., & Jing, Y. 2011, , 730, 127, doi: 10.1088/0004-637X/730/2/127

Shaw, L. D., Nagai, D., Bhattacharya, S., & Lau, E. T. 2010, The Astrophysical Journal, 725, 1452. http://stacks.iop.org/0004-637X/725/i=2/a=1452

Shaw, L. D., Nagai, D., Bhattacharya, S., & Lau, E. T. 2010, , 725, 1452, doi: 10.1088/0004-637X/725/2/1452

Shi, X., & Komatsu, E. 2014, Monthly Notices of the Royal Astronomical Society, 442, 521, doi: 10.1093/mnras/stu858

Shi, X., & Komatsu, E. 2014, , 442, 521, doi: 10.1093/mnras/stu858

Shi, X., Komatsu, E., Nagai, D., & Lau, E. T. 2016, Monthly Notices of the Royal Astronomical Society, 455, 2936, doi: 10.1093/mnras/stv2504

Shi, X., Komatsu, E., Nelson, K., & Nagai, D. 2015, Monthly Notices of the Royal Astronomical Society, 448, 1020, doi: 10.1093/mnras/stv036

Siegel, S. R., Sayers, J., Mahdavi, A., et al. 2018, The Astrophysical Journal, 861, 71, doi: 10.3847/1538-4357/aac5f8

Sievers, J. L., Hlozek, R. A., Nolta, M. R., et al. 2013, , 2013, 060, doi: 10.1088/1475-7516/2013/10/060

Simet, M., Battaglia, N., Mandelbaum, R., & Seljak, U. 2015, in American Astronomical Society Meeting Abstracts, Vol. 225, American Astronomical Society Meeting Abstracts #225, 443.04

Simet, M., Battaglia, N., Mandelbaum, R., & Seljak, U. 2016, Monthly Notices of the Royal Astronomical Society, 466, 3663, doi: 10.1093/mnras/stw3322

Simionescu, A., Allen, S. W., Mantz, A., et al. 2011, Science, 331, 1576, doi: 10.1126/science.1200331

Skillman, S. W., Warren, M. S., Turk, M. J., et al. 2014, arXiv e-prints, arXiv:1407.2600. https://arxiv.org/abs/1407.2600

Smith, G. P., Mazzotta, P., Okabe, N., et al. 2016, , 456, L74, doi: 10.1093/mnrasl/slv175

Springel, V. 2005, , 364, 1105, doi: 10.1111/j.1365-2966.2005.09655.x

—. 2010a, , 48, 391, doi: 10.1146/annurev-astro-081309-130914

—. 2010b, , 401, 791, doi: 10.1111/j.1365-2966.2009.15715.x

Springel, V., Frenk, C. S., & White, S. D. M. 2006, , 440, 1137, doi: 10.1038/nature04805

Springel, V., White, S. D. M., Tormen, G., & Kauffmann, G. 2001, , 328, 726, doi: 10.1046/j.1365-8711.2001.04912.x

Springel, V., White, S. D. M., Jenkins, A., et al. 2005, , 435, 629, doi: 10.1038/nature03597

Springel, V., Pakmor, R., Pillepich, A., et al. 2018, , 475, 676, doi: 10.1093/mnras/stx3304

Sunyaev, R. A., & Zeldovich, I. B. 1980a, , 18, 537, doi: 10.1146/annurev.aa.18.090180.002541

Sunyaev, R. A., & Zeldovich, Y. B. 1970a, Comments on Astrophysics and Space Physics, 2, 66

—. 1970b, , 7, 3, doi: 10.1007/BF00653471

—. 1972, Comments on Astrophysics and Space Physics, 4, 173

—. 1980b, , 190, 413, doi: 10.1093/mnras/190.3.413

Tassev, S., Zaldarriaga, M., & Eisenstein, D. J. 2013, , 2013, 036, doi: 10.1088/1475-7516/2013/06/036

Tinker, J., Kravtsov, A. V., Klypin, A., et al. 2008, , 688, 709, doi: 10.1086/591439

Trac, H., Bode, P., & Ostriker, J. P. 2011, The Astrophysical Journal, 727, 94. http://stacks.iop.org/0004-637X/727/i=2/a=94

Trac, H., Bode, P., & Ostriker, J. P. 2011, , 727, 94, doi: 10.1088/0004-637X/727/2/94

Trac, H., & Pen, U.-L. 2004, , 9, 443, doi: 10.1016/j.newast.2004.02.002

Tremmel, M., Karcher, M., Governato, F., et al. 2017, , 470, 1121, doi: 10.1093/mnras/stx1160

Truelove, J. K., Klein, R. I., McKee, C. F., et al. 1997, , 489, L179, doi: 10.1086/310975

Urban, O., Werner, N., Simionescu, A., Allen, S. W., & B?hringer, H. 2011, Monthly Notices of the Royal Astronomical Society, 414, 2101, doi: 10.1111/j.1365-2966.2011.18526.x

Urban, O., Werner, N., Simionescu, A., Allen, S. W., & Böhringer, H. 2011, , 414, 2101, doi: 10.1111/j.1365-2966.2011.18526.x

Vikhlinin, A., Kravtsov, A., Forman, W., et al. 2006, , 640, 691, doi: 10.1086/500288

Vishniac, E. T. 1987, , 322, 597, doi: 10.1086/165755

Vogelsberger, M., Marinacci, F., Torrey, P., & Puchwein, E. 2020, Nature Reviews Physics, 2, 42, doi: 10.1038/s42254-019-0127-2

Vogelsberger, M., Genel, S., Springel, V., et al. 2014, , 509, 177, doi: 10.1038/nature13316

Voit, G. M. 2005, Reviews of Modern Physics, 77, 207, doi: 10.1103/RevModPhys.77.207

von der Linden, A., Mantz, A., Allen, S. W., et al. 2014, , 443, 1973, doi: 10.1093/mnras/stu1423

Watson, W. A., Iliev, I. T., D'Aloisio, A., et al. 2013, , 433, 1230, doi: 10.1093/mnras/stt791

Woodward, P. R. 1986, in NATO Advanced Study Institute (ASI) Series C, Vol. 188, NATO Advanced Study Institute (ASI) Series C, ed. K.-H. A. Winkler & M. L. Norman, 245

Wright, E. L. 1979, , 232, 348, doi: 10.1086/157294

Zhao, H. 1996, , 278, 488, doi: 10.1093/mnras/278.2.488

Zhu, Q. 2017, arXiv e-prints, arXiv:1712.10116. https://arxiv.org/abs/1712.10116